Filamentation of tokamak plasmas

Please check the document version of this publication:

• A submitted manuscript is the version of the article upon submission and before peer-review. There can be important differences between the submitted version and the official published version of record. People interested in the research are advised to contact the author for the final version of the publication, or visit the DOI to the publisher's website.
• The final author version and the galley proof are versions of the publication after peer review.
• The final published version features the final layout of the paper including the volume, issue and page numbers.

Link to publication

Filamentation of tokamak plasmas

Marc Beurskens

Filamentation of tokamak plasmas

Filamentation of tokamak plasmas

PROEFSCHRIFT

ter verkrijging van de graad van doctor aan de
Technische Universiteit Eindhoven, op gezag
van de Rector Magnificus, prof.dr. M. Rem,
voor een commissie aangewezen door het
College voor Promoties in het openbaar te
verdedigen op woensdag 24 maart 1999 om
16.00 uur

door

MARCUS NICOLAAS ARNOLDUS BEURSKENS

geboren te Roermond

Dit proefschrift is goedgekeurd door de promotoren:

prof.dr. N.J. Lopes Cardozo
en
prof.dr. F.C. Schüller

Copromotor: dr.ing. C.J. Barth

Ik draag dit proefschrift op aan mijn ouders

Contents

Summary

Nuclear fusion is a promising candidate for future energy supply. It is the process in which two light nuclei melt together and an enormous amount of energy is produced. In a thermonuclear reactor the burning temperature is 200 million °C. A tokamak is a device in which a thermonuclear plasma is confined by means of a magnetic field. It is currently the best option for a future nuclear fusion reactor.

In the ideal case the topology of the magnetic field in a tokamak consists of nested toroidal flux surfaces in which the plasma is well confined. However, small perturbations are sufficient to break the symmetry of the flux surfaces, and to disturb the confinement. Perturbations of the magnetic topology might be the reason for the anomalously high heat transport observed in tokamaks, which is 1–2 orders of magnitudes larger than expected. The smallest scale of magnetic structures expected to be of importance for heat transport in a tokamak like RTP (Rijnhuizen Tokamak Project) have a size of 1 mm, i.e. <1 % of the minor radius of RTP.

The most spectacular small scale structures observed in RTP are plasma filaments. These are observed as multiple peaks in electron temperature (T_e) and pressure (p_e) with a typical width of 5–10 mm and an amplitude up to 1.5 keV in a 2 keV ambient plasma. They occur in the central region of plasmas that are heated by Electron Cyclotron Heating (ECH). The central issue in this thesis is the study of these filaments. Questions that are posed concern their statistical significance, their topology, conditions for their occurrence and their dynamics.

The filaments have been observed with a high spatial resolution Thomson scattering diagnostic, which measures T_e and electron density (n_e). In order to study the dynamics of the filaments, a double pulse high resolution Thomson scattering diagnostic has been developed. Much effort is put in accurate calibration and testing of the diagnostic. Furthermore, an extensive error analysis of the T_e and n_e measurements is performed to ensure the statistical significance of the observed small scale structures. The specifications of the diagnostic are the following:

- It measures two almost full profiles of T_e and n_e along a vertical chord with a range of $z=[-125, 165]$ mm. A ruby laser is fired twice and the scattered light is recorded by a double detection system containing 2 Intensified-CCD (ICCD) cameras.
- The spatial resolution of the measurements is 3 mm full width at half maximum over the full z-range. This is 2 % of the RTP minor radius.
- The time separation Δt_{TS} between the two measurements can be tuned in the range $\Delta t_{TS}=[20, 800]$ μs.
- The relative statistical error of a single measurement is 3–5 % of T_e and 2–4 % of n_e. This is for the full T_e-range of $T_e= [50\,\mathrm{eV}, 6\,\mathrm{keV}]$, and a typical n_e of $5\times10^{19}\mathrm{m}^{-3}$.

The measurements performed with this diagnostic have added to the understanding of the nature of filaments. First, it is shown that filaments are not due to a diagnostic artefact. A statistical test shows that their amplitude and power spectrum are well above the noise level. Moreover the fact that filaments show dynamic behaviour proves that they are a plasma physical phenomenon: they are wiped out in a sawtooth crash, they take several milliseconds to develop after switching on ECH, and persist for hundreds of microseconds after ECH is switched off.

It is argued that filaments are independent tube-like structures. The fact that filaments are separate entities is determined in an experiment where different cuts through the plasma center are made. Single peaks are found in all cross-sections. It is shown that the filament amplitude is independent of the amplitude of a large m=1 island present as a sawtooth precursor.

The filament must be closed tubes to sustain the measured high T_e gradients. Their toroidal mode number could not be determined. Most likely they have a n=1 periodicity when they occur in the center of the plasma.

The amplitude of central filaments shows a weak dependence on the edge safety factor q_a. The electron density n_e has a strong effect on the filament amplitude. The filament amplitude scales with $n_e^{-1.5}$. The strong dependence can be understood when assuming neo-classical confinement inside filaments. Indeed, the value of the experimentally found heat diffusivity inside a filament is close to the neo-classical value.

Filaments occur inside the q=1 surface in plasmas with central ECH. However, they have also been observed in off-axis heated discharges in the off-axis maximum of the T_e profile. These plasmas did not have a q=1 surface, but the filaments did occur in the low shear area of the plasma, i.e. at the off-axis minimum of the q profile. It is inferred that very low or vanishing magnetic shear is a required condition for the occurrence of filamentation.

The majority of observations of filamentation have been done in plasmas with ECH, but filaments were also observed during the so-called non-local heating effect, when no additional heating was applied. These observations show that filaments are not ECH specific.

Next to the study of filamentation, the double pulse Thomson scattering diagnostic has been used in many other experiments. The results of these are not included in this thesis, but are published elsewhere. The topics of research were: electron heat transport barriers; off-axis sawtooth activity; profiles during pellet ablation; profiles during major and minor disruptions; and the measurement of current density profiles with tangential Thomson scattering.

Samenvatting

Kernfusie is een veelbelovende kandidaat voor levering van energie in de toekomst. Het is een proces waarin twee lichte atoomkernen samensmelten en waarbij een enorme hoeveelheid energie vrijkomt. Een thermonucleaire reactor wordt bedreven bij een temperatuur van 200 miljoen °C. Een tokamak is een apparaat waarin een thermonucleair plasma opgesloten wordt door middel van een magnetisch veld. Momenteel is het de beste optie voor een toekomstige kernfusiereactor.

In het ideale geval bestaat de topologie van het magnetische veld in een tokamak uit geneste toroïdale flux-oppervlakken, waarin het plasma goed wordt opgesloten. Kleine verstoringen kunnen echter de symmetrie van de flux-oppervlakken breken en de opsluiting verslechteren. Verstoringen van de magnetische topologie zouden verantwoordelijk kunnen zijn voor het anomale warmtetransport dat wordt waargenomen in tokamaks (1–2 orden van grootte belangrijker dan verwacht). De kleinste structuren waarvan wordt verwacht dat ze invloed hebben op het warmtetransport in een tokamak als RTP (Rijnhuizen Tokamak Project) hebben afmetingen in de orde van 1 mm, d.w.z. < 1 % van de kleine straal van RTP.

De meest in het oog springende kleine structuren die in RTP-plasma's geobserveerd zijn, zijn de filamenten. Deze worden waargenomen als meervoudige pieken in de temperatuur (T_e) en druk (p_e) van de elektronen met een typische afmeting van 5–10 mm en een amplitude van maximaal 1.5 keV in een omringend plasma met een temperatuur van 2 keV. Ze komen voor in het centrale deel van het plasma onder Elektronen Cyclotron verhitting (ECH). Dit proefschrift gaat over de bestudering van deze filamenten. De statistische significantie, de topologie, condities voor hun bestaan en het dynamische gedrag van de filamenten worden behandeld.

De filamenten werden bestudeerd door meting met hoge resolutie van T_e en dichtheid (n_e) van de elektronen. Deze meting was gebaseerd op Thomsonverstrooiing. Om het dynamische gedrag van de filamenten te kunnen bestuderen, is een dubbel puls Thomsonverstrooiingssysteem ontwikkeld. Het systeem is uitvoerig getest, en nauwkeurig gekalibreerd. Bovendien is een uitgebreide analyse uitgevoerd van de foutbronnen in het systeem, zodat de statistische significantie van de filamenten gegarandeerd kan worden. De specificaties van de diagnostiek zijn als volgt:

- Het systeem meet twee bijna gehele profielen van T_e en n_e langs een verticaal koord met een bereik van $z = [-125, 165]$ mm. Een robijnlaser wordt tweemaal gevuurd en het verstrooide licht wordt gedetecteerd door een dubbel detectiesysteem, bestaande uit twee 'Intensified-CCD' (ICCD) camera's.
- De ruimtelijke resolutie van de metingen is 3 mm breedte op halve hoogte in de z-richting. Dit is 2 % van de kleine straal van RTP.

13

- De tijdseparatie Δt_{TS} van de twee laserpulsen kan worden ingesteld tussen de 20 en 800 μs.
- De statistische relatieve fout in een enkele meting is 3–5 % in T_e en 2–4 % in n_e. Dit geldt voor het gehele bereik in T_e van [50 eV, 6 keV], bij een typische dichtheid $n_e = 5 \times 10^{19}\text{m}^{-3}$.

De metingen die zijn uitgevoerd met deze diagnostiek hebben bijgedragen aan het inzicht in de aard van de filamenten. Ten eerste is aangetoond dat de filamenten geen artefact van het instrument zijn. Een statistische analyse toont aan dat hun amplituden en vermogensspectrum uitsteken boven de ruis. Het dynamische gedrag van de filamenten toont aan dat ze een plasmafysisch fenomeen zijn: tijdens de neergaande flank van de zaagtand oscillatie worden de filamenten vernietigd; het duurt enkele milliseconden na inschakeling van ECH voordat ze zich ontwikkelen; en ze blijven honderden microseconden zichtbaar na afschakeling van ECH.

Het wordt beargumenteerd dat filamenten buis-achtige structuren zijn. Dat de filamenten onafhankelijke structuren zijn is geverifieerd in een experiment waarin verschillende doorsneden van het plasma zijn gemaakt. Smalle pieken werden gevonden in alle doorsneden. In een ander experiment is aangetoond dat de amplitude van de filamenten onafhankelijk is van de amplitude van de zaagtand precursor.

De filamenten moeten gesloten buizen zijn om de gemeten hoge T_e gradiënt in stand te houden. De periodiciteit van de filamenten kon niet bepaald worden. Hoogst waarschijnlijk hebben filamenten die in het centrum binnen q=1 gevonden worden een m=n=1 periodiciteit.

De amplitude van de centrale filamenten vertoont een kleine afhankelijkheid van de totale stroom (q_a) in het plasma. De elektronendichtheid n_e heeft een sterk effect op de amplitude van de filamenten, die schaalt als $n_e^{-1.5}$. Deze sterke afhankelijkheid kan worden begrepen indien binnen de filamenten neo-klassieke waarden voor de opsluiting worden verondersteld. De experimenteel bepaalde waarde van de warmtediffusiviteit in de filamenten is inderdaad dicht bij de neo-klassieke voorspelling.

Filamenten komen voor binnen het $q=1$ oppervlak in centraal verhitte plasma's onder centrale ECH. Ze zijn echter ook geobserveerd in ontlading waarbij het ECH-vermogen halverwege de rand en de as van het plasma is gedeponeerd. In deze plasma's bestaat geen $q=1$ oppervlak, maar de filamenten werden geobserveerd in de nabijheid van de vermogens depositie, in het gebied in het plasma met geringe magnetische afschuiving. We leiden hieruit af dat lage magnetische afschuiving een noodzakelijke conditie is voor filamentatie.

De meeste observaties aan gefilamenteerde plasma's werden gedaan gedurende ECH, maar filamentatie is ook geobserveerd tijdens het zogenaamde niet lokale verhittingseffect, waarbij geen additioneel vermogen werd toegevoegd. Deze observaties tonen aan dat filamentatie geen ECH-specifiek proces is.

Het dubbel puls systeem voor Thomsonverstrooiing is ook ingezet bij vele andere experimentele programma's. De resultaten van deze programma's worden niet in dit proefschrift beschreven, maar zijn elders gepubliceerd. De onderwerpen waren onder meer transportbarrières in het elektronenverlieskanaal, niet-centrale zaagtandactiviteit, profielvormen gedurende pelletablatie, profielvormen tijdens grote en kleine plasmadisrupties en de metingen van het stroomdichtheidsprofiel met tangentiële Thomsonverstrooiing.

Chapter 1

Introduction

1.1 Nuclear fusion research

In this era with a threatening shortage of energy supplies, it is important to look for long term alternative sources. Nuclear fusion is one of these. Fusion is the process in which two light nuclei melt together. In the fusion process an enormous amount of energy is released. It is the process that provides the stars, like our sun, with energy.

The reaction with the highest cross section is the fusion of two hydrogen isotopes, deuterium (D) and tritium (T):

$$D + T \longrightarrow {}_2^4He + n^0 + 17.6\,\text{MeV},\qquad(1.1)$$

in which ${}_2^4He$ is the element helium and n^0 an energetic neutron. D is abundantly present in sea water, and T can be gained from ${}^6Li$, which can be mined and is also present in sea water. In a thermonuclear reactor the burn temperature is 20 keV, which is equivalent to approximately 200 million °C. The pressure of the fuel in the reactor is about 10 atm.

Forty years of fusion research have led to the following achievements:

- Maximum produced fusion power of 16.1 MW,

- Maximum produced fusion energy of 21 MJ, produced in quasi-steady state in 3 seconds,

- Best ratio between fusion and input power: $P_{\text{fus}}/P_{\text{in}} \approx 0.65$,

These have been obtained in a test-reactor of the type 'tokamak' [1]. In such a device the hot fuel, which is fully ionised and thus in the plasma state, is confined by means of a magnetic field as sketched in Fig. 1.1. The magnetic field consists of a toroidal field B_ϕ induced by coils, and a poloidal field B_θ induced by a plasma current. The plasma current in its turn is generated by using the plasma as the secondary winding of a transformer. Thus a helical magnetic field is generated. The helicity of the field is quantified by the magnetic winding number $q = rB_\phi/R_0B_\theta$ (for r and R_0 see Fig. 1.1), which indicates the number of toroidal turns a field line makes before a poloidal turn is completed. Under normal operation q varies from about 1 on the magnetic axis to 3–6 at the periphery of the plasma.

No net energy production has been achieved yet by means of nuclear fusion. Existing tokamaks are too small to achieve ignition of the fusion fuel. To obtain a burning fusion
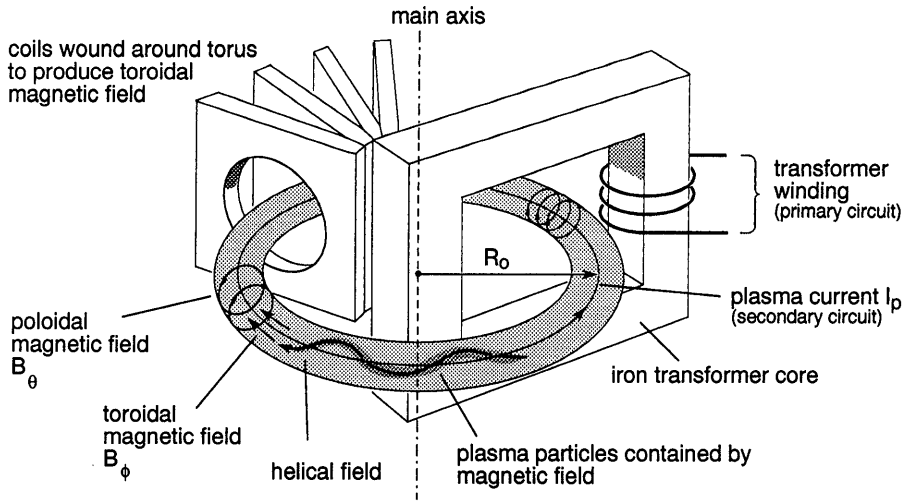
Figure 1.1: *The tokamak, its magnetic fields and some of its subsystems. The major radius is indicated by R, and the minor radius by r.*

plasma the linear dimensions of JET, currently the largest tokamak, need to be increased by a factor of two. Such a machine would still be smaller than a conventional electricity plant running on fossil fuel. It is expected that such a fusion reactor will produce $\sim 1\,\mathrm{GW}$ electric power. However, many technical issues that are associated with the development of such a device need further research. These issues include: the development of huge superconducting coils; the research on materials for the vessel wall and divertor plates that do not suffer fast deterioration due to high thermal energy loads and nuclear reactions with neutrons from the fusion reaction; and the exhaust of thermalised ^4_2He from the plasma.

It is an issue which requires fundamental research is the anomalous transport of heat in the plasma. The transport of heat along magnetic field lines is very large, and 'end' losses are prevented by the toroidal shape of the field configuration. Perpendicular transport should be very slow, assuming that radial heat transport is due to Coulomb collisions only. However, in tokamaks it is found that heat transport, mainly via the electrons, is 10 to 100 times larger than predicted by this so-called 'neo-classical' theory. Imperfections of the magnetic field configuration, which confines the electrons, could play an important role in this anomalous heat transport.

It is generally assumed that the magnetic field in a tokamak forms a nest of perfect toroidal flux surfaces, as is indicated in Fig. 1.2(a). Due to the good transport along the field lines, plasma parameters like temperature and density are constant on a flux surface under this assumption and show poloidal symmetry. The temperature and density are a smooth function of the minor radius as shown in Fig. 1.3(a). However, a small perturbation of the order of 10^{-5} to 10^{-4} of the toroidal magnetic field B_ϕ is sufficient to break the symmetry, and to influence the transport properties of the plasma. Especially surfaces with simple rational values of the winding number q are sensitive to these perturbations. In this perturbed case, the topology changes in a mixture of 'good' surfaces, magnetic
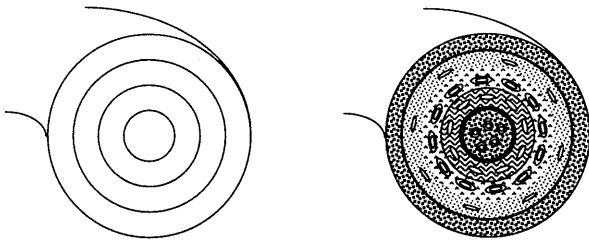
Figure 1.2: *The standard theory of a tokamak plasma assumes a simple magnetic topology: perfect flux surfaces which form a nested set. Under perturbation, the flux surfaces at which q is rational degenerate to form magnetic islands embedded in a region of stochastic field.*
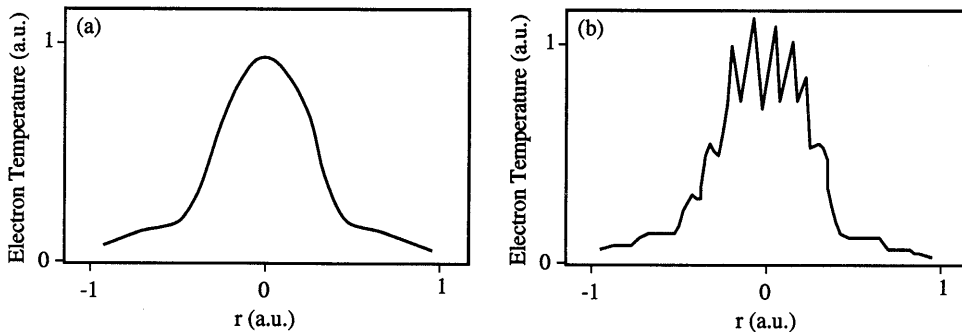
Figure 1.3: *Example of a (a) smooth temperature profile and (b) a profile showing a lot of small scale structure.*

islands, and layers of stochastic field, see Fig 1.2(b). Regions of good confinement alternate with regions of worse confinement. In this case the profile of the temperature is not a smooth function of r anymore, as indicated in Fig 1.3(b).

Although magnetic perturbations may be arbitrarily small, the smallest scale of importance for electron heat transport is expected to be of the size of the ion Larmor radius. In a tokamak like RTP (Rijnhuizen tokamak project), this radius is $\sim 1\,\mathrm{mm}$. This is the smallest scale of structures to be expected in the temperature and density profiles. For RTP with a minor radius of $165\,\mathrm{mm}$, the spatial resolution required to resolve these structures should be better than $1\,\%$ of the minor radius.

1.2 Experimental evidence for small scale magnetic structures

Fluctuation levels of the magnetic field of 10^{-5} to 10^{-4} have indeed been observed in a tokamak [2]. Furthermore, evidence for the footprint of magnetic structures, like magnetic islands, in electron temperature (T_e) and density (n_e) profiles have been reported [4, 5, 6, 7]. Measurements of T_e and n_e with high spatial resolution are very difficult to perform in a tokamak. Mostly, the spatial resolution is 5–10 % of the minor radius, and the minimum
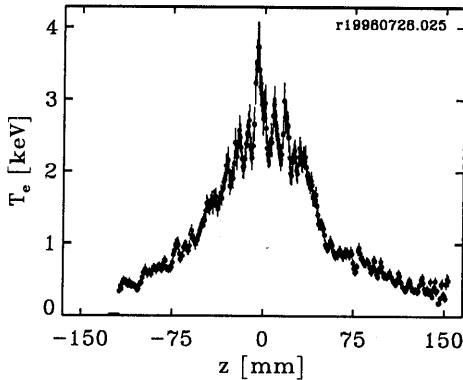
Figure 1.4: *Example of filaments in the T_e profile of an ECH plasma. They occur inside the steep gradients. Outside these gradients quasi-periodic structures are present.*
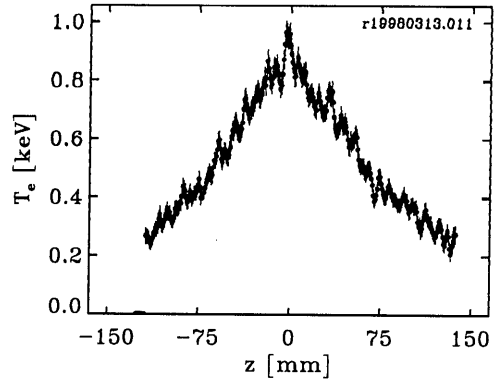
Figure 1.5: *Example of a T_e profile of an Ohmic discharge showing the quasi-periodic structures. Their amplitude is typically 50–100 eV.*

size of observed structures therefore is limited to 10–20 % of the minor radius.

An exception is the high spatial resolution Thomson scattering diagnostic at RTP [3], which measures T_e and n_e with a spatial resolution of 2 % of the minor radius. Furthermore, next to the Ohmic heating by the plasma current, at RTP strong additional heating is available in RTP by means of Electron Cyclotron Heating (ECH), which enhances the amplitude of structures in T_e. Appart from large magnetic islands with a size of 10–20 % of the minor radius, also small scale structures have been observed with this Thomson scattering diagnostic. The most striking observations in RTP are the plasma filaments. These are observed as multiple peaks in T_e with a width of 5-10 mm, i.e 3–6 % of the minor radius. Their amplitude can be up to 1–1.5 keV in a 2 keV ambient plasma. An example is given in Fig. 1.4. The peaks do not show up in n_e. The filaments were first reported in [8]. These were measurements with a single pulse high resolution Thomson scattering diagnostic. Thus only one measurement per discharge could be performed. It was reported that filaments occur in the central region inside the steep gradients near the $q = 1$ surface of plasmas with ECH. Furthermore, outside these steep gradients quasi-periodic structures were observed with similar dimensions as the filaments, but much lower amplitudes; 50–100 eV. These quasi-periodic structures are also observed throughout the full profile in plasmas without ECH, e.g. Fig. 1.5.

1.3   This thesis

This thesis contains a further study of filamentation, and the diagnostic development required to perform this study. Open questions concerning filaments are:

- The topology of the filaments: Are the observed peaks a cross section of toroidally extended structures or are they local T_e fluctuations? If they are spatial structures, are they closed flux loops? Or could the very localised heating of a population of electrons connected to a bundle of field lines give rise to the observations?

- Their relation with MHD activity: What is their relation with the central sawtooth crash and the sawtooth precursor? Are the filaments part of a single large magnetic island or are they separate structures?
- Their occurrence: Are filaments ECH induced or do they pre-exist in Ohmic discharges? Are the peaks also observed in discharges without ECH? Is their occurrence restricted to the central q=1 region in the plasma?
- Their lifetime: Are correlation studies feasible for giving an indication of the lifetime of the filaments?
- The time scale of filament creation: What is the connection with other typical time scales such as the energy confinement time and current diffusion?

To answer some of these questions, measurements of the dynamics of the filaments are required. The temporal resolution that is required is determined by the toroidal plasma rotation time and the time scale of MHD phenomena like the sawtooth crash. The plasma rotation in RTP has a typical period of $100\,\mu s$, and a sawtooth cycle takes 0.5–1.5 ms.

No diagnostic method other than Thomson scattering yields the required spatial resolution of 2 % of the minor radius. However, to design a multi pulse high resolution Thomson scattering diagnostic to obtain time information on the small scale structures is no sinecure. The problem lies in the trade off between laser power and high repetition rates. High laser power is required to obtain high enough signal to noise ratio to resolve the small structures.

At RTP a double pulse Thomson scattering diagnostic has been constructed. A high power ruby laser was available that could yield two laser pulses with a tunable time separation of $20–800\,\mu s$, which is in the range of the typical time scales in the plasma. However the detection system of the old single pulse diagnostic contained only one CCD camera. The readout time of this camera is in the range a few seconds, and this is not fast enough to separate the two laser pulses. Therefore a new detection branch has been developed containing two CCD cameras and two additional image intensifiers that act as fast electronic shutters to separate the two laser pulses.

This way a double pulse Thomson scattering diagnostic is obtained. With this diagnostic dynamic studies like the study of the effect of sawteeth on filaments, and of profile reproduction after a single toroidal turn of the plasma are feasible.

This thesis describes the new double pulse high resolution Thomson scattering diagnostic and its instrumental properties. A large effort is put in testing the system on consistency between the measurements of two CCD cameras. Furthermore, an extensive study of the error of the measurements is performed to ensure the significance of the measured structures. Next to the instrumental part of this thesis an extensive study of the plasma filaments using the double pulse diagnostic is performed that answers many of the questions on filaments posed above. The layout of the thesis is as follows:

- Chapter 2 deals with the theory of Thomson scattering. An expression is given for the relativistic Thomson scattering spectrum, which will be used to fit the experimental spectra.
- Chapter 3 describes the Rijnhuizen Tokamak Project (RTP), its heating system and diagnostic tools.
- Chapter 4 gives an extensive description and test of the RTP double pulse Thomson scattering diagnostic, and some examples of its application.

- Chapter 5 analyses both the statistical and systematic error on the double pulse Thomson scattering measurements.
- Chapter 6 is the study of plasma filamentation. The above addressed questions are discussed. Theoretical considerations together with experimental observations will give an indication of the nature of filaments
- Chapter 7 gives an evaluation of the work performed, suggestions for future developments on high resolution Thomson scattering and future experiments on filamentation.

1.4   Publications

The work on the double pulse Thomson scattering diagnostic has yielded many results. In this thesis only the work dealing with the diagnostic development and the study on plasma filamentation is described. The rest is published elsewhere. Below a list of publications is given. The publications marked with a ♣ are included as chapters 4, 5 and 6 in this thesis.

1.4.1   Journals

1. ♣ (*chapter* 5) 'Error analysis of RTP Thomson scattering data.'
   M.N.A. Beurskens, C.J. Barth, C.C. Chu, and N.J. Lopes Cardozo. Accepted for publication in Rev. Sci. Instrum.

2. 'Structures in T_e profiles: high resolution Thomson scattering in RTP.'
   M.N.A. Beurskens, C.J. Barth, N.J. Lopes Cardozo, and H.J. van der Meiden. Rev. Sci. Instrum. **70** (1) (1999) 995–997

3. 'Double Pulse Thomson Scattering System at RTP'
   M.N.A. Beurskens, C.J. Barth, C.C. Chu, J. Herranz, H.J. van der Meiden, and F.J. Pijper, Rev. Sci. Instrum. **68** (1),(1997) 721–724.

4. 'A high resolution mulitposition Thomson scattering system for the Rijnhuizen tokamak project'.
   C.J. Barth, M.N.A. Beurskens, C.C. Chu, A.J.H. Donné, N.J. Lopes Cardozo, J. Herranz, H.J. van der Meiden, and F.J. Pijper Rev. sci. Instrum. **68** (9), (1997) 3380-3392.

5. 'Electron thermal transport in RTP: filaments, barriers, and bifurcations'
   N.J. Lopes Cardozo, *et al.*, among them M.N.A. Beurskens, Plasma Phys. Control. Fusion **39**, suppl. 12B, (1997) B303-B316.

6. 'Steady-state hollow electron temperature profiles in the Rijnhuizen tokamak project'.
   G.M.D. Hogeweij, *et al.*, among them M.N.A. Beurskens, Phys Rev. Letters **76** (1996) 632–635.

7. ♣ (*chapter* 4) 'Double pulse multiposition Thomson scattering and dynamics of small scale T_e and n_e structures in RTP'
   M.N.A. Beurskens, C.J. Barth, N.J. Lopes Cardozo, and H.J. van der Meiden. Submitted to Rev. Sci. Instrum.

8. ♣ (*chapter* 6) 'Filamentation in the RTP tokamak'
   M.N.A. Beurskens, E.R. Arends , C.J. Barth, N.J. Lopes Cardozo and H.J. van der Meiden. Submitted to Nucl. Fusion.

9. 'Steady state off-axis sawtoothing near q=3/2, 2 and 3 in a Tokamak'
   R.F.G. Meulenbroeks, M.R. de Baar, M.N.A. Beurskens, H.J. de Blank, B.H. Deng, G.M.D. Hogeweij, N.J. Lopes Cardozo, A. Montvai, Th. Oyevaar and the RTP-team. submitted to Phys rev. lett.

10. 'Tokamak plasmas with dominant Electron cyclotron heating; evidence for electron thermal transport barriers'.
    M.R. de Baar, M.N.A. Beurskens, G.M.D. Hogeweij, and N.J. Lopes Cardozo. Submitted to Nucl. Fusion.

11. 'Calibration procedure and data processing for the multiposition Thomson scattering system at RTP'
    C.C. Chu, C.J. Barth, M.N.A. Beurskens, N.J. Lopes Cardozo, and H.J. van der Meiden. Submitted to Rev. Sci. Instrum.

1.4.2 Conference contributions

1. 'Structures in T_e profiles: high resolution Thomson scattering in RTP.'
   M.N.A. Beurskens, C.J. Barth, N.J. Lopes Cardozo, H.J. van der Meiden and the RTP team, Proc. 25th EPS Conf. on Contr. Fusion and Plasma Phys., Prague (1998) B078PR.

2. 'Current density measurements with tangential Thomson scattering in plasmas with peaked and hollow temperature profiles'
   F.A. Karelse, C.J. Barth, M.N.A. Beurskens, G.M.D. Hogeweij, N.J. Lopes Cardozo, H.J. van der Meiden and the RTP team, Proc. 25th EPS Conf. on Contr. Fusion and Plasma Phys., Prague (1998) B106PR.

3. 'Off-axis sawtooth like instabilities near $q = 3/2$, 2 and 3 in RTP'
   R.F.G. Meulenbroeks, M.R. de Baar, M.N.A. Beurskens, H.J. de Blank, B.H. Deng, G.M.D. Hogeweij, N.J. Lopes Cardozo, A. Montvai, Th. Ooyevaar and the RTP team, Proc. 25th EPS Conf. on Contr. Fusion and Plasma Phys., Prague (1998) B129PR.

4. 'Radial particle transport during pellet injection in RTP'
   J. de Kloe, M.N.A. Beurskens, G.M.D. Hogeweij, J. Lok, N.J. Lopes Cardozo, E. Noordermeer, A.A.M. Oomens and the RTP team Proc. 25th EPS Conf. on Contr. Fusion and Plasma Phys., Prague (1998) B085PR.

5. 'Progress in EC Heating and current drive physics and technology'
   A.A.M. Oomens *et al.*, among them M.N.A. Beurskens, 17th International conference on plasma physics and controlled nuclear fusion research, Yokohama, Japan (1998)

6. 'Electron transport studies in the Rijnhuizen tokamak RTP'
   N.J. Lopes Cardozo *et al.*, among them M.N.A. Beurskens, 17th International conference on plasma physics and controlled nuclear fusion research, Yokohama, Japan (1998)

7. 'Dynamics of small scale T_e, n_e and p_e structures, Thomson scattering at RTP'
   M.N.A. Beurskens, C.J. Barth, N.J. Lopes Cardozo, H.J. van der Meiden and the

RTP team, Proc. 24th EPS Conf. on Contr. Fusion and Plasma Phys., Berchtesgaden (1997), Part II, 597–600.

8. 'Current density profiles measured with multi-position tangential Thomson scattering in the RTP-tokamak'
F.A. Karelse, M. de Bruijne, M.N.A. Beurskens, C.J. Barth, G.M.D. Hogeweij, N.J. Lopes Cardozo, H.J. van der Meiden, F.J. Pijper and the RTP-team, Proc. 24th EPS Conf. on Contr. Fusion and Plasma Phys., Berchtesgaden (1997), Part II, 621–624.

9. 'Evidence for fast radial transport during pellet ablation in the RTP tokamak as measured by Thomson scattering.'
J. de Kloe, M.N.A. Beurskens, G.M.D. Hogeweij, J. Lok, N.J. Lopes Cardozo, A.A.M. Oomens and the RTP team, Proc. 24th EPS Conf. on Contr. Fusion and Plasma Phys., Berchtesgaden (1997), Part II, 593–596.

10. 'Disruption studies with active triggering of Thomson scattering in RTP'
F.J.B. Salzedas, S. Hokin, M.N.A. Beurskens, H.J. van der Meiden, A.A.M. Oomens, Th. Ooyevaar, F.C. Schüller and the RTP team, Proc. 24th EPS Conf. on Contr. Fusion and Plasma Phys., Berchtesgaden (1997), Part II, 589–592.

11. 'Double pulse multiposition Thomson scattering at RTP: performance and results'
M.N.A. Beurskens, C.J. Barth, N.J. Lopes Cardozo, H.J. van der Meiden and the RTP team, Proc. of 8th int. symp. on Laser Aided Plasma Diagnostics, Doorwerth (1997), 217–222.

12. 'First current density measurements with tangential Thomson scattering at RTP'
F.A. Karelse, C.J. Barth, M.N.A. Beurskens, M. de Bruijne, G.M.D. Hogeweij, N.J. Lopes Cardozo, H.J. van der Meiden, F.J. Pijper and the RTP team, Proc. of 8th int.symp. on Laser Aided Plasma Diagnostics, Doorwerth (1997), 253–258.

13. 'Double pulse Thomson scattering at RTP: First results'
M.N.A. Beurskens, C.J. Barth, C.C. Chu, N.J. Lopes Cardozo, H.J. van der Meiden, F.J. Pijper and the RTP team, Proc. 23rd EPS Conf. on Contr. Fusion and Plasma Phys., Kiev, (1996), Part III, 1088-1091.

14. 'Pellet disturbed plasmas in the RTP tokamak'
J. de Kloe, J. Lok, M.N.A. Beurskens, J.F.M. van Gelder, B. de Groot, G.M.D. Hogeweij, A.A.M. Oomens and the RTP team, Proc. 23rd EPS Conf. on Contr. Fusion and Plasma Phys., Kiev (1996), Part I, 368–371.

15. 'Experimental access to the topology of the magnetic field in a tokamak, Measurements of plasma filamentation in RTP'
N.J. Lopes Cardozo, C.J. Barth, M.N.A. Beurskens, C.C. Chu, J. Lok, F. van der Loo, A. Montvai, A.A.M. Oomens, M. Peters, F.J. Pijper, M. de Rover, F.C. Schüller, M. Steenbakkers and the RTP team, Advance series in nonlinear dynamics (1996), Vol. 9, 358–372.

16. 'Recent results on ECCD and MHD activity in RTP.'
A.J.H. Donné, et al., among them M.N.A. Beurskens, Proc. of the 16th IAEA fusion energy conference, Montreal, Canada (1996), Vol. III 365–372.

17. 'Heat transport in the RTP tokamak.'
G.M.D. Hogeweij, et al., among them M.N.A. Beurskens, Proc. of the 16th IAEA fusion energy conference, Montreal, Canada (1996), Vol. I 655–662.

18. 'Non-Maxwellian velocity distributions and spatial structures in electron temperature profiles of Ohmic and EC-heated discharges in RTP'
F.M.A. Box, M.N.A. Beurskens, M.F.M. Steenbakkers, C.J. Barth, C.C. Chu, N.J. Lopes Cardozo, F.J. Pijper, E. Westerhof and the RTP team, Proc. 22nd EPS Conf. on Contr. Fusion and Plasma Phys., Bournemouth (1995) Part II. 129–132.

19. 'High resolution multiposition Thomson scattering at RTP'
C.J. Barth, M.N.A. Beurskens, C.C. Chu, A.H.J. Donné, B.J.J. Grobben, N.J. Lopes Cardozo, H.J. van der Meiden, F.J. Pijper, G.C.H.M. Verhaag and the RTP team, Proc. 7th int. symp. on Laser Aided Plasma Diagnostics, Fukuoka, Japan (1995), 386–391

References

[1] J. Wesson, book: 'Tokamaks', second edition, Clarendon press, Oxford (1997)

[2] L. Colas, *et al.*, Nucl. Fusion, **38** (1998) 903–918.

[3] C.J. Barth, *et al.*, Rev. sci. Instrum. **68** (9), (1997) 3380-3392.

[4] P.C. de Vries, *et al.*, Plasma Phys. and Contr. Fusion, **39**, 1997 439-451.

[5] P.C. de Vries, *et al.*, Nucl. Fusion, **37** (1997) 1641-1646.

[6] M.F.F. Nave, *et al.*, Nucl. Fusion, **32** (1992) 825–835.

[7] T. Yamauchi, *et al.*, Phys. letters A, **223** (1996) 179-185.

[8] N.J. Lopes Cardozo, *et al.*, Phys Rev. Letters **73** (1994) 256-259.

Chapter 2

Thomson scattering Theory

Thomson scattering is one of the available methods to measure the electron temperature (T_e) and density (n_e) in thermonuclear fusion devices. It is based on a measurement of the spectrum of photons that are scattered by the free electrons in the plasma. It is characterised by poor time resolution, but offers excellent accuracy and spatial resolution, can be calibrated absolutely and is completely independent of any other measurement. Since T_e is in the order of $1\,\mathrm{keV}$ and higher, relativistic effects need to be taken into account in the determination of the scattering spectrum.

In this chapter only incoherent Thomson scattering is considered. Correlated scattering of light on the electrons in the plasma can only take place above a certain scale length, the Debye length λ_D. If the wavelength of the applied light source is well below this length than the Thomson scattering process is incoherent. In a thermonuclear plasma $\lambda_D \approx 3 \times 10^{-2}\,\mathrm{mm}$, while the wavelength of the applied light is $694.3\,\mathrm{nm}$.

Mattioli obtained an analytical expression for the relativistic incoherent scattering spectrum assuming a relativistic, isotropic electron velocity distribution [1]. In principle the electron velocity distribution in a tokamak plasma, i.e. a magnetised plasma, need not be isotropic. However, deviations of the scattering spectrum due to the electron cyclotron motion can not be resolved in such plasmas in the case of incoherent Thomson scattering at the ruby laser wavelength ($694.3\,\mathrm{nm}$) [2, 3]. For this reason the velocity distribution is assumed to be isotropic in the plane perpendicular to the magnetic field.

Mattioli did not restrict himself to terms of the first order in $\beta = v/c$ (v is the electron velocity and c the speed of light) in his derivation. He also took the *'finite transit time correction'* into account. In a laboratory plasma the electrons cross the scattering volume and scatter the incident wave in a time shorter than the duration of the laser pulse, but much longer than the wave period. This gives rise to an additional correction compared to the case where the electron remains in the scattering volume during the laser pulse length.

The derivations and final formulas in this chapter are obtained from Mattioli [1]. The scattering geometry and definition of parameters used in this chapter are given in Fig. 2.1. The electric field of a polarised incident (i) electromagnetic wave is given by:

$$\vec{E}_i(\vec{r}, t) = \frac{\vec{E}_{0i}}{2} \exp\left[j(\vec{k}_i \cdot \vec{r} - \omega_i t) \right] , \qquad (2.1)$$
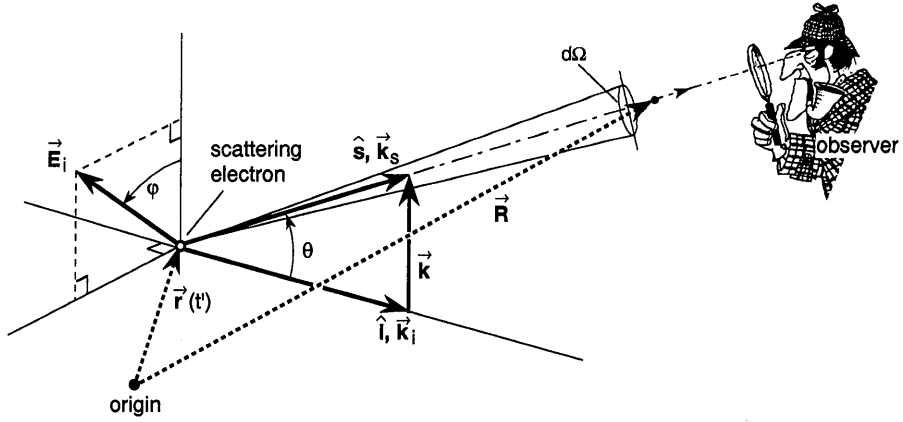
Figure 2.1: *Scattering geometry and definition of parameters.*

where j indicates the imaginary numbers. The acceleration of a single electron under the action of such a wave is:

$$\dot{\vec{\beta}}(\vec{r}, t') = \frac{e}{c\, m_0\, \gamma} \left\{ \vec{E}_i + \vec{\beta} \times (\hat{i} \times \vec{E}_i) - \vec{\beta}(\vec{\beta} \cdot \vec{E}_i) \right\} \tag{2.2}$$

where $\gamma = (1 - \beta^2)^{-\frac{1}{2}}$. The electric field $\vec{E}_s$, at a fixed position $\vec{R}$ and at the time t, scattered by an electron which is accelerated, at the position $\vec{r}$ at the time t', by an electromagnetic wave is given by the formula obtained from the Lienard-Wiechert potentials in the far field region:

$$\vec{E}_s(\vec{R}, t) = \frac{e}{4\pi\, \varepsilon_0\, c\, R} \left[\frac{\hat{s} \times \left\{ (\hat{s} - \vec{\beta}) \times \dot{\vec{\beta}} \right\}}{\left(1 - \hat{s} \cdot \vec{\beta}\right)^3} \right]_{ret} \tag{2.3}$$

The label '*ret*' means that the expression within brackets must be evaluated at the retarded time:

$$t' = t - \frac{|\vec{R} - \vec{r}(t')|}{c} \approx t - \frac{R - \hat{s} \cdot \vec{r}(t')}{c} \tag{2.4}$$

Substituting (2.1) and (2.2) into (2.3), and limiting the incident power to values such that the induced velocity is lower than the thermal velocity, we can derive:

$$\vec{E}_s(\vec{R}, t) = \frac{r_0}{2\gamma R} \left[\frac{\hat{s} \times \left\{ (\hat{s} - \vec{\beta}) \times \left(\vec{E}_{0i} + \vec{\beta} \times (\hat{i} \times \vec{E}_{0i}) - \vec{\beta}(\vec{\beta} \cdot \vec{E}_{0i}) \right) \right\}}{\left(1 - \hat{s} \cdot \vec{\beta}\right)^3} \right]$$

$$\times \exp\left[j\left(\vec{k}_s \cdot \vec{R} - \omega_s^* t - \vec{k} \cdot \vec{r}(0) \right) \right] \tag{2.5}$$

with

$$r_0 = \frac{e^2}{4\pi \varepsilon_0 m_0 c^2}, \tag{2.6}$$

the classical electron radius, and where

$$\omega_s^* = \omega_i \frac{1 - \hat{i} \cdot \vec{\beta}}{1 - \hat{s} \cdot \vec{\beta}} = \omega_i + c\vec{k} \cdot \vec{\beta} \tag{2.7}$$

and

$$\vec{k} = \vec{k}_s - \vec{k}_i = \frac{\omega_s^*}{c} \hat{s} - \frac{\omega_i}{c} \hat{i} \tag{2.8}$$

The power P_s received at a detector placed at R which subtends the solid angle $\Delta\Omega$ during a certain large time interval $-T/2 \leq t \leq T/2$ is:

$$P_s = \lim_{T \to \infty} \frac{1}{T} c \varepsilon_0 R^2 \Delta\Omega \int_{-T/2}^{T/2} \left| \vec{E}_s(t) \right|^2 dt \tag{2.9}$$

Including the *finite transit time correction* and performing a Fourier analysis one arrives at:

$$P_s(\omega_s) = \frac{c \varepsilon_0 r_0^2 \Delta\Omega}{2\gamma^2} \frac{\left[\hat{s} \times \left\{ (\hat{s} - \vec{\beta}) \times \left(\vec{E}_{0i} + \vec{\beta} \times (\hat{i} \times \vec{E}_{0i}) - \vec{\beta}(\vec{\beta} \cdot \vec{E}_{0i}) \right) \right\} \right]^2}{\left[1 - \hat{s} \cdot \vec{\beta} \right]^5} \delta(\omega_s - \omega_s^*) \tag{2.10}$$

We now consider the most common application of a plane polarised wave with the scattering plane perpendicular to the incident electric field $\vec{E}_i$ ($\varphi = 90°$ in Fig. 2.1), and a polariser selecting only the scattered light polarised parallel to $\vec{E}_i$. The scattering cross section $d\sigma_{sv}(\omega_s)/d\Omega$ per unit solid angle and unit frequency for a single electron is defined by:

$$\frac{d\sigma_{sv}}{d\Omega}(\omega_s) = \frac{P_s(\omega_s)}{S_i \Delta\Omega} \tag{2.11}$$

with $S_i = \frac{1}{2} c \varepsilon_0 \vec{E}_i^2$ the incident Poynting vector, and the index v indicating a particular electron with velocity v . $\sigma_{sv}(\omega_s)$ can then be expressed as:

$$\frac{d\sigma_{sv}}{d\Omega}(\omega_s) = \frac{r_0^2}{\gamma^2} \frac{\omega_s^*}{\omega_i} \frac{1}{(1-\beta_s)} \left[1 - \frac{2\beta_E^2(1-\cos\theta)}{(1-\beta_i)(1-\beta_s)}\right] \delta(\omega_s - \omega_s^*) \qquad (2.12)$$

with β_i, β_s and β_E the components of $\vec{\beta}$ in the direction of the unit vectors $\hat{i}, \hat{s}$ and $\hat{E}_i$.

In the case of incoherent Thomson scattering the power scattered by the plasma is obtained by adding the powers scattered by the individual electrons. The scattering cross section $\sigma_s(\omega_s, \theta)$ of the plasma is obtained by averaging $\sigma_{sv}(\omega_s)$ over the electron velocity distribution function. In the case of a relativistic isotropic plasma with electron temperature T_e and density n_e the distribution function will be:

$$f(\beta) = \frac{c^2/v_{th}^2}{2\pi K_2(2 c^2/v_{th}^2)} \gamma^5 \exp\left(-\frac{2c^2}{v_{th}^2} \gamma\right) \qquad (2.13)$$

with K_2 the modified Bessel function of the second kind of order two, and v_{th} the electron thermal velocity:

$$v_{th} = \sqrt{2k_bT_e/m} \qquad (2.14)$$

For the scattering angle θ the scattering cross section per unit solid angle and unit frequency interval is:

$$\frac{d\sigma_s}{d\Omega}(\omega_s, \theta) = \int_{\beta=0}^{1} \frac{d\sigma_{sv}}{d\Omega}(\omega_s) \, f(\beta) \, \beta^2 \, d\beta \qquad (2.15)$$

The power scattered from a volume V now is:

$$P_s(\omega_s, \theta) = n_e \, S_i \, V \, \Delta\Omega \frac{d\sigma_s}{d\Omega}(\omega_s, \theta) \qquad (2.16)$$

By substituting $P_i \Delta L = S_i V$, with ΔL the length of the scattering volume and P_i the incident laser power, (2.16) becomes:

$$P_s(\omega_s, \theta) = n_e \, P_i \, \Delta L \, \Delta\Omega \frac{d\sigma_s}{d\Omega}(\omega_s, \theta) \qquad (2.17)$$

Mattioli [1] has performed the integration 2.15. As a function of the scattering wavelength λ_s and for $T_e \leq 25\,\text{keV}$ $\sigma_s(\lambda, \theta)$ is (under the transformation $\omega_s \rightarrow \lambda_s$) given by:

$$\frac{d\sigma_s}{d\Omega}(\lambda_s, \theta) \; = \; \sigma_0 \; Y(\lambda_i/\lambda_s) \; \exp\left[-\frac{c^2}{v_{th}^2} \; Z(\lambda_i/\lambda_s)\right] \tag{2.18}$$

with:

$$\sigma_0 \; = \; \frac{r_0^2}{2\sqrt{\pi} \; \sin(\theta/2) \; \lambda_i} \; \frac{c}{v_{th}} \; \frac{1}{X(v_{th}/c)} \tag{2.19}$$

σ_0 is the scattering cross section at the incident wavelength λ_i

$$X(v_{th}/c) \approx 1 + \frac{15}{16}\left(\frac{v_{th}}{c}\right)^2 + \frac{105}{512}\left(\frac{v_{th}}{c}\right)^4 \tag{2.20}$$

$$Y(\lambda_i/\lambda_s) = \frac{2\,(\lambda_i/\lambda_s)^4 \; \sin(\theta/2)}{\sqrt{1 \; - \; 2(\lambda_i/\lambda_s)\,\cos(\theta) \; + \; (\lambda_i/\lambda_s)^2}} \tag{2.21}$$

$$Z(\lambda_i/\lambda_s) = \frac{\sqrt{(\lambda_i/\lambda_s) \; - \; 2\cos(\theta) \; + \; (\lambda_i/\lambda_s)^{-1}}}{\sin(\theta/2)} \; - \; 2 \tag{2.22}$$

Examples, according to equation (2.18), of relativistic spectra for incoherent Thomson scattering at the ruby laser wavelength $\lambda_0 = 694.3\,\text{nm}$, are given in Fig. 2.2. The relativistic blue shift increases with T_e.

For the scattering angle θ the total scattered power is

$$P_s(\theta) \; = \; n_e \, P_i \; \Delta L \, \Delta\Omega \int\limits_{\lambda_s} \frac{d\sigma_s}{d\Omega}(\lambda_s, \theta) \; d\lambda_s \tag{2.23}$$

In the classical case this is reduced to:

$$P_s \; = \; n_e \, P_i \; \Delta L \, \Delta\Omega \; r_0^2 \tag{2.24}$$

For a standard experimental Thomson scattering set-up the ratio between incident and scattered power is $P_i/P_s = 10^{14} - 10^{15}$. This gives an indication of the required high laser power and required high sensitivity of the detection system.

Formula (2.18) will be used as a fitting function in a two-parameter least square fit in the form:

$$F(\lambda_s, \theta) = \frac{a_0}{2\sqrt{\pi} \, \sin\left(\theta/2\right) \lambda_i \, a_1 \, X(a_1)} \; Y(\lambda_i/\lambda_s) \; \exp\left[-\frac{Z(\lambda_i/\lambda_s)}{a_1^2} \right] \qquad (2.25)$$

where a_0 and a_1 are the fitting parameters. T_e can be derived directly from $a_1 = v_{th}/c$ and equation (2.14). To determine T_e only a relative calibration of the measured spectrum is required. To retrieve n_e from a_0 an absolute calibration of the measured data by means of, for example, Rayleigh scattering is needed.
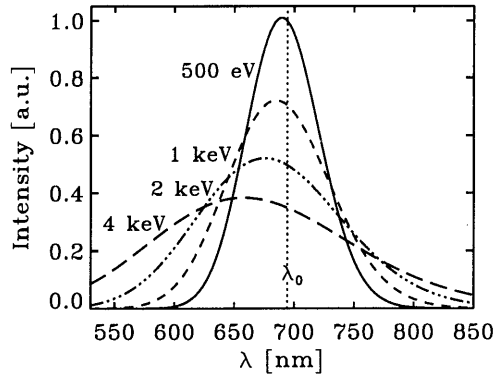
Figure 2.2: *Example of normalised (equal density) relativistic Thomson scattering spectra for Maxwellian velocity distributions with T_e= 500 eV, 1 keV, 2 keV and 4 keV. λ_0 = λ_i = 694.3 nm, i.e. the ruby laser wavelength.*

References

[1] M. Mattioli, 'Incoherent light scattering from high temperature plasmas', EUR-CEA-FC-752 (1974).

[2] J. Sheffield, 'Plasma scattering of electromagnetic radiation', Academic press (1975), ISBN 0-12-638750-8.

[3] I. H. Hutchinson, 'Principles of plasma diagnostics', Cambridge university press (1987), ISBN 0-521-32622-2.

Chapter 3

RTP, ECH and diagnostics

The Rijnhuizen Tokamak Project (RTP) is a tokamak dedicated to the study of electron thermal transport. For this specific task, the tokamak is equipped with high resolution (both spatial and temporal) diagnostics for T_e and n_e [1]. Moreover, RTP features a system for local electron heating at a level significantly exceeding the Ohmic dissipation, using Electron Cyclotron Heating (ECH). Furthermore, RTP is equipped with a pellet injector. In this section, RTP, the 110 GHz ECH system, the pellet injector and the diagnostics relevant for this thesis are described.

3.1   RTP

RTP ($R_0 = 0.72$ m, $a = 0.164$ m) has a circular cross section, a toroidal magnetic field $B_\phi < 2.5$ T and a plasma current $I_p < 150$ kA. Baking, glow discharge cleaning and boronisation are applied to achieve values of the effective ion charge $Z_{eff} < 2$. For all data in this thesis, either hydrogen or helium is used as a filling gas. The discharge duration is typically 0.5 s. Without additional heating, the Ohmic dissipation typically results in a central electron temperature of 700 eV. With application of ECH, this can be increased up to 4 keV. The central density $n_e(0)$ is typically in the range of 1×10^{19}m^{-3} to 1×10^{20}m^{-3}.

3.2   Gyrotron for 110 GHz ECH

The discharges presented in this thesis are either Ohmic or heated with 110 GHz microwaves, injected from the low field side in X-mode, and absorbed at the 2nd harmonic of the electron cyclotron frequency. The microwave source is a GYCOM gyrotron (pulse duration < 200 ms, nominal output power 500 kW, but effective maximum output power 300-500 kW at the time of these experiments). For current drive purposes (ECCD), the system features a tiltable mirror so that co- and counter- (with respect to the plasma current) drive can be applied. Moreover, the mirror can be used to vary the location of deposition in vertical direction.

   The location of deposition can also be tuned in the horizontal direction. The electron cyclotron frequency ω_{ce} is a function of B_ϕ:

$$\omega_{ce} = \frac{e\,B_\phi}{\gamma m_e} \tag{3.1}$$

where e is the electron charge, γ the relativistic factor, and m_e the electron mass. In a tokamak, B_ϕ decreases with radius as $1/R$. Thus, by changing the magnetic field, the resonance position of the gyrotron electron cyclotron waves can be tuned.

The microwave beam has a waist of $\approx 1.5\,\mathrm{cm}$, the radial localisation of the deposition is $\sim 1\,\mathrm{cm} < a/10$. The EC power can exceed the Ohmic heating power up to an order of magnitude.

3.3 Pellet injector

The RTP pellet injector can inject 6 hydrogen pellets sequentially into the plasma. The pellet diameter can be either 0.5 mm or 2 mm. They are injected from the low field side, perpendicular to the magnetic axis (i.e. in a poloidal plane). The angle with horizontal can be chosen between 0 and 7°, resulting in an impact parameter (distance of closest approach to the magnetic axis) of 0 to >10 cm. The latter is referred to as so-called oblique pellet injection.

3.4 Diagnostics

3.4.1 Thomson scattering

The main diagnostic for this thesis is the double pulse high resolution Thomson scattering diagnostic. The diagnostic is extensively described in chapter 5 and 6 and in [2]. It measures T_e and n_e with a very high spatial resolution of 2 % of the minor radius over the full cross section of RTP. The double pulse feature enables the study of some dynamics and reproducibility of small scale structures in T_e and n_e. The time separation between the two pulses can be tuned between 20 and 800 μs. To make small scale structures with low amplitudes visible, a high relative accuracy has been achieved; 3–5 % of T_e and 2–4 % of n_e for T_e in the range of 50 eV–6 keV, at $n_e = 5 \times 10^{19} \mathrm{m}^{-3}$.

3.4.2 Magnetics

RTP features 12 coils for poloidal magnetic field (B_θ) component measurements and 12 saddle coils for radial magnetic field component (B_r) measurements. The horizontal and vertical plasma position are determined by combined measurements of two B_θ-coils and six B_r-coils. The combined signal is used for feed-back control of the plasma-position. I_p is measured with the coils for B_θ. The current through the plasma column and the vessel is measured by a Rogowski-coil.

3.4.3 Interferometry

Two interferometers are mounted on RTP [3, 4]. First, a single chord interferometer at a wavelength of 2 mm is used in combination with a gas-feed system for density feed-

back. It has a time resolution of $10\mu s$. The 2 mm interferometer is also used for absolute calibration of the density profiles as measured with Thomson scattering. Second, a 19 channel interferometer is available for measurement of the temporal evolution of the density profile $n_e(r,t)$. A slab beam at a wavelength of $432\,\mu m$ is injected vertically into the plasma. Phase delays are measured at 19 positions with a time resolution of $2\,\mu s$.

3.4.4 Heterodyne radiometer for ECE-measurements

As was explained in section 3.2 the frequency of electron cyclotron radiation varies with position due to the $1/R$ dependence of $B_\phi(R)$. This leads to the possibility of local measurements of I_{ce}, the intensity of electron cyclotron emission. As I_{ce} is associated with T_e, ECE measurements can be interpreted as measurements of $T_e(r,t)$.

In RTP a 20 channel system for 2nd-harmonic X-mode ECE with a spatial resolution of $\approx 1.5\,\mathrm{cm}$ is installed [5]. The time resolution is $2\,\mu s$. Measurements are obtained from the so-called low field side of the tokamak. The ECE-radiation is collected in a high gain antenna, and fed into a broad-band detector. In two steps, the original frequency band of 86 - 146 GHz is down-converted to 0 - 1.5 GHz, at which it can be processed. In the poloidal section of the antenna, absorbing Macor is mounted on the vessel wall to damp spurious reflections. In this set-up, assuming a Maxwellian velocity distribution, the ECE intensity is given by:

$$I_{ce}(R) \ \sim \omega_{ce}^2(R) \ \cdot \ T_e(R) \ \cdot \ \left(1 - e^{-\tau}\right), \qquad (3.2)$$

where τ is the optical thickness. The optical thickness τ in 2nd-harmonic X-mode is proportional to the electron pressure. In RTP τ is in the range of 1–3.

References

[1] A.J.H. Donné *et al.*, Plasma Physics Reports **20**, (1994) 192

[2] C.J. Barth *et al*, Rev. Sci. Instrum **68**, (1997) 3380

[3] C.A.J. Hugenholtz, Microwave Interferometer and Reflectometer Techniques, Thesis ' Technische Universiteit Eindhoven', (1990)

[4] J.H. Rommers, Faraday rotation measurements in the RTP tokamak, Thesis 'Rijks Universiteit Utrecht', (1996)

[5] J.F.M. van Gelder, Electron Cyclotron Wave Absorption Experiments in Tokamak Plasmas, Thesis 'Rijks Universiteit Utrecht', (1996)

Chapter 4

Double pulse multiposition Thomson scattering

Authors: M.N.A. Beurskens, C.J. Barth, N.J. Lopes Cardozo, H.J. van der Meiden.

Abstract

A high resolution (3 mm FWHM, i.e. 2 % of the minor radius) double pulse multiposition Thomson scattering system is in operation at the Rijnhuizen tokamak project RTP since 1996. It upgrades the previously installed single pulse Thomson scattering system. Two measurements of full electron temperature, T_e, and density, n_e, profiles can be done during one plasma discharge. Typical experimental errors are 3–5 % for T_e and 2–4 % for n_e at $n_e = 5 \times 10^{19}$ m^{-3}. The separation time between the two pulses can be tuned in the range 20–800 μs. Double pulse Thomson scattering measurements have been performed on high n_e Ohmic plasmas with large m/n=2/1 MHD activity, centrally heated plasmas with filaments applying electron cyclotron heating (ECH), plasmas with a transient central T_e-rise after oblique pellet injection showing central filaments, and off-axis heated plasmas with off-axis sawtooth activity. The double pulse feature of the Thomson scattering diagnostic enables the study of dynamics of the T_e and n_e profiles in these plasmas.

4.1   Introduction

The research program of the Rijnhuizen Tokamak Project (RTP; $R/a = 0.72/0.165$ m, $B_T \leq 2.5$ T, $I_p \leq 150$ kA, $q_a \geq 2$) is concentrated on the physics of electron heat transport in tokamak plasmas, one of the areas in tokamak physics which is least understood. To study electron heat transport, RTP is equipped with a high power, < 500 kW, Electron Cyclotron Heating (ECH) system. The deposition of heat can be concentrated within a radial range of 10 % of the minor radius. The ECH can be the dominant heat source, exceeding the Ohmic power by up to a factor of 10. In a typical Ohmic plasma, the central electron temperature (T_e) reaches 0.7 keV, with central ECH T_e up to 4 keV is reached at an electron density (n_e) of 2×10^{19} m^{-3}. The ECH power can be modulated to induce heat waves in the plasma, which are used in heat conduction studies. A comprehensive set of high resolution electron diagnostics [1] is used to measure transport phenomena. These include a 20 channel ECE radiometer, a 19 channel FIR interferometer, an 80 channel 5

camera soft X-ray tomographic system, and the Thomson scattering diagnostic described in the present paper.

Transport studies at RTP can be divided into two categories. In the first, transport is studied on a macroscopic scale, e.g. by performing a power balance analysis or by following the propagation of heat pulses through the plasma [2]. In the second, the effect of small scale structures on T_e, n_e and electron pressure, p_e, on heat transport is analysed. On the basis of measurements of density fluctuations in many tokamaks (see e.g. [3]) as well as theoretical considerations of magnetic islands (e.g. [4]) it may be expected that structures in T_e or n_e with a size down to the ion Larmor radius (ρ_i) could be expected in tokamak plasmas. To see such structures, a spatial resolution of ρ_i (~ 1 mm in RTP) is required.

At RTP a TV TS [1] system is operational which combines excellent spatial resolution with high measurement accuracy [10]. The spatial resolution is 2 % of the minor radius a, i.e. ~ 3 mm, and thus approaches the required resolution of ρ_i. Thanks to the powerful laser, the high system sensitivity and the good resolution of the spectra (88 spectral channels), the measurement accuracy is typically 3–5 % of T_e and 2–4 % of n_e in the range of 50 eV–6 keV for a density of $n_e = 5 \times 10^{19}$ m^{-3} [21]. In 1996 the system has been upgraded from a single pulse to a double pulse system. In each plasma discharge two T_e and n_e profiles can be measured with a separation time Δt, which can be varied from 20–800 μs. Each profile is measured at 350 points along a vertical chord of 300 mm. i.e. 0.86 mm per point. The possible separation times between two profile measurements are in the range of periodic processes in RTP, such as the MHD rotation time (~ 50–200μs) and the sawtooth period ($\sim 500\,\mu$s–2 ms).
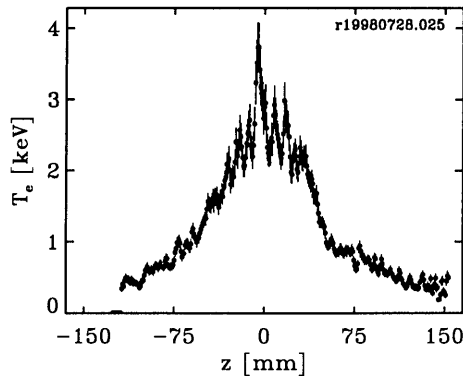
Figure 4.1: *Example of a T_e profile during ECH. Thanks to the high spatial resolution of TS, the filamented character of the plasma can be observed.*

Figure 4.1 shows one example of a multiposition TS measurement at RTP. The figure shows a filamented T_e profile during additional heating by means of ECH. Filaments with an amplitude up to ~ 1 keV and a size down to ~ 5 mm can be observed thanks to the high spatial resolution, [14].

Compared to existing systems only TV TS can achieve the required spatial resolution [8, 9, 10]. Of the other types, LIDAR at JET [5], has been used to look at small MHD

---

[1] *TV stands for applying a 'television' CCD detector*

structures [11], at a resolution of 10 % of a. Systems featuring photodiode detectors and Nd:YAG lasers, like at DIII-D [6], and ASDEX [7], have a higher repetition rate, ($>$20 Hz) than TV TS systems but the spatial resolution is restricted to ≥ 5 % of a. An extensive comparison of TS systems applied in fusion devices is given in [13].

In this paper the double pulse TS diagnostic at RTP and examples of its application are described. In section 4.2 the set-up of the system and the principle of double pulse operation is explained. Furthermore this section discusses the resolution of the measurements and briefly describes the calibration techniques. Section 4.3 describes the analysis method to obtain T_e and n_e from the raw TS data, and briefly discusses the measurement accuracy. The double detection system is tested in section 4.4. Section 4.5 shows a few examples of measurements. These examples serve to illustrate the possibilities of the diagnostic. In depth analysis of these and similar measurements will be presented in forthcoming papers. The paper ends with summary and discussion.

4.2 System set-up and instrumental properties

4.2.1 Overview of the Thomson scattering system at RTP

In this section the RTP TS system is described. An extensive description of the former single pulse diagnostic is given in [10]. The new TS system features a double profile measurement during one discharge. The beam of a ruby laser, ϕ=25 mm diameter, is guided to the input window of the tokamak by means of two mirrors in a periscope set-up. In single pulse mode the laser energy can be up to 25 J in a 15 ns FWHM pulse. The double pulse mode features 2 laser pulses of $<$ 12.5 J each and a pulse width of $\sim$40 ns. An f=3 m telescope guides the beam vertically through the torus and focuses it in the center of the plasma to a waist of $\sim$ 1.5 mm. Because of the small beam divergence in the vacuum system (8.3 mrad) the beam diameter at the plasma edge is $\leq$ 2.5 mm.

Figure 4.2 shows the layout of the double pulse TS system. The observational chord of 300 mm length is imaged onto the entrance slit (height = 200 mm, width = 2 mm) of the polychromator by means of an f = 1000 mm achromatic doublet (item 3). Spectral analysis is performed by a flat grating in the Littrow set-up (item 7). The entrance slit of the polychromator is located just behind the two-part spectral mirror. Collimation of incoming light and focusing of diffracted light is performed by an achromatic doublet (item 6). The grating is oriented such that the laser wavelength returns along its original path through the gap in the spectral mirror. In this way vessel stray light is filtered out, resulting in a stray light ratio of $\leq 5 \times 10^{-4}$ for each spatial element when the full slit height is homogeneously illuminated. The spectrum is projected onto the two-part spherical mirror (item 8) which serves for pupil imaging. The spectral image of 200$\times$ 200 mm^2 is further projected onto the detector surface , i.e. the photo cathode of an image intensifier (item 10), by an f=50 mm/0.95 TV objective using a demagnification of 11.3. Fast electronic gating (100 ns) of the image intensifier suppresses background sources such as H_α line emission and plasma continuum emission. The detected H_α line emission is of the order 8$\times 10^{-2}$ of the total scattered light, and is cut out by means of software. The plasma continuum is $\leq 10^{-2}$ of the scattered light per wavelength channel and is negligibly small.
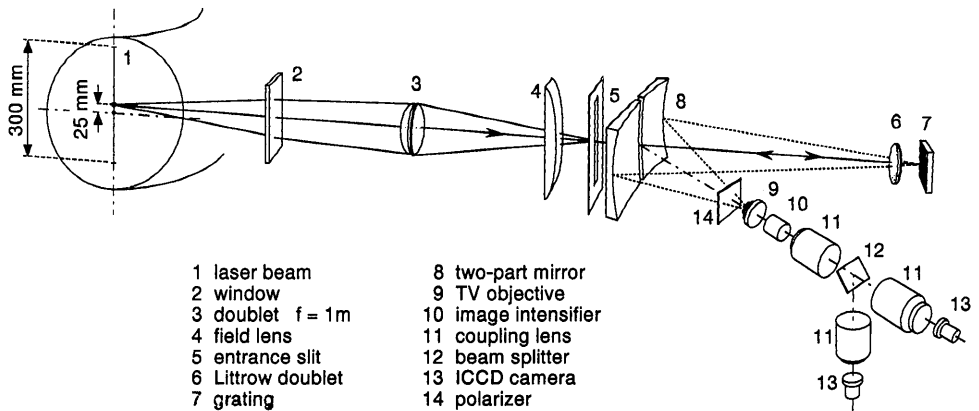
1 laser beam	8 two-part mirror
2 window	9 TV objective
3 doublet f = 1m	10 image intensifier
4 field lens	11 coupling lens
5 entrance slit	12 beam splitter
6 Littrow doublet	13 ICCD camera
7 grating	14 polarizer

Figure 4.2: *Layout of the double pulse TS diagnostic.*

4.2.2   Double detection system

The double detection system has been developed in order to be able to detect two laser pulses 20–800 μs separated in time. The system (see Fig. 4.2) consists of a GEN III image intensifier (item 10), a lens coupling system (items 11), a 50-50 % beamsplitter (item 12) and two 16 bit ICCD cameras. The GEN III image intensifier is equipped with a GaAsP cathode (ϕ 25 mm) giving a net quantum efficiency of 18 % including the MCP (Micro Channel Plate) noise [10]. The MCP-voltage of this intensifier is adjusted such that a photon gain of $\sim$ 2500 is reached at the laser wavelength. Light of its P20 phosphor is coupled (1:1 imaging) to the cathodes of both ICCD cameras by Rodenstock f=95 mm/1.2 objectives with a coupling efficiency of $\sim$ 6 % including the beam splitter. Each camera has a 25 mm image intensifier with an S25 cathode ($\sim$ 3 and 8 % quantum efficiency, for camera 1 and 2 respectively, at the P20 emission wavelength). The ICCD intensifiers are fiber-optically coupled (2.22 : 1) to the CCD chips (385$\times$576 pixels at 22μm pixel size, i.e. $\sim$8.5$\times$12.7 mm^2). Thus the 200$\times$200 mm^2 spectral image at the spherical mirror is reduced to $\sim$ 8 $\times$ 8 mm^2 at the CCD chip, corresponding to 350$\times$350 pixels.

4.2.3   Double pulse operation

The system contains two CCD cameras because the typical read-out time of a high dynamic range (i.e. 16 bit) CCD camera is $\sim$4 s, i.e. much longer than the separation Δt between the two laser pulses. To obtain two laser pulses, the Pockel's cell of the laser is triggered twice during the flash-light period($\sim$ 2-3 ms) with Δt tunable between 20 and 800 μs. Two laser pulses are obtained of < 12.5 J energy and 40 ns FWHM. Figure 4.3 shows the timing scheme of the detector branch for an example in which the pulse separation is 50 μs. The first image intensifier (Fig. 4.2, item 10) is triggered by laser light picked up at the laser and led to the gate circuit by a quartz fiber. The gate of this intensifier is set to 100 ns in order to collect almost the full laser pulse of 40 ns FWHM. This intensifier is gated at both laser pulses, Fig. 4.3 (a). To distinguish between the two laser pulses, the image intensifiers of the ICCD cameras are used as fast electronic shutters; camera 1 records the first laser pulse and camera 2 the second, Fig. 4.3 (c) and (d).

Both cameras are gated open for $20\,\mu s$, i.e. set to the minimum separation time between the two laser pulses. The measurements of the two pulses are now separated. Yet, one problem remains. The P20 phosphor of the first (GEN III) image intensifier has a rather long decay time ($\sim 3\,ms$ to a level of $<1\,\%$), Fig. 4.3 (b). This long emission decay causes an overlap of the first into the second recording, indicated by the filled area inside the $20\,\mu s$ gate of the second camera. In this example of $\Delta t = 50\,\mu s$ the overlap is 14.2 %. Fig. 4.4 gives the overlap as a function of Δt. At $100\,\mu s$ separation the overlap is 7.1 %. The signal of camera 2 can be corrected by subtracting the appropriate part of the first recording from the second. The additional noise generated in this operation is negligible since the system is designed such that the dominant noise source is at the cathode of the first image intensifier (see section 4.3.2). The effect of the overlap on the systematic and statistical error is described in [19].
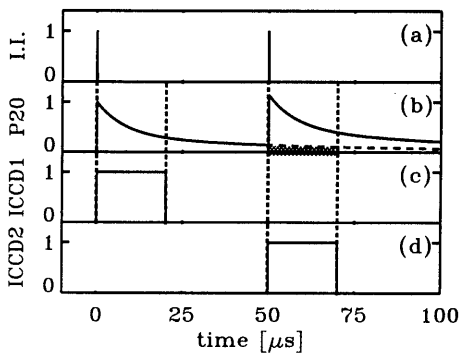

Figure 4.3: *Detector timing scheme for $\Delta t = 50\,\mu s$. (a) The first image intensifier (I.I.) is gated (100 ns) at each laser pulse. (b) The P20 phosphor of the I.I. emits light at both pulses. It has a long decay time due to which an overlap occurs at the second pulse. Camera 1 is gated open for $20\,\mu s$ at the first (c), and camera 2 for $20\,\mu s$ at the second laser pulse (d). The overlap of the first into the second recording is indicated by the grey area in (b).*
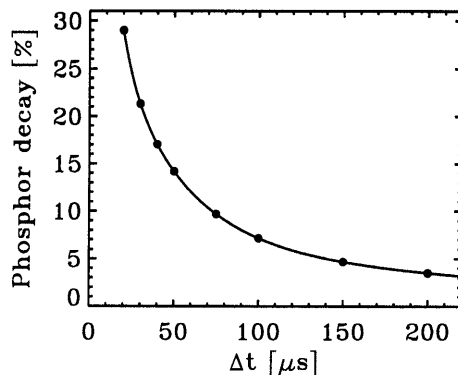

Figure 4.4: *Measured overlap of slow P20 phosphor emission from the first into the second recording as a function of the separation time. It is determined during the $20\,\mu s$ integrating window of the second triggering as indicated in Fig. 4.3(b). At $50\,\mu s$ separation the overlap is 14.2 % and at $100\,\mu s$ it is only 7 %.*

4.2.4 Resolution

The highest resolution possible with the ICCD cameras is 1 pixel, corresponding to 0.8 mm in the plasma and a spectral resolution of 0.9 nm. However, the instrument profiles of the system are wider, as is shown in Fig. 4.5. The figure is obtained from Rayleigh scattering on H_2 gas. It represents the symmetrized instrument function at $z = 0\,mm$ for the laser wavelength, i.e. 694.3 nm, when the full slit height is illuminated. Next to a sharp peak of $\sim 3\,nm$ FWHM, the profile also shows a low broad tail. The broadening of the single wavelength input into a 3 nm wide peak is caused by the resolution of different optical

and electro-optical components of the system, [10]. The halo of the phosphor of the image intensifiers is the cause of the broad tail.
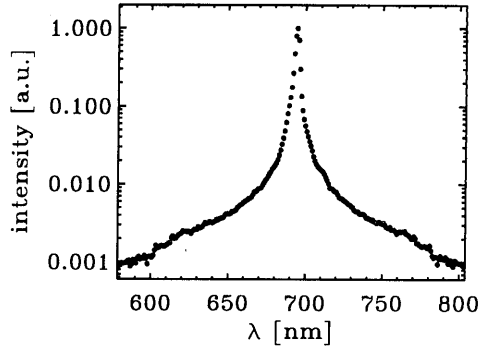

Figure 4.5: *Logarithmic plot of the symmetrised instrument function of camera 1 for the laser wavelength (694.3 nm) at z = 0 mm, obtained from Rayleigh scattering on H_2 gas. It can be divided into a peak with $\sim$ 3 nm FWHM, and a very broad tail at the sub 1 % level.*

The resolution of the total TS system as discussed in this section is defined as the FWHM width of the instrument function. The broad tail is so low that it does not affect the resolution but is important for the final data interpretation, as it gives an off-set to the signal. The effect of the broad tail and the correction for it is discussed in [21].
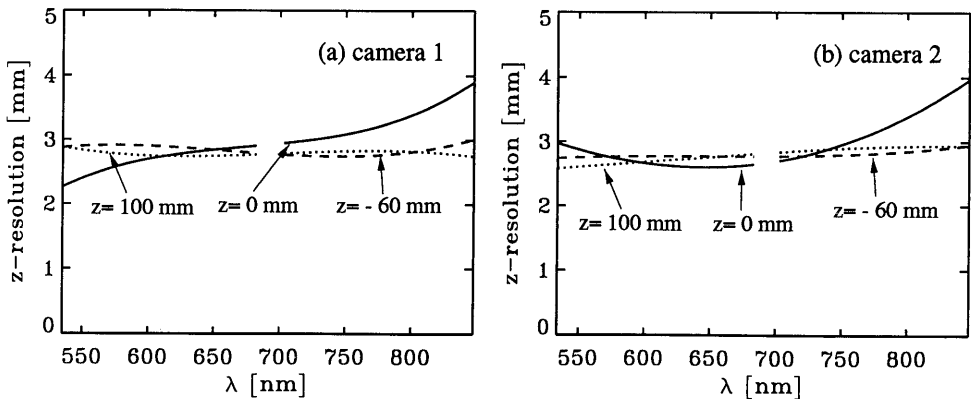
Figure 4.6: *Spatial resolution of the system for (a) camera 1 and (b) camera 2. Note that the resolution is $\sim$ 3 mm for almost the full z-range for both cameras.*

Figure 4.6 shows the spatial resolution for both cameras as a function of wavelength for different positions. The results are obtained from a measurement using a vertical array of pinholes at the laser beam position, also used for position calibration [16]. The figures show that the resolution is below 4 mm FWHM everywhere, and generally below 3 mm FWHM. The optical system is tuned such that a uniform resolution is obtained. In principle it is possible to achieve a FWHM of <2.5 mm in the plasma center and for central wavelengths, at the price of an increase of the FWHM at the egdes of the CCD.

The spectral resolution, Fig. 4.7, has been obtained by homogeneously illuminating the entrance slit, item 5. Fig. 4.2, of the polychromator with light from three spectral lamps, He, Ar and Hg. The width of the polychromator's entrance slit was set to 0.5 mm in this case. The homogeneity of the light distribution is obtained by illuminating the entrance slit of an integrating sphere with a highly reflective inner wall, in front of the viewing doublet (Fig. 4.2, item 3). This measurement is also used for wavelength calibration [16]. The spectral resolution is below 3.2 nm FWHM for all wavelengths and at all positions for both cameras.
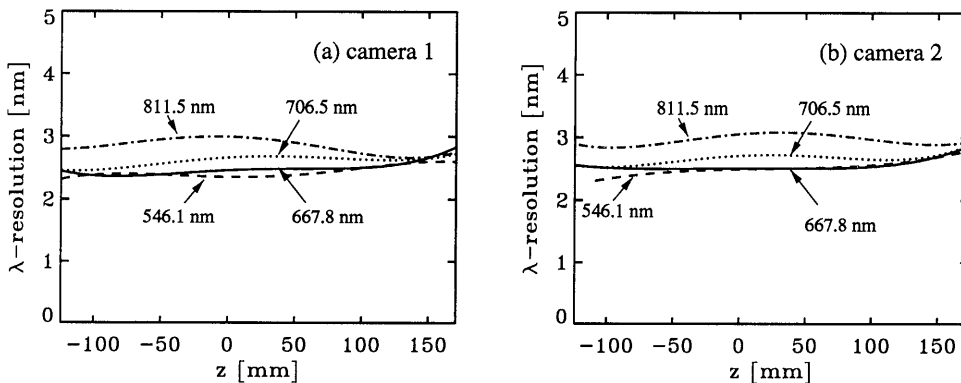

Figure 4.7: *Spectral resolution of the system for (a) camera 1 and (b) camera 2. The spectral resolution ≤ 3.2 nm for the full λ-range.*

The spatial resolution of about 3 mm is < 1% of the plasma diameter, i.e. 330 mm. This is of the order of the smallest scale expected for structures, as was discussed in the introduction. For the presentation and calculation of T_e, n_e and p_e the full pixel resolution of the CCD's will be used. In this way the smallest structure that can be resolved is ≈ 3 pixels wide. The advantage of using the full pixel resolution is that the instrument profile is resolved in the T_e, n_e and p_e profiles. It offers the possibility of a first check on the statistical significance of structures observed in the measured profiles; any structure should involve at least 3 data points.

4.2.5   Calibration

The calibration procedure is described extensively in [16] and will be briefly explained here. Four calibrations are needed in order to calibrate the system; a relative, an absolute, a wavelength and a position calibration. The wavelength and position calibration are performed with the spectral lamps and the vertical array of pinholes, respectively, as discussed in the previous section.

For the relative calibration a tungsten ribbon lamp is used. The emission is calculated using the black body formula and the emissivity of tungsten according to the measurements of De Vos, [17]. In order to get an isotropic light source which illuminates the whole entrance slit of the spectrometer an integrating sphere in front of the viewing doublet (Fig. 4.2, item 3) is applied. This way the relative sensitivity for all pixels can be determined in one measurement. Figure 4.8 shows the spectral sensitivity for one central slice for both cameras. Since the measurement is not fully *in situ*, the measurements had

to be corrected for the wavelength dependent transmission of the sphere, the polarizer and for that of the quartz viewing window [16]. The central cut in the signal around the ruby wavelength (694.3 nm) is caused by the gap in the two-part spectral mirror (Fig. 4.2, item 8). Note that both the short and the long wavelengths around the central wavelength are measured, while most other TS systems only use either the short or the long wavelength side. The relative sensitivity stays high for the whole spectral range, i.e. over 60 % of the maximum. The greater part of the reduction at the edges ($\sim$ 30 %) can be ascribed to the efficiency of the grating which has a maximum at its blazing wavelength of 656 nm. Vignetting by the TV objective (Fig. 4.2, item 5) in front the first image intensifier reduces the sensitivity with another 10 % at the edge.
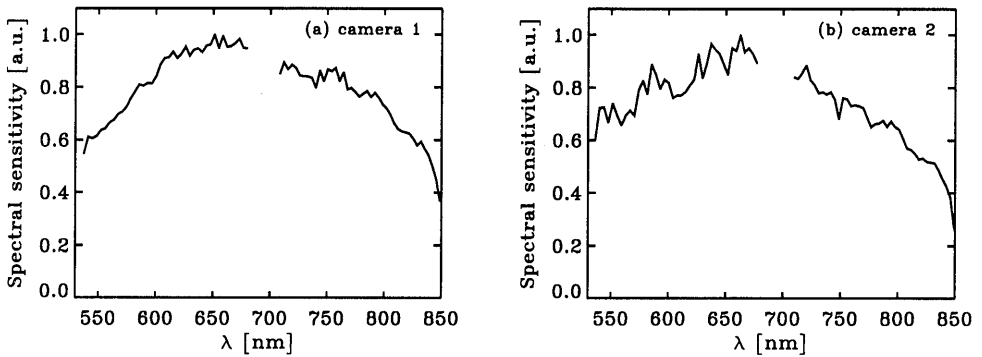
Figure 4.8: *Relative calibration for (a) camera 1 and (b) camera 2 for a central slice. The hole around 694.3 nm is the cutting window for the laser wavelength.*
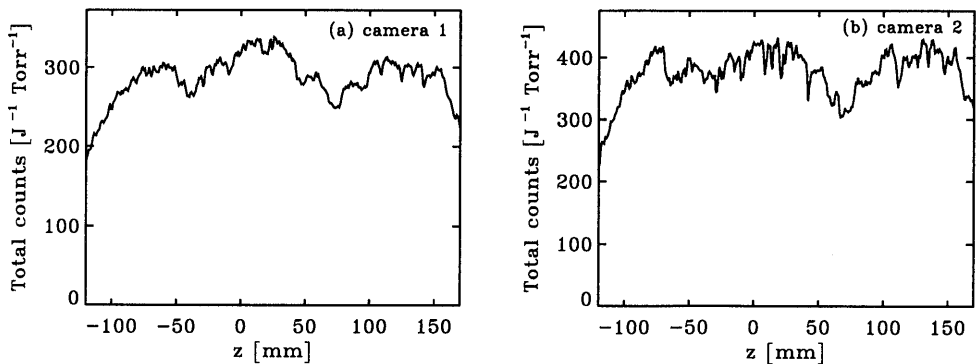
Figure 4.9: *Rayleigh signal as a function of radius for (a) camera 1 and (b) camera 2*

The absolute calibration is needed to get an absolute measure for n_e, and to measure the z-dependent transmission of the system. It is carried out performing Rayleigh scattering on H_2 gas at room temperature. The grating of the spectrometer is rotated such that the ruby wavelength (694.3 nm) is imaged just next to the gap in the spectral mirror (Fig. 4.2,

item 8). A second relative calibration is performed with the rotated grating, to correct for the z-dependence of the relative calibration above. The ratio of the cross sections for Thomson scattering (σ_T) and Rayleigh scattering on H_2 (σ_{R,H_2}) is:

$$\sigma_T/\sigma_{R,H_2} = 1769 \qquad (4.1)$$

This ratio is needed to calculate an absolute calibration curve for n_e [16]. Figure 4.9 shows the Rayleigh scattered light for both cameras integrated along the wavelength direction, expressed in CCD counts. It remains rather flat and stays for the greater part above 75 % of the maximum level. Vignetting losses and divergence of the laser beam lead to a sensitivity loss at the edges. The dips around z=-40 and 60 mm are due to a local decrease in sensitivity of the first image intensifier at these positions.[2]

4.3   Data analysis

4.3.1   Fitting function

Assuming a relativistic Maxwellian velocity distribution Mattioli [18] derived an expression for the spectrum of incoherent TS light. The expression is a Gaussian function of which the blue wing is somewhat enhanced due to relativistic effects. Figure 4.10 gives a few examples of spectra for several temperatures. The figure shows that the relativistic blue-shift becomes larger with higher T_e. The expression of the spectrum has two parameters: a_0 the surface of the Gaussian, and a_1 the width of the Gaussian. The curves are used as a fitting function for the RTP TS measurements. From a_1 T_e can be determined directly. n_e is obtained from a_0, and the absolute calibration discussed in section 4.2.5. In appendix A the analytical expression for the theoretical TS spectrum is given.

4.3.2   Fitting routine and error estimation

The measured Thomson spectra S_{TS} are fitted with F, the expression for the TS spectrum by Mattioli, using a non-linear least square fitting routine by Levenberg and Marquardt [20]. This fitting routine minimizes the χ^2:

$$\chi^2(j) = \sum_{i_b} \left[S_{TS}(i_b, j) - F(i_b) \right]^2 \cdot W(i_b, j) \qquad (4.2)$$

The formula is expressed in CCD-pixels j in the z-direction and i_b in the λ-direction. The index b indicates binning of four pixels in the λ-direction. Experimental data is also binned with four pixels in the wavelength to encount for the instrument profile and to increase the signal to noise ratio per channel. This way 88 wavelength channels remain, which is sufficient to resolve the spectra.

---

[2]*Both the relative and the absolute sensitivity curves of camera 2 show more pixel to pixel variation than camera 1. According to the manufacturer of the ICCD cameras this is due to fiber optical coupling between the image intensifier and the CCD chip. The coupling is glued to the CCD chip with an optical gel that is deteriorating in time such that it becomes less transparent at some places, leading to extra dips in sensitivity. This effect is accounted for by repeating the calibration measurements regularly (every half year).*
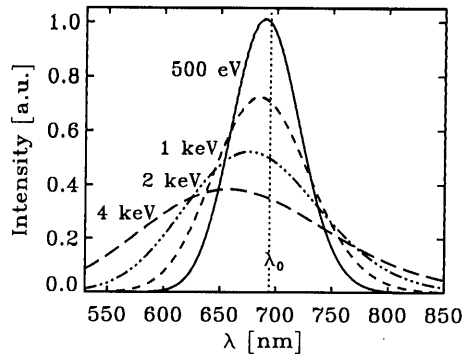
Figure 4.10: *Example of normalised relativistic Thomson scattering spectra for Maxwellian velocity distributions with T_e = 500 eV, 1 keV, 2 keV and 4 keV. Due to relativistic effects the blue shift of the spectra becomes higher for higher values of T_e. $\lambda_0 = 694.3$ nm is the ruby laser wavelength.*

The weight function $W(i_b, j)$ contains an estimator for the error on the measured spectra, σ_{TS}. It smoothes the estimator for σ_{TS} over 5 binned pixels:

$$W(i_b, j) = \frac{5}{\sum\limits_{i_b-2}^{i_b+2} \sigma_{TS}^2(i_b, j)} \quad (4.3)$$

σ_{TS} is dominated by the photon statistics in the system. An extensive study of the contributions of noise in different stages in the diagnostic is described in [21]. The following stages are important for detection noise:

- Photon noise at the first image intensifier (item 10 in Fig. 4.2)

- Photon noise at the intensifier of the ICCD, (item 13)

- Photon noise at the CCD-chip.

- CCD read-out noise, with a standard deviation of $\sigma_{CCD-noise} = 2$ counts.

At zero signal level the CCD read-out noise is dominant. The relative error, $\varepsilon_{TS} = \sigma_{TS}/S_{TS}$, on the measurement is the quadratic sum of the contributions:

$$\varepsilon_{TS}^2(i_b, j) = \frac{\varepsilon_{intensifier\ 1}^2}{\Delta_{intensifier\ 1}}(i_b, j) + \frac{\varepsilon_{intensifier\ 2}^2}{\Delta_{intensifier\ 2}}(i_b, j) + \varepsilon_{CCD}^2(i_b, j) + 4 \cdot \varepsilon_{CCD-noise}^2$$
$$(4.4)$$

representing the contributions listed above. The factors $\Delta_{intensifier\ 1}$ and $\Delta_{intensifier\ 2}$ correct for the smoothing effect of the instrument profile as discussed in [21], and are ≈ 4.4 and 3.6 respectively. The factor 4 in front of $\varepsilon_{CCD-noise}^2$ stems from binning four pixels in the λ-direction. σ_{TS} can be expressed in terms of S_{TS} as:

$$
\begin{aligned}
\sigma_{TS}^2(i_b, j) &= (C_{intensifier\ 1} + C_{intensifier\ 2} + C_{CCD}) \cdot S_{TS}(i_b, j) + 4 \cdot \sigma_{CCD-noise}^2 \\
&= C_{total} \cdot S_{TS}(i_b, j) + 4 \cdot \sigma_{CCD-noise}^2
\end{aligned}
\quad (4.5)
$$

Here $C_{intensifier\ 1}$, $C_{intensifier\ 2}$ and C_{CCD} are the amplitude of the different contributions and determined by system parameters only, [21]. The system is designed such that $> 90\%$ of the noise is determined at the first image intensifier. The values of the amplitudes differ for the two cameras. For camera 1: $C_{intensifier\ 1} = 2.9$, $C_{intensifier\ 2}=0.5$, and $C_{CCD}=0.1$, thus $C_{total}=3.5$. For camera 2: $C_{intensifier\ 1} = 3.8$, $C_{intensifier\ 2}=0.3$, and $C_{CCD}=0.1$, thus $C_{total}=4.2$. Expression (4.5) is used in (4.3) to determine the weight function for the fit.

In [21], simulations of TS spectra are performed using the theoretical TS spectrum by Mattioli, and by adding noise according to the separate contributions. Figure 4.11 gives an example of a fit through such a simulated spectrum with $T_e=1$ keV and $n_e=5\times10^{19}$ m^{-3}. These simulations are performed for a set of T_e values in the range of 50 eV–6keV. From the fits of these simulated spectra, estimations of the statistical error on T_e and n_e are determined. Fig. 4.12 shows the errors on T_e and n_e as a function of T_e. The estimations found by the simulations agree well with the experimental values for errors on T_e and n_e [21]. In the for RTP important range of $0.5 < T_e < 3$ keV ,$\sigma_{T_e}/T_e \leq 4\%$ and $\sigma_{n_e}/n_e= 2.5\%$ at the given density $n_e = 5\times10^{19}$ m^{-3}.
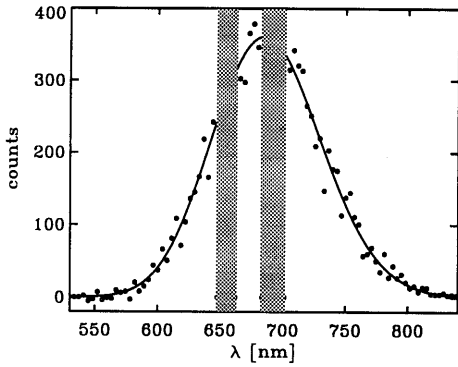

Figure 4.11: *Fit of a simulated spectrum with $T_e = 1keV$ and $n_e=5\times10^{19}\ m^{-3}$. The cutting window and the region around H_α are left out. The noise is added using a noise generator.*
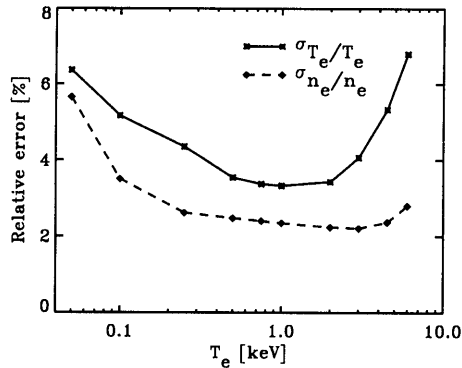
Figure 4.12: *Relative statistical errors on T_e and n_e obtained form simulations as a function of T_e for $n_e=5\times10^{19}\ m^{-3}$. The drawn line represents the error on T_e and the dashed line the error on n_e.*

4.3.3   From raw data to T_e, n_e and p_e

Figure 4.13 shows an example of the CCD images of a double pulse measurement of a high n_e plasma, with $\Delta t = 75\,\mu$s. The raw CCD images contain TS spectra for 350 positions. The spectra show a dip around the laser wavelength, i.e. 694.3 nm. This is caused by the cutting window in the spectral mirror (Fig. 4.2, item 8). At 656.3 nm the H_α Balmer line can be recognized.

Before fitting, the data should undergo corrections and calibrations. A chronological list of corrections and calibrations is given in appendix B. Figure 4.14 gives an example of a fit for both the cameras for a calibrated spectrum in the central region of the plasma. The fit matches the data very well: for camera 1 the reduced $\chi^2_\nu=0.76$ and for camera 2 $\chi^2_\nu=1.16$. The averaged $< \chi^2_\nu >$ over all spatial points is 1.0 for both cameras. From the width a_1, T_e can be determined directly. In order to derive n_e from the surface a_0

of the spectrum fit the absolute calibration performed with Rayleigh scattering (section 4.2.5) and a laser-energy measurement is used. Finally, the electron pressure p_e can be calculated using the ideal gas law. For the determination of the error on p_e the covariance between the errors on T_e and n_e has been taken into account.

Figure 4.15 shows T_e, n_e, and p_e profiles derived from the data in Fig. 4.13. Very conspicuous are the flat areas on the profiles between $|z|=100$ and $70\,\mathrm{mm}$ in the first pulse. They are absent in the second pulse. In section 4.5.1 it will be shown that the flat areas are the O-points of a rotating m/n=2/1 magnetic island.
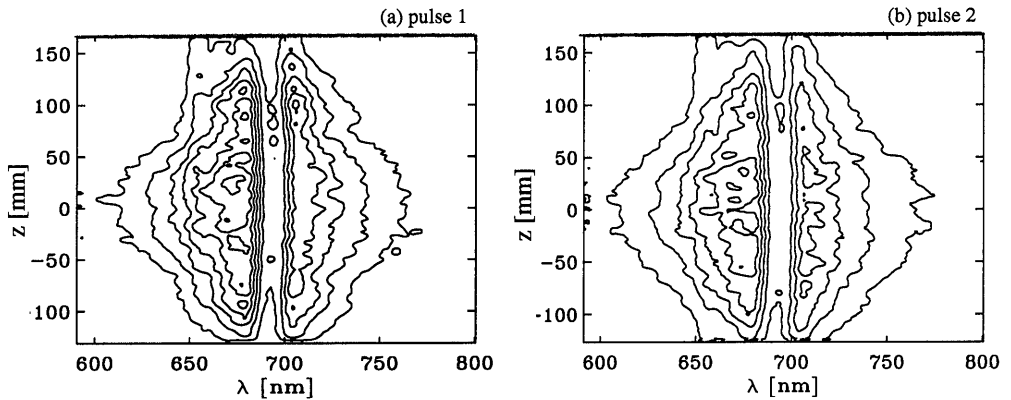
Figure 4.13: *Contour plot of CCD-image containing raw Thomson scattering data for (a) camera 1 and (b) camera 2. The measurements are taken in a high n_e Ohmic discharge. The separation time between the two pulses is $\Delta t = 75\,\mu s$*
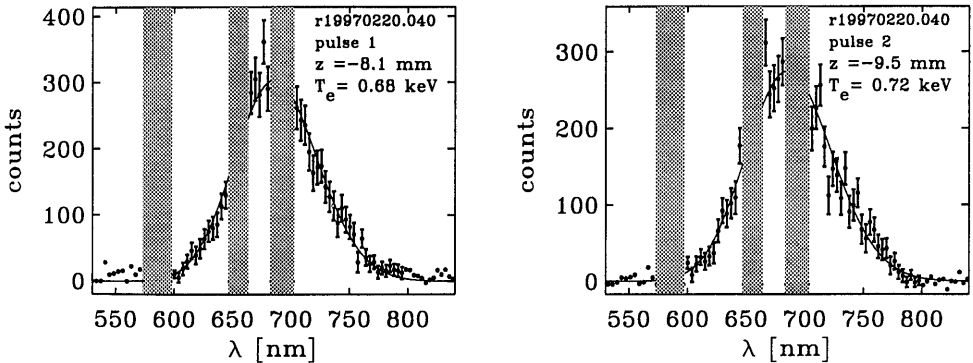
Figure 4.14: *Fitted Thomson spectrum for (a) camera 1 and (b) camera 2. The spectra come from a central slice in Fig. 4.13 (a) and (b).*
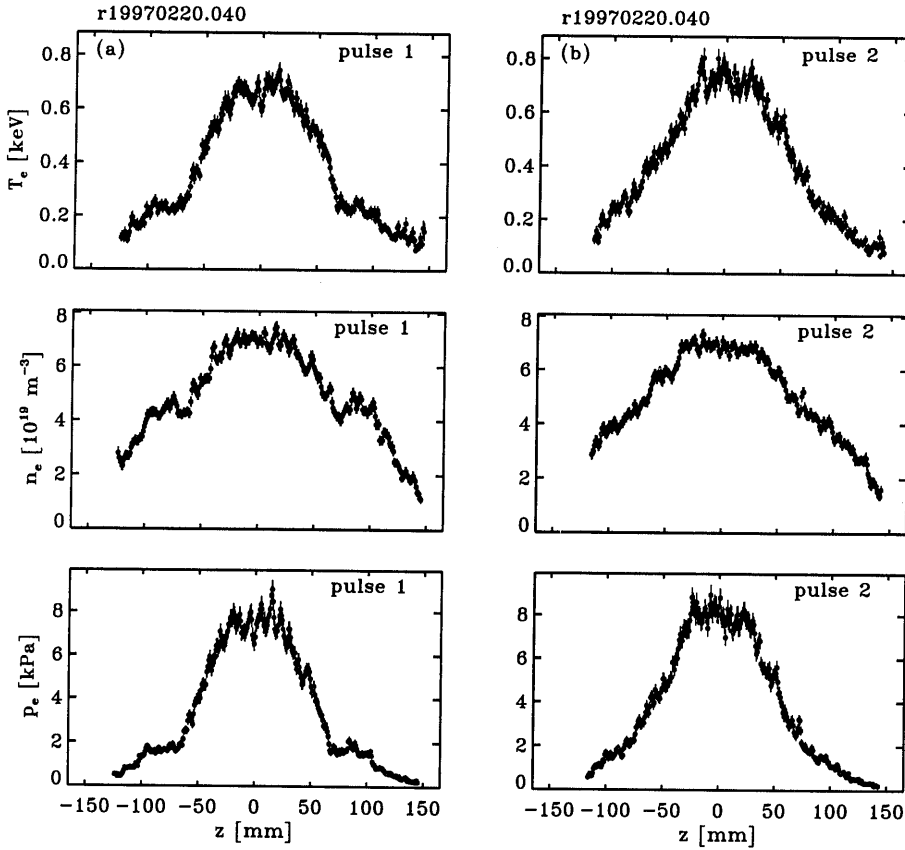
Figure 4.15: *Profiles of T_e, n_e, p_e obtained from the spectra in Fig. 4.13 with $\Delta t = 75\mu s$. (a) Camera 1 (b) Camera 2. The first pulse shows the footprints of two large $m=2$ islands. In the second pulse the $m=2$ islands have rotated and show the X-points of the islands on the TS profiles. (see section 4.5.1).*
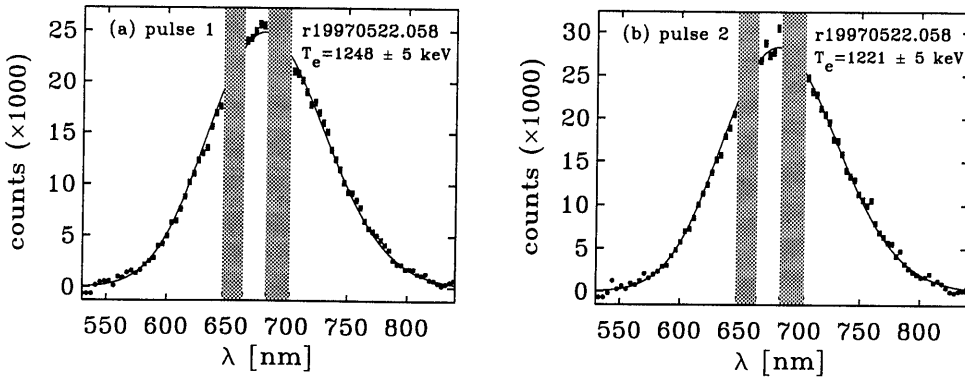
Figure 4.16: *Fit through the average of 85 spectra from one discharge with a flat central temperature of $T_e \approx 1.2$ keV. (a) camera 1 and (b) camera 2. Note that the deviations between the data and the fits are very small.*

To show the good calibration of the system 85 TS spectra of one discharge with a flat central $T_e \approx 1.2\,\text{keV}$ and $n_e \approx 3.5 \times 10^{19}\text{m}^{-3}$ were added to reduce the random error, and fitted (see Fig. 4.16). The discharge used for this purpose is a centrally ECH heated plasma with a higher T_e than the discharge in Fig. 4.15. The time separation was set to $\Delta t = 0\,\mu s$, i.e. both cameras take a picture of the same image. For both cameras the fitting function follows the data very well.

4.4   Experiments: measurements with $\Delta t = 0\,\mu s$

Figure 4.17 and 4.18 show an overplot of the T_e and n_e profiles of a centrally ECH heated discharge. Both cameras look at the same laser pulse, i.e. $\Delta t = 0\,\mu s$. The profiles measured with both cameras agree very well. This demonstrates the quality of the two independent calibrations. In order to study the deviations more carefully 15 similar discharges were used to look at the systematic (b_{T_e} and b_{n_e}) and statistical (ζ_{T_e} and ζ_{n_e}) deviations between measurements with camera 1 and camera 2. In order to be able to compare the two measurements a spline interpolation is applied to correct for minor differences in magnification.
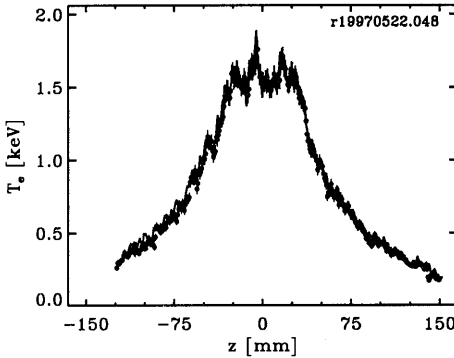

Figure 4.17: *Double detection: two T_e profiles taken at the same time, i.e. $\Delta t = 0\,\mu s$, with camera 1 (dots) and 2 (line). The bias b_{T_e} and the statistical deviation ε_{T_e} between the profiles lie well within the error-bars (see Fig. 4.19 and 4.21).*
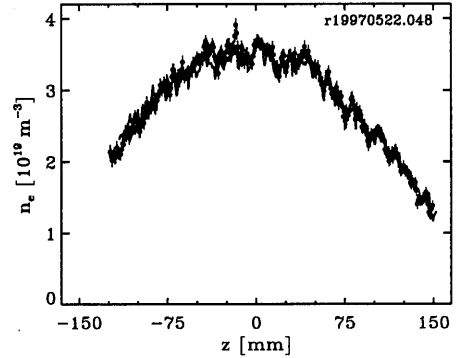
Figure 4.18: *Double detection: two n_e profiles taken at the same time, i.e. $\Delta t = 0\,\mu s$, with cameras 1 (dots) and 2 (line). The bias b_{n_e} and the statistical deviation ε_{n_e} between the profiles lie well within the error-bars (see Fig. 4.20 and 4.22).*

The definition for the systematic deviation, the bias b_{T_e} on T_e, averaged over 15 discharges is as follows:

$$b_{T_e} = \frac{1}{15} \sum_{i=1}^{15} (T_{e,1,i} - T_{e,2,i}), \tag{4.6}$$

where $T_{e,1,i}$ and $T_{e,2,i}$ indicate the 15 T_e profiles for camera 1 and 2. This bias can be compared to σ_{T_e}, the quadratic sum of the error bars on T_e for both cameras:

$$\sigma_{T_e} = \sqrt{\sigma_{T_e,1}^2 + \sigma_{T_e,2}^2}, \tag{4.7}$$

where $\sigma_{T_e,1}$ and $\sigma_{T_e,2}$ represent the average error bars of the 15 discharges for camera 1 and 2. The same expression for the bias, b_{n_e}, and σ_{n_e} can be made for n_e.
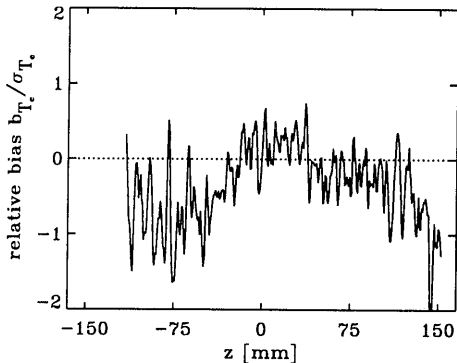
Figure 4.19: *Bias* b_{T_e} *of the* T_e *profiles of camera 1 with respect to camera 2. The deviations lie well within the error bars. At the edges the* T_e *determination by camera 2 lies above the determination by camera 1 by less then 1* σ_{T_e}
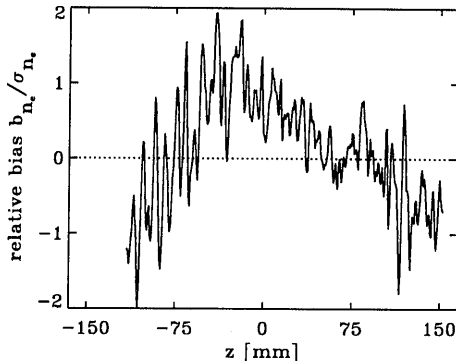
Figure 4.20: *Bias* b_{n_e} *of the* n_e *profiles of camera 1 with respect to camera 2. The deviations lie within 1* σ_{n_e}. *They are due to a slight mis-alignment of the laser beam in relation to the entrance slit.*

Figures 4.19 and 4.20 show the systematic deviations b_{T_e} and b_{n_e} normalised to σ_{T_e} and σ_{n_e}. In the ideal case the bias is zero, as it is for T_e in the central part. The biases on T_e and n_e stay within one σ_{T_e} and σ_{n_e} for the whole z-range.

The shot-to-shot deviations are given by the statistical deviation ζ_{T_e} (n=15):

$$\zeta_{T_e} = \sqrt{\frac{1}{15}\sum_{i=1}^{15}\left(T_{e,1,i} - T_{e,2,i} - b_{T_e}\right)^2} \tag{4.8}$$

ζ_{T_e} is corrected for the systematic deviation b_{T_e}. The same definition ζ_{n_e} is used for the statistical deviation on n_e. The statistical deviation between the two cameras should only be due to noise from the ICCD intensifiers and the CCD chip. Noise at the first intensifier, Fig 4.2, item 10, is correlated in the two measurements with $\Delta t = 0\,\mu s$ and should cancel out in the comparison. As shown in section 4.3.2 the first intensifier determines over 90 % of the noise on the spectra. In the ideal case the statistical deviation between the cameras should be $\sim 0.1 \cdot \sigma_{T_e}$ and $\sim 0.1 \cdot \sigma_{n_e}$. Fig. 4.21 and 4.22 show the relative statistical deviation on T_e and n_e. Both curves show a similar behaviour. The minima of the curves lie close to the optical axis of the system, i.e. z=+25 mm (Fig. 4.2). Here ζ_{T_e} and ζ_{n_e} are $\sim 0.5\,\sigma_{T_e}$ and $\sim 0.5\,\sigma_{n_e}$, respectively. Towards the edge the deviations approach σ_{T_e} and σ_{n_e}. Over the whole range the statistical deviations are larger than the expected $0.1 \cdot \sigma_{T_e}$ and $0.1 \cdot \sigma_{n_e}$. As mentioned above a spline interpolation is used to match the z-calibrations of both cameras. A small deviation (~ 1 pixel) in the match in position decreases the correlation of the noise on both profiles, and thus increases the statistical deviation between the two.

To summarize, for settings of $\Delta t \neq 0\,\mu s$ differences between the profiles of camera 1 and 2 are significant if the deviations on T_e and n_e are $> \sigma_{T_e}$ and $> \sigma_{n_e}$, respectively.
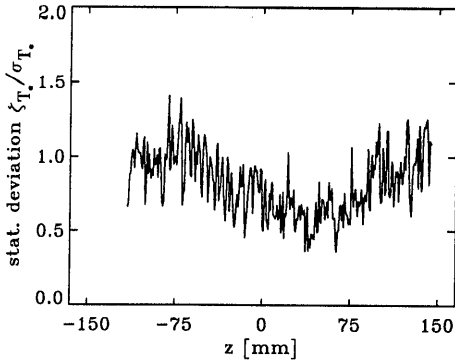
Figure 4.21: *Statistical deviation ε_{T_e} of T_e profiles measured by camera 1 and 2. ε_{T_e} is below σ_{T_e} over the whole z-range. The minimum deviation lies around the center of the detection system (z=+25 mm).*
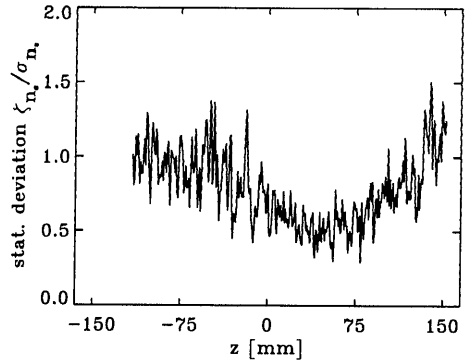
Figure 4.22: *Statistical deviation ε_{n_e} of n_e profiles by camera 1 and 2. ε_{n_e} is below σ_{n_e} over the whole z-range. Also here the minimum deviation lies around the center of the detection system (z=+25 mm).*

4.5   Plasma physical results

In this section, four examples of measurements with the TS diagnostic are given to illustrate the possibilities of the diagnostic: (1) Rotating MHD modes in an Ohmic discharge. (2) Filaments before and after a sawtooth crash in ECH heated plasmas. (3) Transient heating effect of the plasma center during edge cooling with oblique pellet injection. And (4), detailed profile information before and after an off-axis sawtooth crash.

4.5.1   Identification of large and small MHD modes using the plasma rotation

In high density Ohmic discharges, large m=2 activity has been observed in RTP. The mode is stable for over hundreds of ms, as can be seen on the magnetics. It has a rotation period of τ_{MHD} of 150 μs. Figure 4.15 gives an example of T_e, n_e and p_e profiles taken in such a discharge. The figure shows a m/n=2/1 island turning from showing its O-point to showing its X-point in the TS measurements. The time separation between the two pulses was set to Δt=75μs, i.e. $\frac{1}{2}\tau_{MHD}$. As can be seen in Fig. 4.15, the island has a clear local maximum in n_e. The profiles of T_e and n_e combine to a flat p_e-profile inside the island. Using the plasma rotation and setting Δt to a fraction of τ_{MHD}, allows a mode analysis of the structures seen on the profiles.
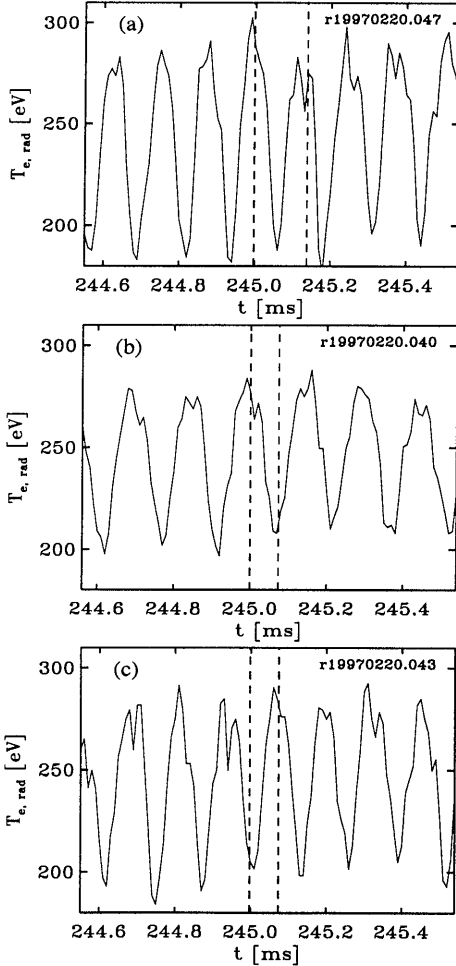
Figure 4.23: *Radiation temperature measured by ECE taken close to the m=2 island. The vertical lines show the timing of the two TS pulses for each discharge. (a) $\Delta t \approx 1.1 \times \tau_{MHD}$. The two laser pulses are fired at the maximum of the ECE signal, i.e. through the O-points of the m=2 island, see Fig. 4.24. (b) $\Delta t \approx \frac{1}{2} \times \tau_{MHD}$ and first pulse at maximum and second at minimum of the ECE signal. (c) $\Delta t \approx \frac{1}{2} \times \tau_{MHD}$ with the first at the minimum and the second at the maximum of the ECE. Plasma parameters in all three cases are: $q_a = 5.2$, $n_e(0) \approx 6.5 \times 10^{19}$ m^{-3}*
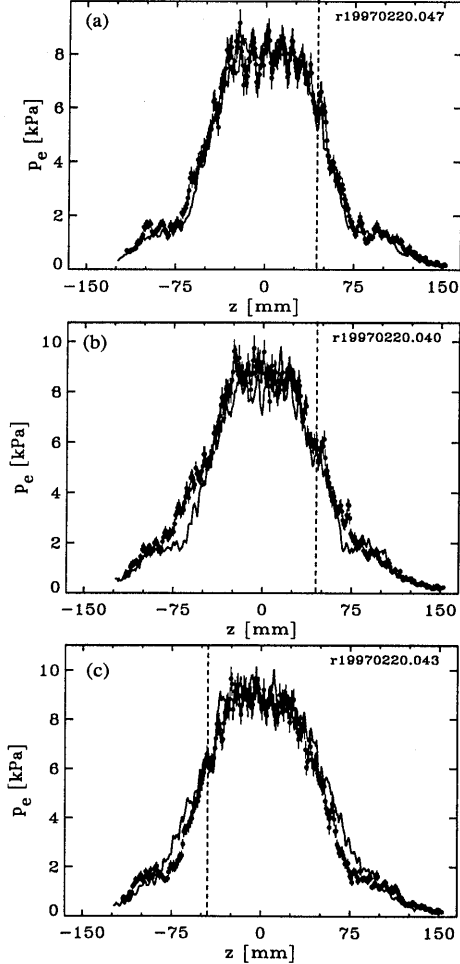
Figure 4.24: *Double pulse TS measurements of the discharges in Fig. 4.23. (a) p_e profiles taken with $\Delta t \approx 1.1 \times \tau_{MHD}$. The first pulse is plotted as a line, the second as dots and error bars. The m/n=2/1 islands around $|z| = 80\,mm$ reproduce very well in the profiles. (b) $\Delta t \approx \frac{1}{2} \times \tau_{MHD}$. Here the O-point of the m/n=2/1 island rotates from showing its O-point (line) to showing its X-point (dots) (c) $\Delta t \approx \frac{1}{2} \times \tau_{MHD}$ as well. The m/n=2/1 islands here rotate from showing its X-point (line) to showing its O-point (dots). All three discharges show a reproducing odd mode: (a) and (b) at z=+45 mm and (c) at z=-45 mm.*

Figures 4.23 and 4.24 show three examples of double pulse TS measurements in similar high density plasmas. Figure 4.23 shows the timing of the TS laser in relation to the island rotation, and Fig. 4.24 shows the corresponding p_e profiles. In the first discharge the TS separation time is set to $\Delta t = 1.1 \times \tau_{MHD}$, and in the second and third to $\Delta t = \frac{1}{2}\tau_{MHD}$. In the case of $\Delta t = 1.1 \times \tau_{MHD}$ the profiles reproduce very well. Not only the m=2 mode around $|z| = 80$ mm, are very similar in both profiles, also smaller structures like the odd mode in the steep gradient at z=+45 mm, and the complicated p_e structures in the center appear very similar. The central part of the profiles is enlarged in Fig. 4.25. The agreement is not perfect, which may be caused due to the fact that the rotation time τ_{MHD} is not perfectly matched by Δt. Of course, also dynamics of the structures may be the cause of the difference. Still, the fact that many structures appear in the same relative positions after a single toroidal turn demonstrates that the plasma may be regarded as a rigid rotator.
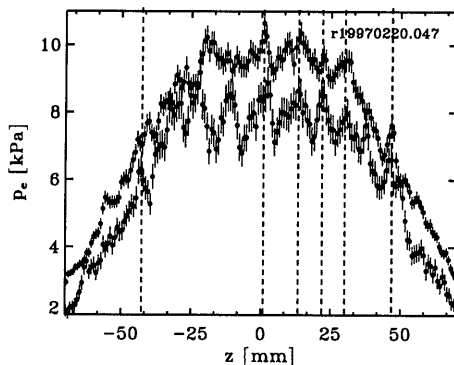
Figure 4.25: *Enlargement of the central part of the profiles in Fig.4.24 (a). The first pulse is shifted up. The vertical lines indicate the maxima of structures that reproduce in both profiles. Note that the agreement is not perfect (see text). The odd mode (m/n=3/2) at z=45 mm is visible on both profiles.*

Figures 4.24 (b) and (c) show the discharges in which Δt is set to $\frac{1}{2}\tau_{MHD}$. The first of the two shows the m/n=2/1 island rotating from showing its O-points to showing its X-points (this is the discharge of Fig. 4.15), while the second shows rotation of the m/n=2/1 island from showing its X-points to showing its O-points (see Fig 4.23 for the timing of the TS pulses). However in Fig. 4.24 (b) the odd mode in the steep gradient, at z=+45 mm, has returned to the same position, demonstrating that this mode must have n=even, with an n=2, m=3 mode as the most likely candidate. In Fig. 4.24 (c) the odd mode sits on the other side of the profile at z=-45 mm, showing that the structure is not a systematic deviation in p_e. Here it also reproduces after $\frac{1}{2}\tau_{MHD}$, showing the n=even character of the mode, with again n=2, m=3 as the most likely candidate. In this way an m/n=3/2 mode has been identified using double pulse TS.

4.5.2   TS in plasmas with central sawteeth

In this section two examples are given of TS during a central sawtooth collapse. Both examples concern Electron Cyclotron Current Driven (ECCD) discharges in which the

ECH was launched under an angle with the toroidal magnetic field B_T. A distinction is made between *counter-* and and *co-*ECCD. In the case of counter-ECCD the ECH is launched in the direction anti-parallel, and in the case of co-ECCD in the direction parallel to the inductively driven current. In both examples the plasma parameters are I_p=60 kA, q_a=5.8, $n_e(0)$= 1.5×10^{19}m^{-3}. The current is kept constant using a current feedback control system.

The first example deals with a counter-ECCD plasma. ECH was launched under an angle of -20° in relation with B_T, and the driven current is $\sim$-5 kA in the center of the plasma. The plasma shows large sawtooth activity with a long saturation phase and a period of $\sim$ 4 ms (see Fig. 4.26). Double pulse TS measurements are taken with one pulse just before and one just after a sawtooth collapse. Figure 4.27 shows the two TS T_e profiles. The profile before the crash is filamented, i.e. it has narrow T_e peaks, and has a high central T_e. The crash is $\sim$ 1 keV deep, and the T_e profile after the crash is much flatter. It shows the heat deposition in the outer region of the profile.
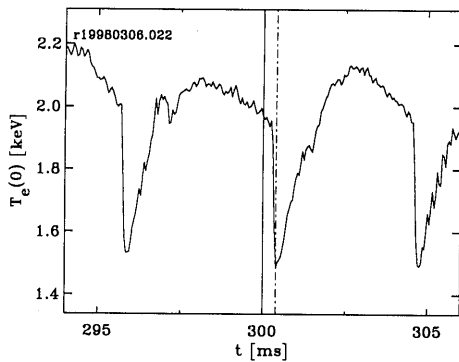
Figure 4.26: *Central ECE channel of a sawtoothing counter-ECCD plasma. The vertical lines indicate the timing of the TS laser in relation with the sawtooth phase; just before and just after the crash. The two TS pulse were taken in the same discharge.*
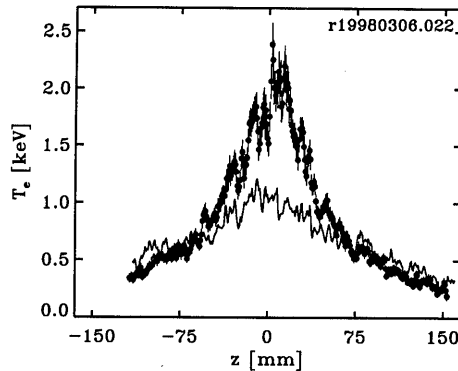
Figure 4.27: *TS profiles before and after a sawtooth crash in a counter-ECCD plasma. The crash is as deep as $\sim$ 1 keV. The profile before the crash shows filaments in the center. The lower profile shows the heat pulse going out.*

For the second example with co-ECCD unfortunately no double pulse measurements are available. Instead three profiles are shown of well reproducing discharges (see Fig. 4.28). The plasmas show non-saturated sawteeth with a period of $\sim$ 1.3 ms. The EC waves are launched under an angle of +20° with respect to B_T, as a consequence of which a current of roughly 10 kA is driven in the center of the plasma. Figure 4.28 shows the central ECE channel of one of the discharges. It indicates the timing of the TS laser for the three discharges, in relation to the sawtooth collapse. Figures 4.28 (a)–(c) show the three T_e profiles. The profile in Fig. 4.28 (a) is taken just before the crash. It has high central T_e and is filamented. The filaments have a width of 5–10 mm each and are 500–700 eV high. Figure 4.28 (b) is measured during the sawtooth crash. The high spatial resolution of the TS system allows to see the detailed shape of the profile. It shows the spectacular

displacement of the hot core. The profile of (a) is overplotted for comparison. Figure 4.28 (c) shows the profile just after the crash. This profile is flatter and the amplitude of the structures in the center is lower than in (a). Outside the inversion radius the profiles (a) and (c) are very similar. No outward heat pulse is observed. This might be due to slightly different plasma parameters in the two discharges.
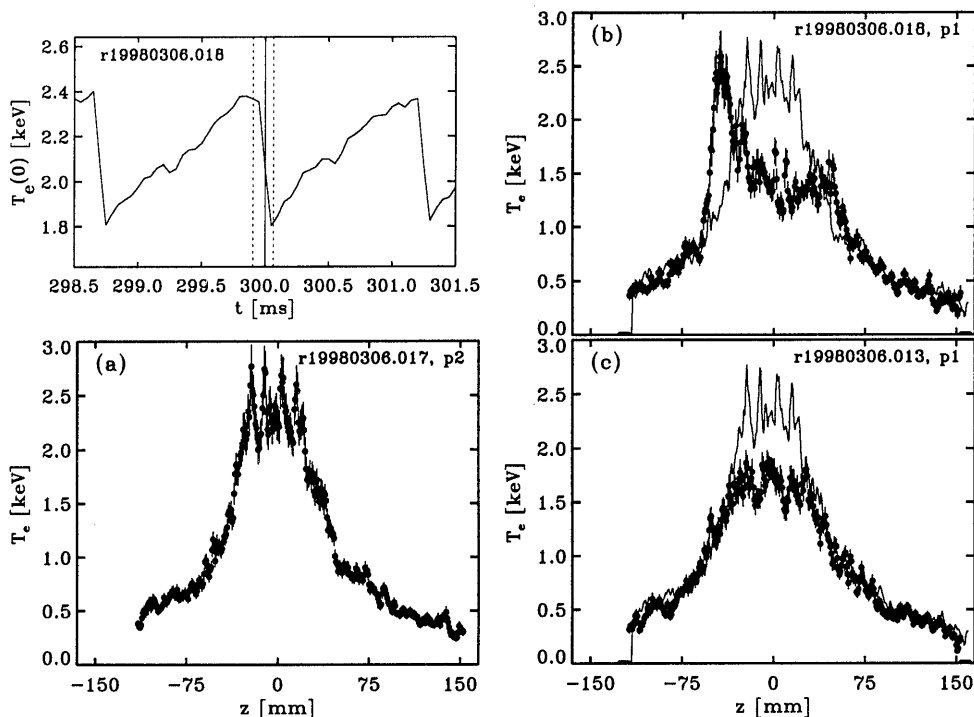
Figure 4.28: *TS profiles in different stages of a sawtooth cycle in well reproducing plasmas with ECCD. The timing of the pulses in relation to the sawtooth phase is indicated in the central ECE time trace (top left). (a) Just before the sawtooth crash, with high central T_e and a filamented core. (b) Profile inside the sawtooth crash, showing the displacement of the hot core. (c) After the sawtooth crash, showing the flattened top of the profile. The profile of (a) is overplotted in (b) and (c) as a thin line.*

4.5.3   Filaments during 'non-local' heating of an Ohmic plasma, induced by oblique pellet injection

A clear example of filaments in a non-ECH plasma is given in Fig. 4.30, which shows the T_e profile of a plasma with oblique pellet injection. A small pellet (0.6 mm diameter) is shot in and passes the plasma center at $\geq 65\%$ of the minor radius. The plasma edge cools, while in the plasma center a T_e rise is observed. This phenomenon has been observed in several tokamaks and is called 'non-local' heating, [22, 23, 24]. In RTP, such 'non-local' heating has been observedin plasmas with $2.5 \times 10^{19} \leq n_e(0) \leq 4 \times 10^{19}\,\mathrm{m^{-3}}$. Only at low densities of $n_e(0) \approx 2.5 \times 10^{19}\,\mathrm{m^{-3}}$ filaments have been observed. Figure 4.29 shows the

central ECE channel, the central line-averaged density, and the timing of the two TS pulses of the discharge shown in Fig. 4.30. The line averaged n_e increases by a factor of ~1.5 and the increase in central radiation temperature is ~10 %. The first pulse of TS is taken ~5.5 ms after the pellet injection and the second pulse 400 μs later. The first pulse, being fired just after a sawtooth-crash, shows a flat T_e profile. However 400 μs later high T_e peaks have developed. It appears, as in section 4.5.2, that the filaments are destroyed by the sawtooth crash and develop during the T_e rise.
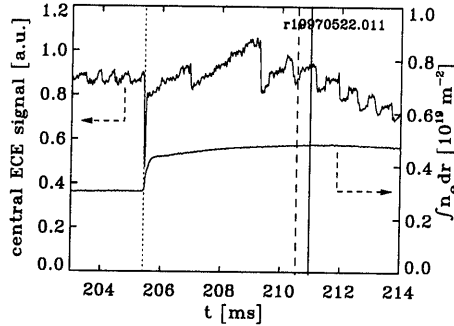
Figure 4.29: *Example of transient T_e rise after oblique pellet injection. The figure shows a central ECE trace and the line integrated density from interferometry. A pellet is shot in obliquely and enters the plasma at 205.4 ms (dotted line). The dashed lie indicates the timing of the first and the full line the timing of the second laser pulse. Transient heating of the center occurs after pellet injection, and the sawtooth activity is enhanced.*
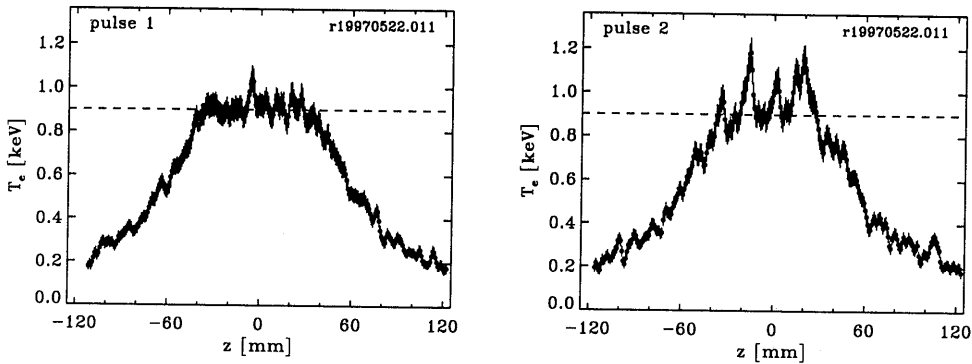
Figure 4.30: *Two T_e profiles after oblique pellet injection. The Thomson laser was fired ~ 5.5 ms after the pellet (see Fig. 4.29). The first laser pulse was shot just after a sawtooth crash (a) and the second just before the next crash (b). The first profile after the crash is nearly flat while the second is filamented. Plasma parameters: $q_a = 4.7$, $n_e(0) = 2.6 \times 10^{19}$ m^{-3}*

4.5.4 Off-axis sawteeth during off-axis ECH

In RTP, sawtooth activity has been observed with a distinct off-axis localisation, in plasmas with off-axis ECH. These instabilities have been associated with the q=3/2, 2, and

3 surfaces [15, 25, 26]. Here, examples of sawtooth activity near q=2 and q=3/2 is given. The q=2 and q=3/2 character is determined from the time evolution of different ECE channels, as discussed in [26]. Figure 4.31 shows three ECE channels of a discharge with sawteeth at the q=2 surface. It shows a central channel, a channel at the same radial position as the ECH deposition (ρ_{dep}) at $|z| \approx 50$ mm, and a channel outside the deposition region. The off-axis character of the sawteeth is illustrated by the fact that the central ECE-channel is almost silent while the channel at ρ_{dep} shows strong sawtooth activity. The outer channel shows inverse sawtoothing. Figure 4.32 shows two T_e profiles taken with the double pulse TS diagnostic with Δt=400 μs. The first profile is taken at the beginning of the saturation of a sawtooth and the second during its crash (see Fig. 4.31). The profile before the crash has developed sharp ears at the position of the ECH deposition. The crash at this radius is ~ 0.2 keV. The second profile shows that during the crash the central part of T_e is hardly affected by the instability. Outside ρ_{dep} the heat deposition is clearly visible.

Figure 4.31: *Three ECE channels of a discharge with off-axis sawteeth with a q=2 character: one central channel inside the ECH deposition radius ρ_{dep}, one channel at ρ_{dep}, and one channel outside ρ_{dep}. The central channel remains almost unchanged, while the channel at ρ_{dep} shows sawtooth activity. The outer channel shows inverse sawteeth. The vertical lines at 250.0, and 250.4 ms indicate the timing of the TS laser.*
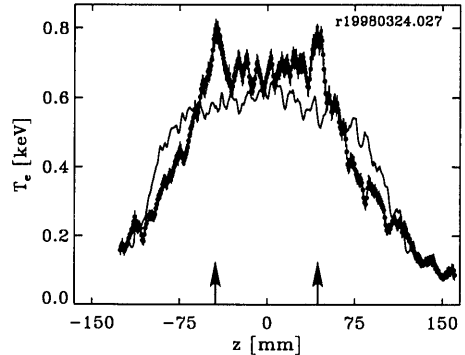
Figure 4.32: *T_e profile just before (dots) and during (line) an off-axis sawtooth crash with a q=2 character. The timing of the laser pulses is indicated in Fig. 4.31. The arrows indicate the ECH deposition region. The profile before the crash has developed off-axis ears, which occur at the same radial position as the ECH deposition. Note that during the crash these ears are chopped off, while the central T_e remains almost unchanged. Outside the deposition radius the outward heat pulse is visible.*

For the q=3/2 sawtooth case no double pulse measurements before and after the crash in a single profile are available. Therefore two well reproducing discharges are used to show the evolution of the crash. Three ECE channels are given in Fig. 4.33. The central channel shows less sawtooth activity than the channel at ρ_{dep}. The outer channel shows inverse sawtoothing. Three T_e profiles are presented in Fig. 4.34. The timing of the TS measurements is given in Fig. 4.33. Figure 4.34 shows that the profile before the crash

shows steep gradients outside the ECH-deposition radius. The profile right after the crash shows that the crash is $\sim 0.5\,$keV deep. A small central part remains almost unaffected, indicating the off-axis character of the crash. In fact the area covered by the central ECE channel ($\sim 2\,$cm) is larger than the unaffected central region in Fig. 4.34. Later, i.e. $400\,\mu s$ after the crash, T_e is rising again in the off-axis region where the crash occurred.
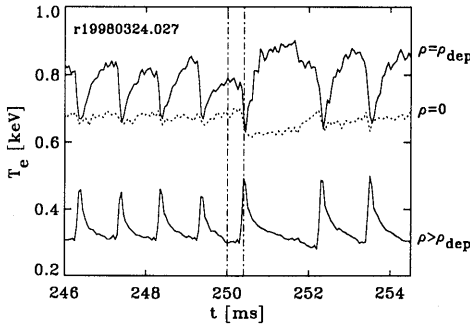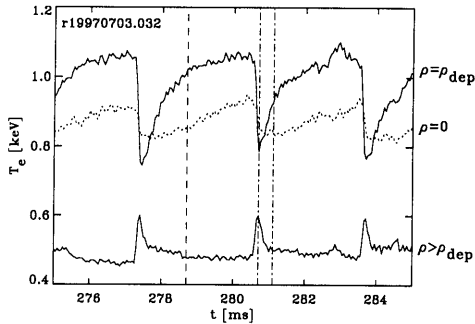

Figure 4.33: *Three ECE channels of a discharge with off-axis sawteeth with a m/n=3/2 character: one central channel inside the ECH deposition radius ρ_{dep}, one channel at ρ_{dep}, and one channel outside ρ_{dep}. The region covered by the central ECE-channel is somewhat larger than the small center part of the profiles in Fig. 4.34. The period of the instability is longer than that of ordinary sawteeth. The three vertical lines indicate the timing of the TS laser relative to the sawtooth cycle. The last two TS measurements are taken in the same discharge.*
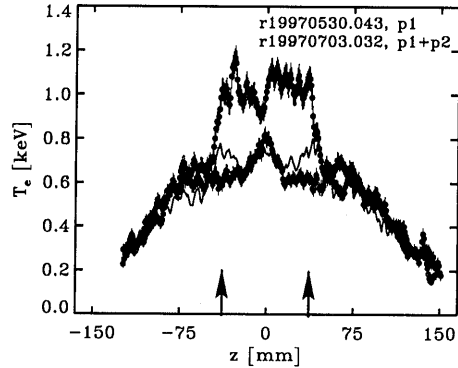
Figure 4.34: *Three T_e profiles of a discharge with q=3/2 sawteeth. The bottom two profiles are taken in the same discharge, while the top one is from a well reproducing discharge. The top profile (dots) is at the beginning of the saturation phase of the sawtooth (see Fig. 4.33). The deposition radius of the ECH is indicated with arrows. The bottom profile(also dots) is taken just after the crash and the middle one (line) $400\,\mu s$ later. In the latter profile the area around the ECH deposition is heating up again. Note that a small central part remains unaffected.*

4.6 Summary and discussion

A double pulse multiposition TS diagnostic has been constructed and extensively tested. The aim of this diagnostic is to measure small scale structures in T_e and n_e profiles with a size down to a few mm. The double pulse feature enables the study of the dynamics of these small scale structures. The temporal separation between the two pulses can be varied from 20 to 800 μs, which is of the order of periodic plasma processes such as plasma rotation, ~ 50–$200\mu s$, and sawtooth activity, $\sim 500\,mus$–2 ms. Almost the full cross section of 330 mm of the plasma is covered; a laser chord of 300 mm length is viewed. The chord is covered with 350 points and the spatial resolution is $\sim 3\,$mm, i.e. 3.5 measurement points. The spatial resolution of the instrument is thus 2 % of the plasma minor radius.

The statistical errors on the measured T_e and n_e are small, i.e. a relative error of 3–5 % on T_e in the range of $50\,$eV$< T_e <6\,$keV at $n_e = 5 \times 10^{19}\,$m^{-3}. The relative error

on n_e in that case is even smaller: 2–4 %.

Measurements with separation time $\Delta t = 0\,\mu s$ have been performed. This enables a comparison of the T_e and n_e profiles obtained with the two detection branches. Both the systematic bias and the statistical deviation between the two cameras are below σ_{T_e} and σ_{n_e} for T_e and n_e respectively.

Measurements with $\Delta t \neq 0\,\mu s$ have been performed in different plasma experiments. A large m/n=2/1 island of $\sim 3\,cm$ wide is visible on the TS profiles (see section 4.5.1). The resolution of the TS system is so good that a detailed profile inside the island is resolved. The density n_e shows a local maximum inside the island. This maximum in n_e in large m/n=2/1 islands has also been observed by De Vries at the Textor tokamak, [27], using a pulsed radar diagnostic. Double pulse measurements at $\Delta t = \tau_{MHD}$ and $\frac{1}{2} \times \tau_{MHD}$ show the reproduction of the m/n=2/1 island and the island turning from showing its O-point to showing its X-point, respectively. Using the plasma rotation and setting Δt to half integer values of the rotation a much smaller m/n=3/2 mode has been identified. Identification of MHD modes applying TS has also been performed at other tokamaks; at JET by Nave [11], and at JFT-2M by Yamauchi [28]. Also at the W VII-A stellarator small islands have been observed applying TS [29].

Filaments are seen in centrally heated plasma applying ECH, section 4.5.2, and [14]. After a central sawtooth crash the filaments amplitude has decreased. A TS measurement inside the sawtooth crash shows the detailed profile of the displacement of the hot core. This displacement has been observed with lower spatial resolution in tomographic reconstructions of soft X-ray measurements, e.g. [30]. Filaments have also been observed in plasmas without ECH heating, section 4.5.3. In these plasmas a transient central T_e rise occurs because of edge cooling with a pellet, [23, 24]. The plasma center is filamented, indicating that no strong localised heating source is required to induce plasma filaments. Also in this case the filament amplitude was highly reduced after a sawtooth crash.

Finally, detailed T_e profiles before and after off-axis sawtooth crashes with a distinct off-axis character are given in section 4.5.4. Examples are given of sawtooth crashes with a $m/n=2/1$ and 3/2 character. At RTP off-axis sawtooth crashes have been observed at rational values of q of 2, 3/2 and 3 [26]. All these crashes occurred in off-axis heated discharges. Also at other tokamaks off-axis sawtooth like phenomena have been observed [31, 32, 33]. None of them has a good profile measurement of the crash. Thanks to the double pulse multiposition TS, at RTP the topology of the crash can be seen in great detail.

A TS system similar to the RTP system is currently in operation at the TJ-II stellarator. The TJ-II system has been developed at the FOM-Instituut voor Plasmafysica 'Rijnhuizen' in the Netherlands and is adapted to specific needs at TJ-II [34]. A new high resolution multiposition TV TS system is currently under development for the TEXTOR tokamak, as part of the Trilateral Euregio Cluster (TEC).

4.7   Acknowledgments

nostic. The authors also would like to thank the RTP-team for very efficient operation of the machine and diagnostics. In particular, all members of the TS operator team are thanked for excellent operation of the TS diagnostic. The development, construction and operation of the TS diagnostic would not have been possible without the the professional help of the drawing office, the machine workshop, and the software engineering group.

Appendices

4.8 Appendix A: theoretical Thomson scattering spectrum

The theoretical TS spectrum according to Mattioli is:

$$F(\lambda) = \frac{a_0}{2\sqrt{\pi}\,\sin\left(\frac{\theta}{2}\right)\lambda_0\,a_1\,X(a_1)}\,Y(\Lambda)\,\exp\frac{-Z(\Lambda)}{a_1^2} \tag{4.9}$$

with:

$$\Lambda = \frac{\lambda_0}{\lambda}$$

a_0 = surface of Gaussian if it were non-relativistic.

$$a_1 = \frac{1}{c}\sqrt{\frac{2k_b T_e}{m_e}} = \frac{v_{th}}{c}$$

$$X(a_1) \approx 1 + \frac{15}{16}a_1^2 + \frac{105}{512}a_1^4$$

$$Y(\Lambda) = \frac{2\sin\left(\frac{\theta}{2}\right)\Lambda^4}{\sqrt{1 - 2\Lambda\cos\theta + \Lambda^2}}$$

$$Z(\Lambda) = \frac{\sqrt{\Lambda - 2\cos\theta + \Lambda^{-1}}}{\sin\left(\frac{\theta}{2}\right)} - 2$$

Here, λ_0 is the ruby laser wavelength at 694.3 nm, k_b the Bolzmann constant, m_e the electron rest mass, v_{th} the electron thermal velocity and c the speed of light.

4.9 Appendix B: data correction and calibration

Before fitting the raw measured TS spectra they should undergo a list of corrections and calibrations. Chronologically correcting and calibrating the data goes as follows:

- Background subtraction: The CCD's dark-current gives an off-set to the data. A plane is fitted to the area of the CCD-image where no signal is recorded, and subtracted from the signal.

- Laser energy determination: a small area of the CCD is used to record laser light picked up with a fiber at the laser-beam exit window of the tokamak. The intensity of this signal is used to determine the laser pulse energy.

- Image tilt correction: The spherical mirror is tilted with respect to the detection plane, see Fig. 4.2. This tilt causes a deformation of the image of the mirror on the CCD; Horizontal lines on the mirror result into diverging lines in its image on the CCD. The effect of the tilt of the mirror is corrected by means of software, such that horizontal lines on the mirror are represented by horizontal lines on the CCD. The topic is discussed in [16].

- Binning: four pixels are binned in the wavelength direction: Transform the CCD-pixels $(i,j) \longrightarrow (i_b, j)$.

- Wavelength and position–calibration: Transform the CCD-pixels $(i_b, j) \longrightarrow (\lambda, z)$, i.e. (wavelength, position).

- Correction for the slow P20 phosphor decay for camera 2 (optionally): The long tail of the phosphor emission decay causes an overlap of the signals of pulse 1 and 2 in the second recording. the signal of camera 2 is corrected using the phosphor decay, Fig. 4.4, at the preset separation time Δt, and the signal of camera 1. Spline interpolation is applied to correct for a small difference in magnification of the images.
  For separation times $\geq 100 \mu s$ this correction is skipped.

- CCD-mask: the area of the CCD-image outside the image of the spectral mirror is set to zero. On top of that line emission from the plasma such as the H_α Balmer line at 656.3 nm are cut out of the data by means of software. When He is puffed in the plasma also the He lines at 587.6 and 667.8 nm are cut out.

- Relative calibration: the measurements of the relative spectral sensitivity, of section 4.2.5, are used in order to calibrate the pixel sensitivity.

- 1th order approximation of the instrument profile. The instrument profile of the diagnostic has a very long tail. This tail causes a more or less homogeneous background level to the signal. As a 1th order correction for this background a certain fraction ($4 \cdot 10^{-6}$) of the total CCD image is subtracted from the spectra, [21]. The correction fraction is the same for both cameras, since their instrument profiles are very similar.

The data is now ready to be fitted. the non-linear least square fitting algorithm and the weight function of section 4.3.2 are used to fit the theoretical spectral shape equation (4.9) to the data. The fitting is performed in two iteration loops. In the first iteration loop the full spectral range from 530 to 840 nm is used. This loop gives a first estimate for the width and the amplitude of the spectrum. These parameters are used as starting parameters for the second iteration loop. In this loop only the part of the spectrum within the $2 \times 1/e$ width is used, containing >99 % of the recorded photons. This cut-off range is a trade off between good statistics and minimization of influence of background noise and signals, and has been determined empirically.

References

[1] A.J.H. Donné, Plasma Phys. Reports **20** (1994) 192

[2] N.J. Lopes Cardozo, *et al.*, Plasma Phys. and Controlled Fusion **37** (1995) 799-852.

[3] P.C. Liewer, Nucl. Fusion **25** (1985) 543.

[4] B.B. Kadomtsev, 'Tokamak plasma: a complex physical system' (Adam Hilger, Bristol and New York, 1992)

[5] H. Salzmann, *et al.*, Rev. Sci. Instrum. **59**, 1451 (1988).

[6] T.N. Carlstrom, *et al*, Rev. Sci. Instrum. **63**, 4901 (1992)

[7] H. Murman, *et al.*, Rev. Sci. Instrum. **63**, 4941 (1992)

[8] D. Johnson, *et al.*, Rev. Sci. Instrum. **57**, (1986) 1856

[9] T. Yamauchi, *et al.*, Proc. 20th EPS Conf. on Controlled Fusion and Plasma Physics, (Lisboa 1993) Part III, p 1195-1198.

[10] C.J. Barth *et al.*, Rev. sci. Instrum. **68** (9), (1997) 3380-3392.

[11] M.F.F. Nave, *et al.*, Nucl. Fusion **32** (1992) 825.

[12] R.E. Stockdale, *et al.*, Rev. Sci. Instrum. **66**, 490 (1995)

[13] C.J. Barth, 'High spatial resolution Thomson scattering at hot plasmas.' Proc. 8th symposium on Laser aided plasma diagnostics, p197-210.

[14] N.J. Lopes Cardozo, *et al.*, Phys Rev. Letters **73** (1994) 256-259.

[15] N.J. Lopes Cardozo, *et al.*, Plasma Phys. Control. Fusion **39**, suppl. 12B, (1997) B303-B316.

[16] C.C. Chu *et al*, 'Calibration procedure and data processing for the multiposition Thomson scattering system at RTP', to be published.

[17] J.C. de Vos, Physica **20**, 690 (1954).

[18] M. Mattioli, 'Incoherent light scattering from high temperature plasmas', EUR-CEA-FC-752 (1974).

[19] M.N.A. Beurskens, *et al.*, Rev. Sci. Instrum. **68** (1) (1997) 721–724.

[20] P.R. Bevington, 'Data reduction and error analysis for the physical sciences', ISBN 69-16942.

[21] M.N.A. Beurskens, *et al.*, 'Error analysis of RTP Thomson scattering data', to be submitted to Rev. Sci. Instrum.

[22] K.W. Gentle,*et al.*, Phys Rev. Letters **74** (1995) 3620.

[23] P. Mantica, *et al.*, Proc. 24th EPS Conf. on Controlled Fusion and Plasma Physics, (Berchtesgaden 1997) Part IV, p 1853-1856.

[24] J.D. Callen and M.W. Kissick. Plasma Phys. Control. Fusion **39** (1997) B173–B188.

[25] M.R. de Baar, *et al.*, Phys Rev. Letters **78** (1998) 4573–4576.

[26] R.F.G. Meulenbroeks, *et al.*, 'Steady state off-axis sawtoothing near q=3/2, 2, and 3 in a Tokamak', submitted to Phys Rev. Letters.

[27] P.C. de Vries, *et al.*, Nucl. Fusion, **37** (1997) 1641-1646.

[28] T. Yamauchi, *et al.*, Phys. letters A, **223** (1996) 179-185.

[29] R. Jaenicke, *et al.*, Nucl. Fusion, **28** (1988) 1737-1750.

[30] R.S. Granetz, *et al.*, Nucl. Fusion, **25** (1985) 727-732.

[31] Z. Chang, *et al.*, Phys. Rev. Letters **77** (1996) 3553–3556

[32] S. Turlur, *et al.*, Proc. 22th EPS Conf. on Controlled Fusion and Plasma Physics, (Bournemouth 1995) Part IV, p 073-076.

[33] P. Burrati, *et al.*, Plasma Phys. Control. Fusion **39** (1997) B383–B394.

[34] C.J. Barth, *et al.*, 'High resolution multiposition Thomson scattering for the TJ-II stellerator', accepted for publication in Rev. Sci. Instrum.

Chapter 5

Error Analysis of RTP Thomson Scattering Data

Authors: M.N.A. Beurskens, C.J. Barth, C.C. Chu[†], and N.J. Lopes Cardozo
† Current address: King George V avenue, Durban 4001, South Africa.

Abstract

At the Rijnhuizen Tokamak project a double pulse multiposition Thomson scattering diagnostic has been operational since 1996. It has been installed for the study of small scale structures in electron temperature (T_e) and density (n_e). This diagnostic measures T_e and n_e with high spatial resolution (3 mm FWHM i.e. 2 % of the minor radius) and high accuracy (3–5 % of T_e and 2–4 % of n_e in the range of 50 eV–6 keV and $n_e = 5 \times 10^{19}$ m^{-3}.) In this paper an extensive error analysis is performed on both statistical and systematic deviations. It is found that the instrument function of the detection branch has a smoothing effect on the noise. This reduces the statistical error on the T_e and n_e measurements on each spatial position, because the resolution of the instrument is oversampled. The long tail of the instrument profile of the entire diagnostic has significant effect on the systematic deviations in the T_e and n_e determination. However, it does not affect the relative size of the small scale structures on T_e and n_e, and for this this reason does not hamper the study of these structures.

5.1   Introduction

The tokamak is considered as one of the most promising devices for future nuclear fusion electricity plants. In a tokamak a thermonuclear plasma is confined in a helical toroidal magnetic field configuration. Part of the field is generated by a toroidal electric current through the plasma, which also heats the plasma (Ohmic heating). An outstanding issue in the fusion research is the anomalous loss of heat in the plasma which threatens the economic feasibility of the fusion reactor.

The research program of the Rijnhuizen Tokamak Project (RTP) concentrates on the anomalous heat conductivity, with emphasis on the role of magnetic structures. For this reason, the tokamak [R/a = 0.72/0.165 m, $B_T \leq 2.5$ T,$I_p \leq 150$ kA, $q_a \geq 2$] is equipped with strong localised additional heating and high resolution diagnostics. The additional heating is Electron Cyclotron Heating (ECH) (~350 kW) with localised power deposition within ~10 % of the minor radius a. The additional heating power is an order of magnitude larger than the integrated Ohmic heating power, and locally exceeds the Ohmic power even by two orders of magnitude. In an additionally heated plasma in RTP, electron temperatures (T_e) are up to 4 keV at an electron density (n_e) of 2×10^{19}m^{-3}, while in a typical Ohmic plasma the central T_e reaches 0.7 keV. The ECH power can be modulated to induce heat waves in the plasma, which are used in heat conduction studies.

A comprehensive set of high resolution electron diagnostics [1] is used to measure transport phenomena. These include a 20 channel Electron Cyclotron Emission (ECE) radiometer measuring T_e along a horizontal line, a 16 channel ECE imaging diagnostic measuring T_e along a vertical line, a 19 channel FIR interferometer, and an 80 channel 5 camera soft X-ray tomographic system. Of these, the ECE systems offer the best spatial resolution of ≥ 1.3 cm, i.e. 8 % of a. The spatial resolution of these time resolving diagnostics suffices to study transport phenomena such as heat pulse propagation.

On the basis of measurements of density fluctuations in many tokamaks (see e.g. [2]) as well as theoretical considerations of magnetic islands (e.g. [3]) it may be expected that structures in T_e or n_e with a size down to the ion Larmor radius (ρ_i) could be expected in tokamak plasmas. In RTP $\rho_i \sim 1$ mm, which is 0.5 % of a. Clearly, the spatial resolution of above mentioned diagnostics is not good enough to resolve these small structures. Therefore, next to the time resolving diagnostics, RTP is equipped with an ultra high spatial resolution Thomson scattering system.

The RTP Thomson Scattering (TS) diagnostic measures T_e and n_e at 350 points along a vertical chord of 300 mm with a spatial resolution of 3 mm, i.e. 2 % of a, approaching the required resolution of ρ_i. Next to high resolution a high accuracy of the measurements is required. The TS diagnostic measures T_e and n_e with an accuracy of 3–4 % of T_e and 2–3 % of n_e in the range of 50 eV–6 keV at a density of $n_e = 5 \times 10^{19}$ m^{-3}. Figure 5.1 and 5.2 give typical examples of high spatial resolution and high accuracy measurements of T_e and n_e with this diagnostic.

Figure 5.1 shows an example of a T_e profile of an ECH plasma with small central peaks, called filaments, of a width of 5–10 mm and amplitude up to 1 keV. Next to the high T_e peaks, steep T_e gradients are visible at |z|= 40 mm. An example of a n_e profile is given in Fig. 5.2. This is the n_e profile of a high n_e Ohmic discharge with large m=2 activity. The m=2 islands are clearly visible around |z|= 80 mm. Even the profile inside the islands is visible. More examples of the application of the instrument can be found in [6-13]

The RTP TS system is extensively described in two publications [4, 5]. A reliable estimation of the statistical errors is important for the study of the small scale structures. For this reason, in this paper an error analysis of the T_e and n_e measurements is performed. In section 5.2 the system is described briefly. In section 5.3 the error on the raw TS spectra is determined. Section 5.4 shows the propagation of this error in the error on the T_e and n_e determination, using simulations of TS spectra. The error on T_e and n_e derived from these simulations are compared to the error on T_e and n_e determined in the real experiment in section 5.5. Finally, an estimation of the systematic deviations in the T_e and n_e determination is made in section 5.6.
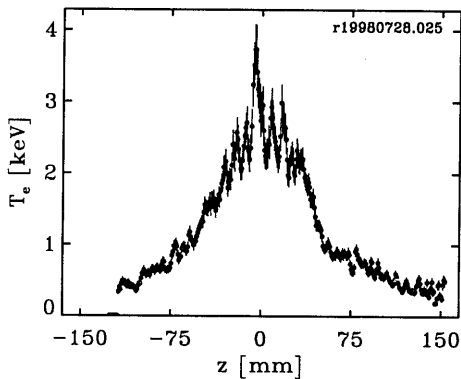
Figure 5.1: *Example of a T_e profile during additional ECH. Thanks to the high spatial resolution of TS, the filamented character in the center of the plasma and the steep T_e gradients at $z=\pm 40\,mm$ can be observed.*
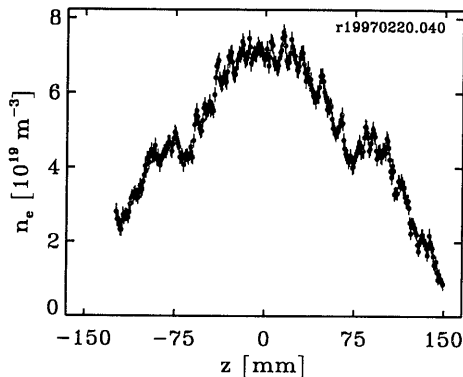
Figure 5.2: *n_e profile of a high density Ohmic discharge. The profile inside the m=2 islands (z=±80 mm) is clearly visible. Also smaller structures are significant.*

5.2 Overview of the diagnostic

The system is briefly described here. An extensive description can be found in [4, 5]. Figure 5.3 shows the layout of the double pulse TS system. The beam of a ruby laser (max. 25 J) is led vertically through the plasma (item 1). The laser can be fired twice, dividing the energy of 25 J over two pulses of 12.5 J. The pulses are fired with a separation time of 20–800 μs. The observational chord of 300 mm length is imaged onto the 200 mm high entrance slit (item 5) of the polychromator. Spectral analysis is performed by a flat grating (item 7) in the Littrow set-up, covering a wavelength range of 530–850 nm. Collimation of input light and focusing of diffracted light is performed by an achromatic doublet (item 6). The grating is oriented such that the laser wavelength returns along its original path through the gap in the spherical mirror (item 8). This way vessel stray light is filtered out, resulting in a stray light ratio of $\leq 5\cdot 10^{-4}$ for each spatial element when the full slit height is illuminated. The spectrum is projected onto the two-part spherical mirror which serves for pupil imaging. The spectral image of 200×200 mm^2 is further projected onto the detector surface. A polarizer (item 14) in front of the TV objective

(item 9) reduces the plasma light contribution.

1 laser beam	8 two-part mirror
2 window	9 TV objective
3 doublet f = 1 m	10 image intensifier
4 field lens	11 coupling lens
5 entrance slit	12 beam splitter
6 Littrow doublet	13 ICCD camera
7 grating	14 polarizer

Figure 5.3: *Schematics of the double pulse TS diagnostic at RTP. Scattered light is col-lected in the radial direction.*

The detector system consists of a GEN. III image intensifier (item 10), a lens coupling system (items 11), a 50-50 % beamsplitter (item 12) and two Intensified Charge Cou-pled Device (ICCD) cameras. The $200 \times 200\,mm^2$ spectral image at the spherical mirror (item 8) is reduced to $\sim 8 \times 8\,mm^2$, i.e. 350×350 pixels^2. Figure 5.4 shows an image of TS light on the CCD chip: 350 spectra with 350 wavelength pixels, which are later binned by four pixels to obtain $\sim$85 wavelength channels. This binning is performed since the wavelength resolution with a 2 mm wide slit is approximately four pixels. In the center the spectra are wider than at the top and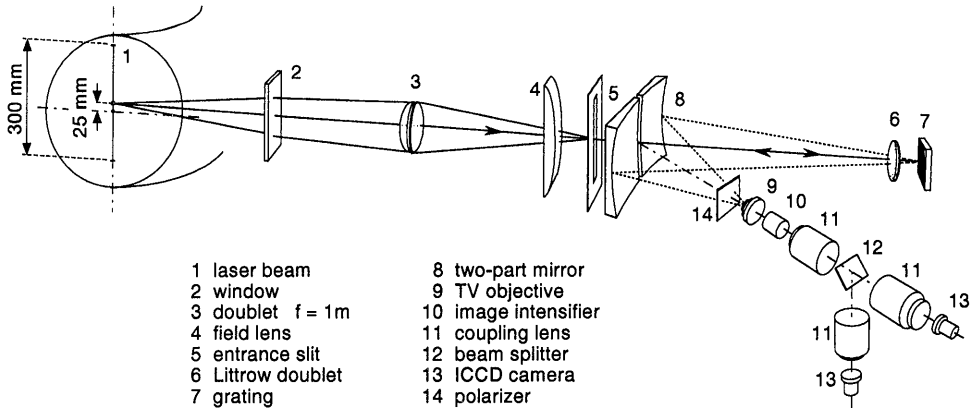 the bottom of the picture, indicating a higher T_e in the center than at the edge. The cutting window of the mirror at $\lambda_0 = 694.3$ nm is visible in the middle of the image. The figure shows the spectra corresponding to the n_e profile in Fig. 5.2.

The first image intensifier (item 10) has a fast gate of 100 ns in which all scattered light is collected (laser pulse length ≈ 40 ns FWHM). In this 100 ns also light such as the H_α-line emission, continuum radiation and vessel stray light from the laser, is collected, by which the measurement can be disturbed. Fig. 5.5 shows these other light sources and compares them to a TS spectrum. It is clear that the continuum and vessel stray light are well below the TS light level. H_α light, however, is of the same order as the TS light. For analysis, this is eliminated with software.

The procedure of double pulse measurements is as follows. The laser is fired twice with Δt between 20 and 800 μs. The fast gate of the first image intensifier (item 10) is triggered twice by laser light picked up at the laser and led to the gate circuit by a quartz fiber. To distinguish between the two laser pulses, the image intensifiers inside the ICCD cameras are used as fast electronic shutters; camera 1 records the first laser pulse and camera 2 the second. The cameras are gated open for 20μs which is adapted to the shortest separation time between two laser pulses. During these 20μs only $\kappa \approx 30$ % of the light emitted by the P20 phosphor of the first image intensifier is collected, because the phosphor has a slow decay time of ~ 3 ms to a 1 % level. This 30 % however is sufficient, since the photon

noise of the system is still mainly determined at the cathode of the first image intensifier (section 5.3).
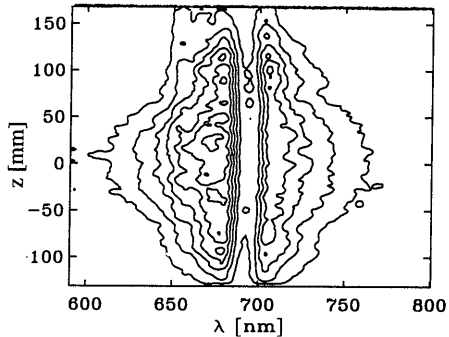
Figure 5.4: *Contour plot of CCD-image containing raw TS data. The width in λ-direction is a measure for T_e. The vertical gap at $\lambda_0 = 694.3\,nm$ is caused by the cutting window in the two part mirror in the spectrometer (Fig. 5.3). At 656.3 nm H_α deforms the measurement.*
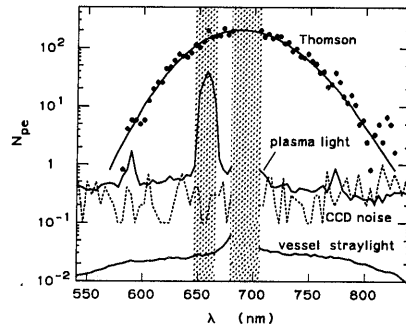
Figure 5.5: *A TS spectrum with its fit compared to disturbing light sources like H_α line and continuum emission, and vessel stray light. The continuum emission and vessel stray light levels are well below the TS spectrum. H_α light is eliminated with software.*

5.3 Error determination

Assuming a Maxwellian velocity distribution Mattioli derived an analytical expression for the spectrum of incoherent TS scattered light [14]. The expression is a Gaussian of which the blue wing is somewhat enhanced due to relativistic effects. Figure 5.6 gives examples of this theoretical curve for several T_e-values. The enhancement of the blue wing becomes larger with higher T_e. The theoretical curve is determined with two parameters: the area underneath the curve and the width of the curve. Before fitting the raw data with this curve, a series of calibrations and corrections need to be performed, which are extensively described in [4, 5, 15]. The most important are the relative and absolute calibration. The relative calibration corrects for wavelength dependent transmission, and is important for the T_e determination. The absolute calibration is needed to calculate absolute values for n_e from the integrals of the scattered spectra. Errors on the T_e and n_e determination caused by calibration errors are discussed in [5] by comparing the results of the two cameras. It is found that systematic deviations due to calibrations lie within one standard deviation of the measurements.

Another source that can disturb the measurements is collected light other than TS scattered light. Figure 5.5 shows that the level of these is negligibly low.

Remaining deviations from a correct T_e and n_e determination can be caused by:

- Detection noise, causing a statistical deviation.

- Deformation of the spectra by the instrument profile of the diagnostic, causing a systematic deviation.

The instrument profile of the diagnostic is $\sim$ 3 pixels wide and has a very long tail. Especially this tail causes a significant systematic error in the T_e and n_e determination as will be discussed in section 5.6.

In the detector branch of the diagnostic there are several stages where noise is generated. Since in the z-direction the full pixel resolution is used in the determination of T_e and n_e, also in this case the instrument function plays a role. Noise generated at a certain stage is smoothed by the instrument profile of the remaining part of the diagnostic.

An absolute estimator for the noise in the system is important to derive estimators for the statistical errors on T_e and n_e as will be shown in section 5.3.1. The error contributions at different stages in the detector branch will be discussed in section 5.3.2. The influence of the instrument function on the noise will be discussed in section 5.3.3.
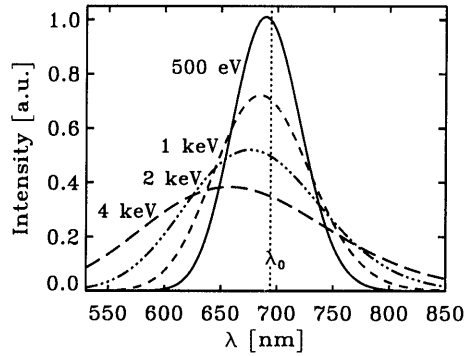
Figure 5.6: *Example of normalised relativistic TS spectra for Maxwellian velocity distributions with $T_e = 500\,eV$, $1\,keV$, $2\,keV$ and $4\,keV$. $\lambda_0 = 694.3\,nm$, i.e. the ruby laser wavelength.*

5.3.1 Fitting routine

The fitting routine applied for the fits of the calibrated data is a non-linear least square fitting routine by Levenberg and Marquardt, e.g. [16]. This fitting routine minimizes the χ^2:

$$\chi^2(j) = \sum_{i_b} \left[S_{TS}(i_b, j) - F(i_b)\right]^2 \cdot W(i_b, j), \qquad (5.1)$$

where $S_{TS}(i_b, j)$ is the calibrated TS signal, and $F(i_b, j)$ the fitting function, Fig. 5.6. The formula is expressed in CCD-pixels j in the z-direction and i_b in the λ-direction. The index b indicated binning of four pixels in the λ-direction as is done in the experiment. The weight-function $W(i_b, j)$ contains an estimator for the standard deviation of the measured spectra, $\sigma_{S_{TS}}$. The value of the reduced $\chi^2(j)$, $\chi^2_\nu(j)$, indicates the goodness of the fit:

$$\chi^2_\nu = \chi^2/\nu \qquad (5.2)$$

where ν is the number of degrees of freedom of the fit. For a good fit, $\chi^2_\nu(j)$ should be distributed around 1. The weight function $W(i_b, j)$ is defined as:

$$W(i_b, j) = \frac{5}{\sum\limits_{i_b-2}^{i_b+2} \sigma^2_{S_{TS}}(i_b, j)} \qquad (5.3)$$

$W(i_b, j)$ smooths the estimator for $\sigma_{S_{TS}}(i_b, j)$ over 5 binned wavelength channels of 4 pixels each. Using $\sigma_{S_{TS}}(i_b, j)$ the fitting routine makes an estimation of the statistical error on T_e and n_e according to:

$$\sigma_{T_e}^2(j) = \sum_{i_b} \sigma_{S_{TS}}^2(i_b, j) \left(\frac{\partial T_e(j)}{\partial S_{TS}(i_b, j)} \right)^2 \tag{5.4}$$

and

$$\sigma_{n_e}^2(j) = \sum_{i_b} \sigma_{S_{TS}}^2(i_b, j) \left(\frac{\partial n_e(j)}{\partial S_{TS}(i_b, j)} \right)^2 \tag{5.5}$$

Thus the errors on T_e and n_e are determined by a weighted quadratic sum over the errors on all data points in the spectrum. Any correlation between the $\sigma_{S_{TS}}(i_b, j)$-values needs to be accounted for in the sums (5.4) and (5.5). In section 5.3.3 will be shown that the detection branch instrument profile leads to a correlation in the $\sigma_{S_{TS}}(i_b, j)$-values. The correction for this correlation is dealt with in that section.

5.3.2 Breakdown of noise sources

The detection branch of the diagnostic contains the elements 10–13 in Fig. 5.3. There are three stages in this branch where photon statistics introduces noise on the signal:

- At the first image intensifier.

- At the image intensifier of the ICCD camera.

- At the CCD-chip of the ICCD camera.

A fourth noise source is read-out noise in the CCD camera.

At an image intensifier photons induce primary photoelectrons with a certain quantum efficiency η_Q. These primary photoelectrons are accelerated towards a Micro Channel Plate (MCP) where secondary electrons are produced in a multiplication process. The secondary electrons are again accelerated towards a phosphor screen that subsequently emits light. The photon noise induced in the image intensifier is determined by the number of primary photoelectrons and the so-called noise figure NF of the MCP, which includes noise generated in the multiplication process. An effective efficiency η_{eff} of the image intensifier is now defined as:

$$\eta_{eff} = \eta_Q / NF^2 \tag{5.6}$$

At the CCD also photoelectrons are produced. The photon noise at the CCD is determined by the number of these photoelectrons. The analog signal of the CCD is converted into CCD-counts. For this reason the conversion factor of photoelectrons into CCD-counts must be known in order to know the noise amplitude from the number of counts. For the CCD cameras in the diagnostic this conversion factor is 10 photoelectrons/count. The system has two ICCD cameras which are more or less equal. In the following discussion only one camera is discussed. A worst case scenario is taken, using the specifications of the ICCD camera with the lowest sensitivity.

The amplitude of the noise in all three cases listed above will be estimated using values for the system parameters as given in Table 1. Most of the parameters in Table 1 in principle are wavelength and position dependent. However, the variation is < 20 % for the greater part of the detection area. For reasons of convenience, they are taken as wavelength and position independent in the error analysis. The parameters are described in the table and will be further explained in the following.

Table 1: *Summary of wavelength independent system parameters.*

Symbol	Description	Quantity	Unit
E_{laser}	Laser energy at the scattering volume	10	J
$h\nu_0$	Single photon energy at 694.3 nm	2.86×10^{-19}	J
ΔL	Length of scattering volume (seen by 1 pixel)	0.82×10^{-3}	m
Ω	Solid angle of collection	2.1×10^{-3}	sr
$\sigma_{Thomson}$	classical TS cross-section	7.94×10^{-30}	m^2/sr
$\tau_{overall}$	Overall system transmission	17	%
η_1	Efficiency of intensifier 10	18	%
G_1	Photon gain of the first intensifier	2.5×10^3	
T_1	Efficiency lens coupling system	6	%
η_2	Efficiency of the ICCD intensifier	3	%
κ	Collection fraction second image intensifier	30	%
K_{CCD}	ICCD detection efficiency: counts/photon	5×10^{-2}	cnt/ph
ζ_{CCD}	CCD conversion factor: photoelectrons/count	10	pe/cnt

Number of scattered photons $S_{ph,\,scatt}$ in the vessel.

Laser light is scattered by the free electrons in the plasma. The number of photons scattered from a volume with length ΔL (covered by 1 CCD pixel) in the solid angle Ω at a density $n_e(j)$ is:

$$N_{ph,\,scatt}(j) = \frac{E_{laser}}{h\nu_0} \Delta L \, \Omega \, \sigma_{Thomson} \, n_e(j), \qquad (5.7)$$

where the index j indicates CCD pixels in the z-direction. $E_{laser}/h\nu_0$ is the total number of photons in a single laser pulse and $\sigma_{Thomson}$ the differential TS cross section. Since the full pixel resolution is used, the length of the scattering volume is 0.82 mm. The amount of photons scattered as a function of wavelength is given by:

$$S_{ph,\,scatt}(i,j) = N_{ph,\,scatt}(j) \cdot F(i,j)\,di, \qquad (5.8)$$

where $F(i,j)$ is the relativistic expression by Mattioli for a TS spectrum, Fig. 5.6. Index i indicates the unbinned pixels in the wavelength direction. Binning four pixels in the wavelength direction is introduced at the end of the next section. The integral $\int F(i)\,di \geq 1$ due to the relativistic effects (depending on T_e). For example, for $T_e = 1$ keV, $\int F(i)\,di = 1.06$. However the deviation from unity is small and for this reason the approximation $\int S_{ph,\,scatt}(i,j)\,di \approx N_{ph,\,scatt}(j)$ will be used in the rest of the paper.

Number of photoelectrons $S_{pe,1}$ at the first intensifier.

The scattered photons $S_{ph,\ scatt}(i,j)$ are collected with the viewing optics (Fig. 5.3, items 2–4), and dispersed by the spectrometer part (items 5–9). The number of photons in front of the first image intensifier, indicated with $ph, 1$, is:

$$S_{ph,1}(i,j) = S_{ph,\ scatt}(i,j)\ \tau_{overall}, \qquad (5.9)$$

where $\tau_{overall}$ refers to the transmission of the branch (items 2–9) including the polarizer (14). The index 1 indicates the first image intensifier. The photon noise on the output signal of this intensifier is determined by the effective number of photoelectrons $S_{pe,1}(i,j)$ obtained with its effective efficiency η_1, see equation (5.6):

$$S_{pe,1}(i,j) = S_{ph,1}(i,j)\ \eta_1. \qquad (5.10)$$

The standard deviation of the photon noise is now given by $\sigma_{S_{pe,1}}(i,j) = \sqrt{S_{pe,1}(i,j)}$.

Number of photoelectrons $S_{pe,2}$ at the second intensifier.

The second intensifier, at the ICCD, collects $S_{ph,2}(i,j)$ photons emitted by the phosphor of the first intensifier:

$$S_{ph,2}(i,j) = S_{ph,1}(i,j)\ G_1\ T_1, \qquad (5.11)$$

with G_1 the photon gain of the first image intensifier, and T_1 the coupling efficiency of the lens system (items 11 and 12). The intensifier of the ICCD has an effective efficiency η_2. Due to the short gate of the second intensifier compared to the slow phosphor decay of first intensifier only a part κ of the $S_{ph,2}(i,j)$ photons are transformed into photoelectrons. The effective number of photoelectrons is now given by:

$$S_{pe,2}(i,j) = S_{ph,2}(i,j)\ \kappa\ \eta_2 \qquad (5.12)$$

The photon noise here is determined by $\sigma_{S_{pe,2}}(i,j) = \sqrt{S_{pe,2}(i,j)}$.

Number of photoelectrons $S_{pe,CCD}$ at the CCD.

Now, the transformation is made from photons in front of the ICCD cathode to photoelectrons on the CCD surface. For this transformation K_{CCD} and ζ_{CCD} are needed. K_{CCD} is the conversion factor from photons in front of the ICCD to CCD-counts and ζ_{CCD} is the CCD conversion factor in counts/photoelectron (at the CCD). K_{CCD} is given by:

$$K_{CCD} = \frac{G_2\ T_2\ \eta_{CCD}}{\zeta_{CCD}} \qquad (5.13)$$

It contains the photon gain G_2 of the second intensifier, the coupling efficiency T_2 between intensifier output and CCD, and the CCD quantum efficiency η_{CCD}. All three parameters are not well specified by the ICCD manufacturer. For this reason K_{CCD} is determined using an absolute calibration of the CCD sensitivity using Rayleigh scattering on H_2 at room temperature [5]. Using K_{CCD} and ζ_{CCD} the number of photoelectrons at the CCD surface is:

$$S_{pe,CCD}(i,j) = S_{ph,2}(i,j)\ \kappa\ K_{CCD}\ \zeta_{CCD} \qquad (5.14)$$

The amplitude of the photon noise here is given by $\sigma_{S_{pe,CCD}}(i,j) = \sqrt{S_{pe,CCD}(i,j)}$. Finally the TS signal on the CCD camera in CCD counts is given by S_{TS}:

$$S_{TS}(i,j) = S_{pe,CCD}(i,j)/\zeta_{CCD} \qquad (5.15)$$

A fourth additional noise source is the read-out noise of the CCD and has an amplitude of $\sigma_{CCD-noise} = 2$ counts.

Summary of noise sources and total noise $\sigma_{S_{TS}}$ on TS spectrum.

All noise contributions of the diagnostic are listed in Table 2. Now the estimator for the error on the final TS spectrum is $\sigma_{S_{TS}}(i,j)$. The relative error $\varepsilon_{S_x} = \sigma_{S_x}/S_x$ is introduced, with x=pe,1, pe,2, pe,CCD or TS. A good estimator for $\varepsilon_{S_{TS}}(i,j)$, is the quadratic sum of the separate contributions of relative errors:

$$\varepsilon_{S_{TS}}^2(i,j) = \frac{\sigma_{S_{TS}}^2}{S_{TS}^2}(i,j) = \left(\frac{\varepsilon_{S_{pe,1}}^2}{\Gamma_{pe,1}}(i,j) + \frac{\varepsilon_{S_{pe,2}}^2}{\Gamma_{pe,2}}(i,j) + \varepsilon_{S_{pe,CCD}}^2(i,j)\right) + \frac{\sigma_{CCD-noise}^2}{S_{TS}^2(i,j)} \qquad (5.16)$$

Two unknown parameters remain: $\Gamma_{pe,1}$ and $\Gamma_{pe,2}$. These correct for the fact that the noise produced at the first and second image intensifier is smoothed by the instrument profiles of the remaining detector branch. In the next section $\Gamma_{pe,1}$ and $\Gamma_{pe,2}$ will be determined. First, expression (5.16) will be written in terms of system parameters using equations (5.9)–(5.15), the noise amplitudes listed in Table 2, and the definition for ε_x. Equation (5.16) can now be written as:

$$\sigma_{S_{TS}}^2(i,j) = S_{TS}(i,j) \cdot \left(\frac{G_1 T_1 \kappa K_{CCD}/\eta_1}{\Gamma_{pe,1}} + \frac{K_{CCD}/\eta_2}{\Gamma_{pe,2}} + \frac{1}{\zeta_{CCD}}\right)$$
$$+ \quad \sigma_{CCD-noise}^2 \qquad (5.17)$$

Table 2: *The noise contributions of the detector branch.*

Description	Name	Amplitude
Poisson noise at the first image intensifier, item 10	$\sigma_{S_{pe,1}}(i,j)$	$\sqrt{S_{pe,1}(i,j)}$
Poisson noise at the intensifier of the ICCD, item 13	$\sigma_{S_{pe,2}}(i,j)$	$\sqrt{S_{pe,2}(i,j)}$
Poisson noise at the CCD-chip	$\sigma_{S_{pe,CCD}}(i,j)$	$\sqrt{S_{pe,CCD}(i,j)}$
Gaussian CCD read-out noise	$\sigma_{CCD-noise}$	2 counts

5.3.3 Influence of instrument profile on the statistical error

An instrument function deforms the spectra, but also smoothes noise. Figure 5.7 shows the logarithmic plot of the one dimensional (1-D) instrument function of the full diagnostic, items 1–13. This profile is obtained from Rayleigh scattering on H_2 and is averaged over 100 spatial pixels. The averaging makes the long tail of the profile visible. The central peak has ~ 3.5 pixels FWHM and determines the spectral resolution. The long tail appears to play an important role in the systematic deviations of the measurements. The effect of this long tail will be discussed in section 5.6.

To calculate the role of the instrument profile on the smoothing of noise, the instrument

profiles at different stages in the diagnostic need to be measured. In this section the smoothing factors $\Gamma_{pe,1}$ and $\Gamma_{pe,2}$ due to the smoothing effect of the appropriate instrument profiles will be calculated. Furthermore the estimator for $\sigma_{S_{TS}}$ will be given, and a first estimation of the error on n_e will be calculated.
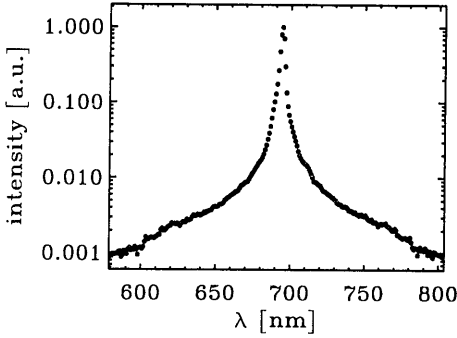

Figure 5.7: *One dimensional instrument function of the full diagnostic, i.e. items 1–13, Fig. 5.3, obtained from a line source applying Rayleigh scattering. The long tail is caused by the halo of the phosphor of the image intensifiers, rather than stray light (straylight ratio = $5 \cdot 10^{-4}$). The right-hand side of the tail is replaced by the left-hand side, because the cutting window in the two part mirror disturbs the profile. The steps at 600 and 785 nm are caused by the edge of the two-part mirror.*
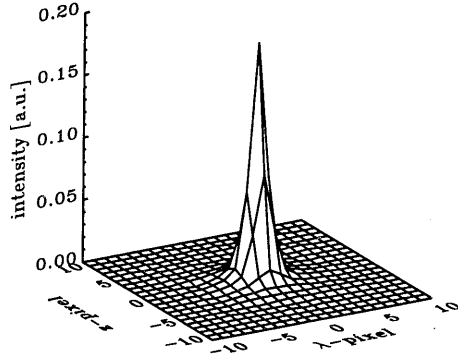
Figure 5.8: *Normalised instrument profile $I(k,l)$ of the detector system 10–13, with k (the λ–pixels) and l (the z–pixels) running from -10 to 10. The profile was measured by imaging a 250 μm pinhole, using f/22 optics, to a 22 μm image on the intensifier's surface. The 22 μm image is small compared to the image intensifier resolution of ∼ 60 μm, in order to act as a point-source.*

Error on each separate data point due to noise at the first intensifier.

Fig. 5.8 shows the two dimensional (2-D) instrument profile, $I(k,l)$, of the branch items 10–13, Fig 5.3. Noise produced at the first image intensifier is smoothed by this part of the instrument profile. In principle this profile also extends to the edge of the CCD chip, but the long tail is not resolved in the measurement of this 2-D instrument profile. However, for the smoothing of noise only the central part of the profile plays an important role. Therefore, only a smaller part of the CCD is used and a range of -10 to 10 pixels is taken leading to a 21×21 pixels large area. The signal $S_{pe,1}(i,j)$ at the first intensifier, equation (5.10), will be convolved with the above mentioned instrument profile $I(k,l)$, leading to $C_{pe,1}(i,j)$:

$$C_{pe,1}(i,j) = \sum_k \sum_l S_{pe,1}(i-k, j-l) \cdot I(k,l), \tag{5.18}$$

with k and l running from -10 to 10, the used instrument profile area. The noise on $S_{pe,1}(i,j)$ is smoothed by this instrument profile according to:

$$\sigma^2_{C_{pe,1}}(i,j) = \sum_k \sum_l \sigma^2_{S_{pe,1}}(i-k, j-l) \cdot I^2(k,l) \tag{5.19}$$

The amplitude of the signal $S_{pe,1}(i,j)$ does not vary much in the range of (k,l). For this reason the noise on $C_{pe,1}(i,j)$ compared to the noise on $S_{pe,1}(i,j)$ is approximately:

$$\sigma^2_{C_{pe,1}}(i,j) = \sigma^2_{S_{pe,1}}(i,j) \cdot \sum_k \sum_l I^2(k,l) = \sigma^2_{S_{pe,1}}(i,j)/\Gamma^*_{pe,1} \qquad (5.20)$$

The reduction factor $\Gamma^*_{pe,1}$ for noise on $C_{pe,1}(i,j)$ because of the smoothing by the instrument function is thus:

$$\Gamma^*_{pe,1} = \frac{1}{\sum_k \sum_l I^2(k,l)} \qquad (5.21)$$

Calculation of smoothing factor $\Gamma_{pe,1}$.

However, to derive T_e and n_e from the TS spectra, an array of 350 unbinned spectral points is used, to which a theoretical curve is fitted (Fig 5.6). Equations (5.4) and (5.5) determine the error on T_e and n_e. Correlations in values of $\sigma_{S_{TS}}$ in the wavelength direction cancel out in the integrals (5.4) and (5.5). For this reason the smoothing factor $\Gamma_{pe,1}$ as is applied in equation (5.17) will be smaller than $\Gamma^*_{pe,1}$. This means that the error on the integral of a spectrum in the wavelength direction will be larger than the quadratic sum of $\sigma_{C_{pe,1}}$ in i, equation (5.20). The correct value for $\Gamma_{pe,1}$ is corrected for the correlation of noise in the wavelength direction. It is given by:

$$\Gamma_{pe,1} = \frac{1}{\sum_l \sum_k \sum_m I(k,l)I(m,l)} \qquad (5.22)$$

with m also running from -10 to 10. From the values of $I(k,l)$ in Fig. 5.8, $\Gamma_{pe,1}$ can be calculated: $\Gamma_{pe,1} = 4.4$, [17].

Determination of smoothing factor $\Gamma_{pe,2}$

The only remaining unknown parameter in equation (5.17) is $\Gamma_{pe,2}$. It can be calculated from the instrument profile of the ICCD camera, called $J(k,l)$. Unfortunately, this ICCD instrument profile has not been measured. However, $J(k,l)$ can be estimated from $I(k,l)$. $I(k,l)$ is the instrument profile of the branch items 10–13, Fig 5.3. Of this branch the first intensifier and the ICCD intensifier have the worst resolution, and therefore $I(k,l)$ is mainly built up out of the instrument profiles of these intensifiers. It is assumed that the instrument profiles of these intensifiers are equal. Then $I(k,l)$ is built up out of two equal instrument profiles $J(k,l)$. $J(k,l)$ has a width σ_J, according to:

$$\sigma^2_J = \frac{\sigma^2_I}{2} \qquad (5.23)$$

where σ_I is the width of $I(k,l)$. The narrower profile $J(k,l)$ can now be calculated from $I(k,l)$. The smoothing factor $\Gamma_{pe,2}$ can now be determined from the values of $J(k,l)$. Here, the correlation of noise in the wavelength direction is also taken into account:

$$\Gamma_{pe,2} = \frac{1}{\sum_l \sum_k \sum_m J(k,l)J(m,l)} \qquad (5.24)$$

This way $\Gamma_{pe,2} = 3.6$ is found.

Estimator for $\sigma_{S_{TS}}$ on the TS spectra.

Now $\Gamma_{pe,1}$ and $\Gamma_{pe,2}$ can be used to complete equation (5.17). Like in the experiment, binning of four pixels in the wavelength direction is performed, (section 5.2), thus making the transformation $i \longrightarrow i_b$. Using the values for $\Gamma_{pe,1}$ and $\Gamma_{pe,2}$ and the values for the system parameters in Table 1, the estimator for $\sigma_{S_{TS}}(i_b, j)$ becomes:

$$
\begin{aligned}
\sigma_{S_{TS}}^2(i_b, j) &= S_{TS}(i_b, j) \cdot (2.9 + 0.5 + 0.1) \ + \ 4 \cdot \sigma_{CCD-noise}^2 \\
&= 3.5 \cdot S_{TS}(i_b, j) + \ 4 \cdot \sigma_{CCD-noise}^2
\end{aligned}
\tag{5.25}
$$

The main contribution to the noise on the final data is by the photon statistics generated at the first image intensifier. The system has been designed to have the major detection noise here; the contribution to $\sigma_{S_{TS}}$ is $\sqrt{2.9/3.5} \approx 90\,\%$. This way splitting up the signal with a beamsplitter for the double detection system has hardly any effect on the noise. Equation 5.25 gives the estimator for $\sigma_{S_{TS}}(i_b, j)$ as it will be used in the fitting routine in the weighting factor equation (5.3). It is corrected for the correlation of the $\sigma_{S_{TS}}(i_b, j)$-values in the wavelength direction.

First estimation for the error on n_e.

An first estimation of the error in the n_e determination can be made. The density n_e is proportional to the integrated signal $N_{TS}(j) = \int S_{TS}(i_b, j) di_b$. Since correlation in the noise in the wavelength direction has been accounted for already in equation (5.25) the error on $N_{TS}(j)$ is given by:

$$
\sigma_{N_{TS}}^2(j) = 3.5 \cdot N_{counts}(j) + \ 350 \cdot \sigma_{CCD-noise}^2
\tag{5.26}
$$

For a typical n_e of $5 \times 10^{19} \mathrm{m}^{-3}$ the number of counts detected according to equations (5.7)–(5.15) is $N_{counts} \approx 10^4$ counts. Equation (5.26) then gives: $\sigma_{N_{TS}} \approx 200$ counts; a relative error of $\approx 2\,\%$. Which is also a first estimate for the error on n_e.

5.4   Errors on n_e and T_e; fits on simulations of TS spectra.

In this section the errors on T_e and n_e are determined by simulating spectra with the Mattioli scattering formula for a relativistic electron population. Noise is added at different stages in the instrument to conform to the experiment. The amplitudes of the noise are taken as given in Table 2, and the noise is created using a noise generator. The smoothing effect on the noise by the instrument profile is implemented at the appropriate stages. The simulated spectra are fitted with the non-linear least square fitting routine as described in section 5.3.1. Equation (5.25) is used as the estimator for the error in the weight function (5.3). For $n_e = 5 \times 10^{19} \mathrm{m}^{-3}$ and 10 values of T_e in the range of 50 eV–6 keV, 500 spectra have been simulated. Convolution with the instrument profile $I(k, l)$ smoothes the noise. The simulated spectra are prepared in the following sequence:

- Add Poisson noise generated at the first intensifier.

- Convolve the 500 TS spectra with $I(k, l)$, Fig. 5.8.

- Add Poisson noise generated at the cathode of the ICCD. Here no convolution is allowed anymore since the signal at the first intensifier has been convolved with $I(k, l)$ already, i.e. the instrument profile of the total detection branch (Fig. 5.3, items 10–13). Reduction of noise at the second intensifier is performed by decreasing the noise amplitude here with $\sqrt{\Gamma_{pe,2}}$.

- Add Poisson noise generated at the CCD-chip.

- Add CCD read-out noise.

- Bin the spectra with 4 pixels in the wavelength direction.

Treating noise in this way, instead of just considering the quadratic sum of contributions as in section 5.3, is more realistic. Namely, the number of photons/photoelectrons generated at one stage determines the number of photons/photoelectrons as input for the next stage. Thus, a lower number of photons/photoelectrons generated at stage 1 will lead to more noise generated at stage 2. While in the quadratic sum of errors in section 5.3, only average numbers are taken, and the noise amplitudes at the separate stages are taken as independent. The error estimations in section 5.3 is a good estimate for the noise amplitude on the final signal as used in the weight factor, equation (5.3), since noise generated at the first stage is dominant.

Fig. 5.9 shows an example of a simulated spectrum with $T_e = 1 \, \text{keV}$, and its fit. The cutting window and the H_α spectral line are cut out of the spectrum, just like in the real experiment. The weight function applied for this fit is also plotted in Fig. 5.9.
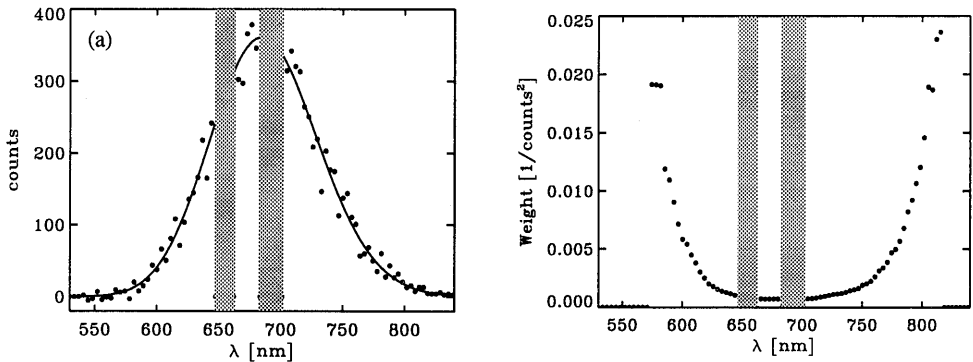
Figure 5.9: *Fit of a simulated spectrum (a) and its weight factors (b). Starting values are $T_e = 1 \, keV$, $n_e = 5 \times 10^{19} m^{-3}$, and $E_{laser} = 10 \, J$. The cutting window and the region around H_α are left out.*

The 500 fits to the simulated data give 500 T_e and n_e-values, with average values $< T_e >$ and $< n_e >$. Convolution with $I(k, l)$ hardly affects the shape of the spectra, resulting in small systematic deviation in $< T_e >$ and $< n_e >$. The deviations from the starting values T_e and n_e lie within 2 % for both parameters.

The statistical error on the T_e and n_e values from the fits are derived in two different ways. In the first, the fitting routine gives an estimator for the error on T_e and n_e from its covariance matrix, and in the second method the spread in the 500 T_e and n_e-values

from the fits of the simulated spectra are calculated. The error estimators for T_e and n_e derived form the covariance matrix in the fit are labeled $\sigma_{T_e,fits}$ and $\sigma_{n_e,fits}$. And the spread in the 500 fits are indicated with $\sigma_{T_e,stat}$ and $\sigma_{n_e,stat}$. In the experiment only $\sigma_{T_e,fits}$ and $\sigma_{n_e,fits}$ can be calculated. As a test of the fitting routine both methods are compared using the simulations of the TS spectra. Figure 5.10 shows the comparison.
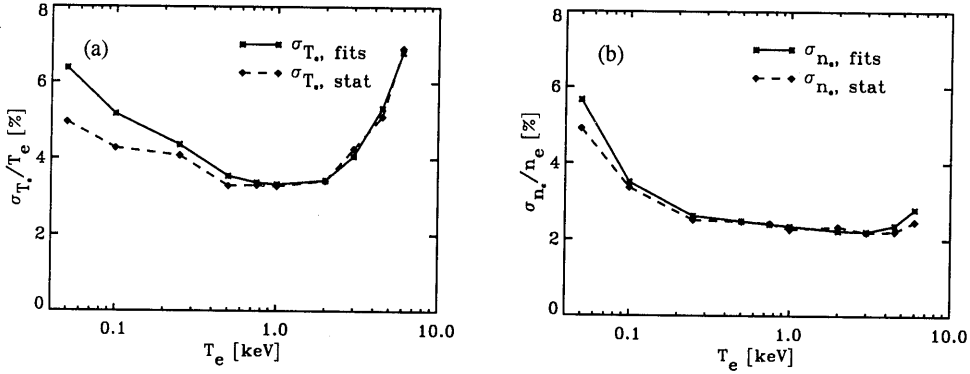

Figure 5.10: *Relative errors on (a) T_e and (b) n_e. The full line shows the estimator for the errors $\sigma_{T_e,fits}$, and $\sigma_{n_e,fits}$, as determined from the covariance matrix of the fitting routine. The dashed line shows the spread, $\sigma_{T_e,stat}$ and $\sigma_{n_e,stat}$, in the 500 T_e and n_e values. In the simulations $n_e = 5 \times 10^{19} m^{-3}$ and $E_{laser} = 10 J$ are taken.*

As the figure shows the error calculated by the fitting routine agrees very well to the standard deviation in the 500 simulated measurements. The fitting routine over-estimates the error for the lower T_e's, but no more then 25 % for $T_e = 50$ eV. In the region 500 eV– 2 keV σ_{T_e} and σ_{n_e} are nearly independent of T_e. At low T_e values relatively much light is cut out of the spectra by the central cutting window, causing a loss of signal and an increase of σ_{T_e} and σ_{n_e}. Above $T_e = 2$ keV the error also rises because for these high temperatures the spectra become broader than the spectral range (530–850 nm) of the spectrometer. The latter effect is less dramatic for n_e than for T_e. The n_e determination is less sensitive to the slope of the wings of the spectra.

At the end of section 5.3.3 an estimation for the error on n_e was given. There the estimated relative error was given as $\sigma_{n_e}/n_e \approx 2\%$. Figure 5.10 shows that $\sigma_{n_e}/n_e \approx 2.5\%$ for a wide T_e-range. The higher value is caused by the loss of data-points in the H_α- and cutting-window, which has not been taken into account in the previous section.

5.5   Comparison with the experiments

In this section the error bars on T_e and n_e obtained from experimental data are compared to the errors found in the simulations in the previous section. Calibrated TS spectra are fitted with the relativistic formula for a TS spectrum, Fig. 5.6, using the fitting routine described in section 5.3. The comparison is performed for a medium n_e Ohmic discharge, Fig. 5.11, and for a high T_e, low n_e ECH plasma, Fig. 5.14. The errors obtained from the fitting routine in the simulations, Fig. 5.10, are scaled to the densities, and laser energies in the experiments.

For the Ohmic discharge, Fig. 5.11, an example of a fit to a spectrum is given in Fig. 5.12. The reduced χ_ν^2 value of this fit is 0.86. The figure also shows the histogram of χ_ν^2 values for all fits. The expected distribution is overplotted to the histogram. The number of degrees of freedom ν for the fits vary from 10 for the lower to 45 for the higher T_e-values. Therefore, for each point the theoretical χ_ν^2-distribution function is calculated and all curves are averaged, thus obtaining the expected χ_ν^2-distribution. The average value over all spatial points of the χ_ν^2 is just above one: $< \chi_\nu^2 > = 1.11$, indicating a small underestimation of $\sim 5\%$ of the errors. Figure 5.13 show the comparison between the errors obtained from the experiments and from the simulations. The agreement between simulations and experiment is very good.

Figure 5.15 shows an example of a fit to a central spectrum of the ECH discharge in Fig. 5.14. Here the reduced χ_ν^2 is 0.90. The spectrum is much noisier than the spectrum of the Ohmic discharge above, still the relative error determined from this spectrum is only 7% for T_e and 4% for n_e, respectively. The figure also shows the histogram of χ_ν^2 for all fits with the expected χ_ν^2-distribution overplotted. The average value of all χ_ν^2 values is $< \chi_\nu^2 > = 1.02$. Figure 5.16 also shows that for higher T_e the errors on T_e and n_e obtained form the experiment and simulations agree very well.

In conclusion, the error determination from the experiments using the fitting routine is good. The values agree very well with the simulations, and the histograms of reduced χ_ν^2-values agree well with the expected χ_ν^2–distribution functions. The averaged χ_ν^2-value averaged over all spatial points is close to unity for both examples.

As a historical note should be mentioned that TS profiles measured with the double pulse diagnostic, presented in papers between July, 1996 and January, 1998, have too small error bars. There the error on T_e and n_e should be multiplied by a factor of 1.5. This remark excludes reference [4], which deals with older single pulse TS data. The error bars in the profiles of this single pulse diagnostic have been calculated correctly.
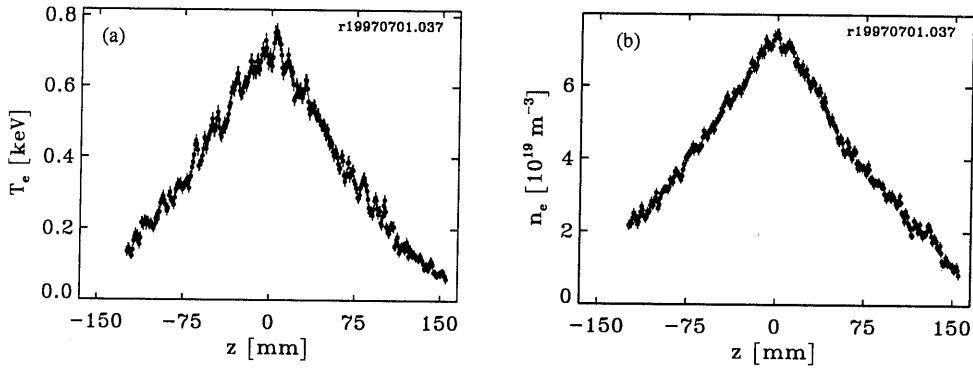
Figure 5.11: *(a) T_e and (b) n_e profile of an Ohmic discharge. Parameters: I_p=80 kA, q_a=5.2.*
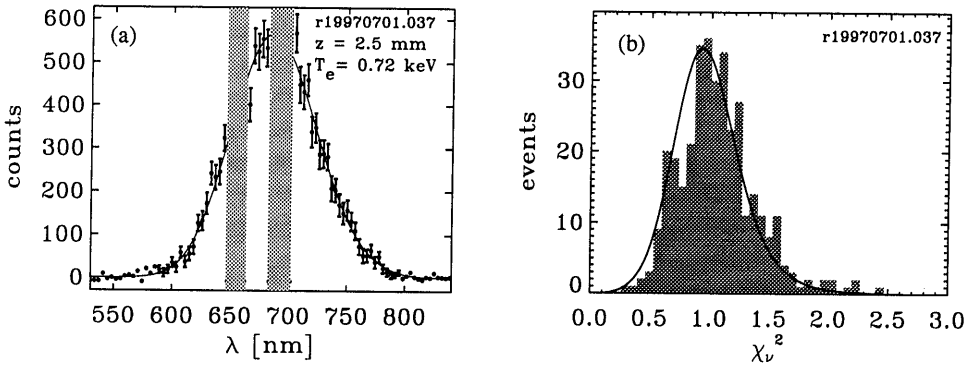
Figure 5.12: *(a) Fit through calibrated TS spectrum: T_e=720 eV, n_e=7.1×10^{19} m^{-3}, and χ^2_ν=0.86. The spectrum belongs to the point at z=2.5 mm in Fig. 5.11. (b) Histogram of the χ^2_ν values for the Ohmic discharge. The full line is the expected distribution for χ^2_ν, see text.*

Figure 5.13: *The relative error on (a) T_e and (b) n_e as a function of T_e for the data in Fig. 5.11. The errors estimated by the fitting routine for the experiment are compared to the errors estimated by the simulations. The agreement is very good.*
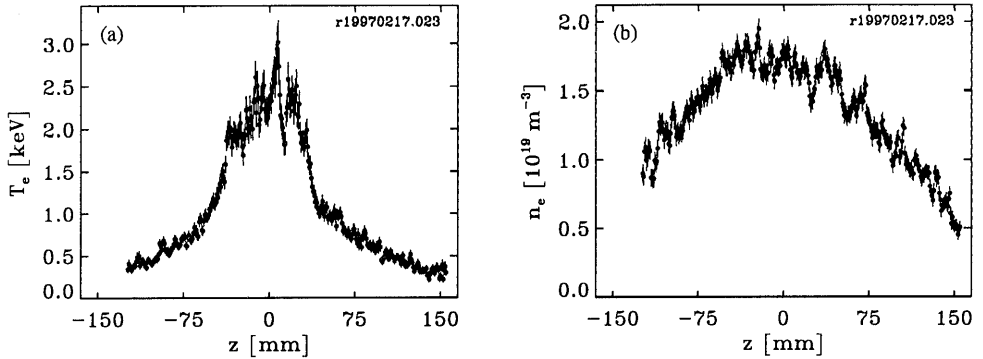
Figure 5.14: *(a) T_e and (b) n_e profile of a low n_e ECH plasma. I_p=60 kA, and q_a=6.4.*
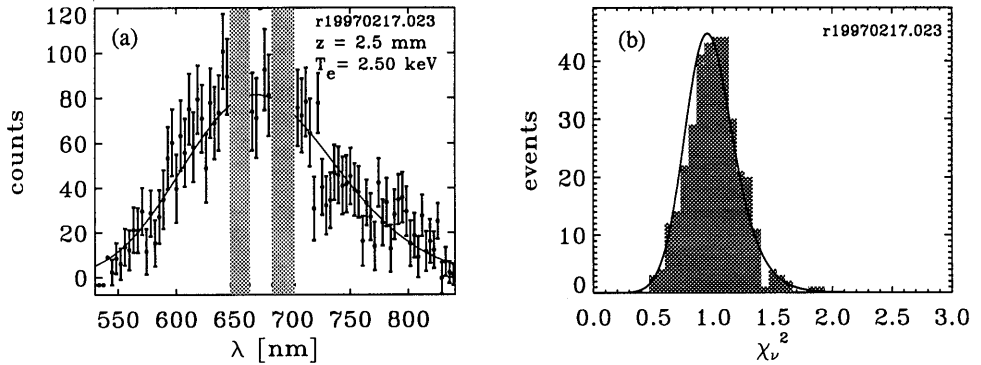
Figure 5.15: *(a) Fit through calibrated TS spectrum: T_e=2.5 keV, n_e=1.7×10^{19} m^{-3}, and χ^2_ν=0.90. The spectrum belongs to the point at z=2.5 mm in Fig. 5.14. (b) Histogram of the χ^2_ν values for the ECH plasma. The full line is the expected distribution for χ^2_ν, see text.*
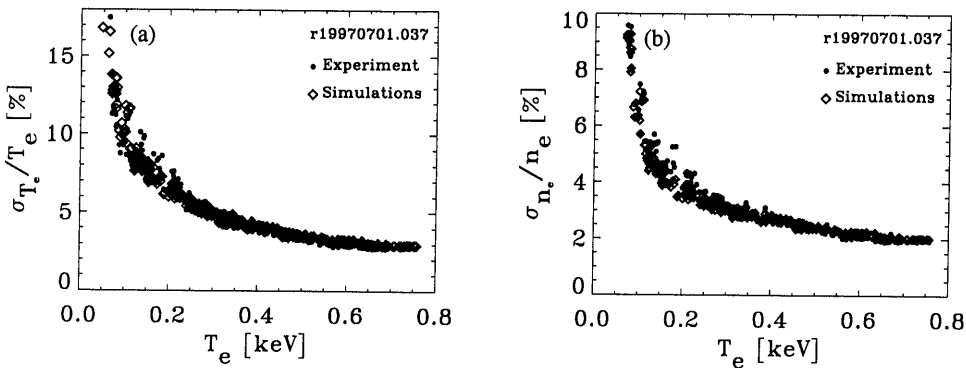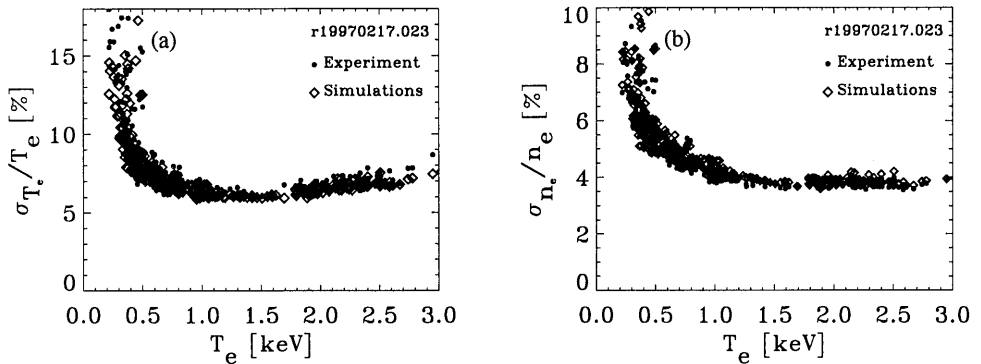

Figure 5.16: *The relative error on (a) T_e and (b) n_e as a function of T_e for the data in Fig. 5.14. The errors estimated by the fitting routine for the experiment are compared to the errors estimated by the simulations. The agreement is very good.*

5.6 Bias on T_e and n_e determination due to instrument profile.

The instrument profile of the full diagnostic has a very long tail (Fig. 5.7). This long tail puts a pedestal on the spectra when convolved with the instrument profile. The pedestal causes an over-estimation of T_e and an under-estimation of n_e by the fitting routine. In this section the quantitative effect of the convolution with the full instrument profile on the bias in the T_e and n_e determination is calculated.

Every point in the image on the CCD camera is represented by a different 2-D instrument profile. However the amplitude of the tail of such an instrument profile is $\sim 10^{-5}$ times the maximum. The dynamic range of the 16 bits CCD camera is not large enough to resolve this. The tail becomes visible when a line source is applied, e.g. Rayleigh scattering on $H_2$ gas illuminating the full entrance slit, see Fig. 5.7. Every point source along the 350 points high vertical image of the laser beam gives a contribution to the tail, yielding a ~ 350 times higher amplitude of the tail. The ratio in amplitude between the tail and the maximum of the profile then becomes $\sim 5 \cdot 10^{-3}$, as can be seen in Fig. 5.7. The profile in the figure has been averaged over 100 position pixels in the vertical direction to get better statistics.

Convolution with the 1-D profile gives a good approximation for the 2-D convolution if:

- The 2-D instrument profile is invariant under translation of z and λ.

- And the T_e and n_e profiles are flat.

Under these assumptions transforming the 2-D convolution into the 1-D convolution is as follows:

$$
\begin{aligned}
C(i,j) &= \sum_k \sum_l P(i-k, j-l) \cdot Q(k,l) \\
&= \sum_k P(i-k, j) \sum_l Q(k,l) \\
C(i) &= \sum_k P(i-k) \cdot R(k) \quad\quad\quad (5.27)
\end{aligned}
$$

With i and j the $\lambda-$ and $z-$pixel indices, and $P(i,j)$ the scattered spectra, $Q(k,l)$ the 2-D instrument profiles, and $C(i,j)$ the convolved signal. $R(k)$ is the 1-D instrument profile. In $C(i)$ the index j is left out because there no dependence in the $z-$direction is assumed; the T_e and n_e profiles are assumed to be flat.

In this section the effect of convolving the spectra with the 1-D instrument profile of Fig. 5.7 is shown. For ten T_e-values, theoretical TS spectra are convolved with the 1-D instrument profile and the appropriate amount of noise is added. First, these simulated spectra will be fitted without applying any correction. It will be found that in this case, the systematic deviations are rather large for low values of T_e. Next, a correction method is introduced. The fit function will be convolved with the 1-D instrument profile as well, which gives much better results. Finally a more simple correction method is introduced which is used for bulk data analysis.

5.6.1 Uncorrected fits to convolved spectra.

Fig. 5.17 gives an example of a convolved spectrum with input values T_e=250 eV and n_e=5·10^{19}m^{-3}, and its fit. In the figure, no noise has been added to the spectra to make the pedestal in the spectrum caused by the convolution more clear. The fit gives an over-estimation of T_e of 28 % and an under-estimation of n_e of 15 %, giving T_e=320 eV and n_e=4.25×10^{19}m^{-3}. Fig. 5.18 compares the T_e and n_e values obtained from the fit with the ten input values. As can be expected, the effect is larger for lower values of T_e, and becomes less important for higher T_e. For T_e=50 eV the deviation is +40 % for T_e and -40 % for n_e, while for T_e=3 keV the deviation for T_e and n_e are only +7 % and -3.5 % respectively.
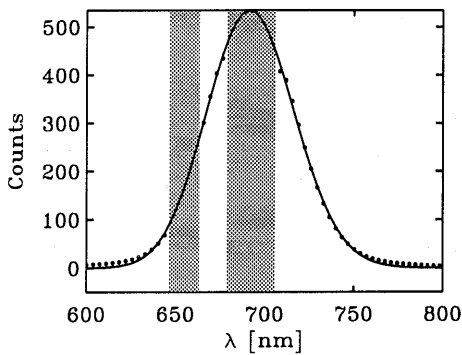

Figure 5.17: *TS spectrum convolved with the 1-D instrument profile. The spectrum is fitted with an uncorrected fitting function. The input values are T_e= 250 eV and n_e= 5·10^{19}m^{-3}, while the fit yields T_e=320 eV and n_e=4.25×10^{19}m^{-3}.*
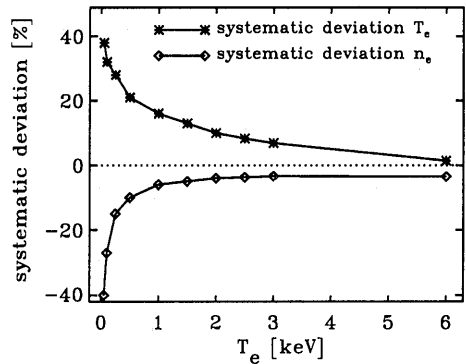
Figure 5.18: *Bias on T_e and n_e as a function of T_e caused by convolution of the spectra with the 1-D instrument profile.*

5.6.2 Convolution of the fit function.

The fits to the convolved spectra give large systematic deviations in the estimations of T_e and n_e. Deconvolution of the TS spectra would be a good correction method. However, the problem with deconvolution is that it amplifies noise on the spectra. A better correction method is convolving the fitting function with the same 1-D instrument profile. In the fitting routine this convolution is repeated for each iteration step with new fitting parameters. Figure 5.19 shows an example of a fit with this new fitting function. The fitting function for the same T_e and n_e but without convolution is overplotted. Figure 5.20 shows the results for the deviations in the T_e and n_e determination. The deviations become very small.

As explained in the introduction of this section, the instrument profile is different for every position on the CCD. This means that in the experiment the correction for the deformation of the TS spectra can not be expected to be as good as in Fig. 5.20. Furthermore, this method is rather time-consuming, since the convolution of the fitting function is performed in every iteration step. For bulk data analysis another correction method is applied, as will be explained in the next section.

Figure 5.19: *Example of a fit to a spectrum with T_e=250 eV and n_e=5·$10^{19}m^{-3}$ which has been convolved with the 1-D instrument profile. In this case the fitting function (full line) is convolve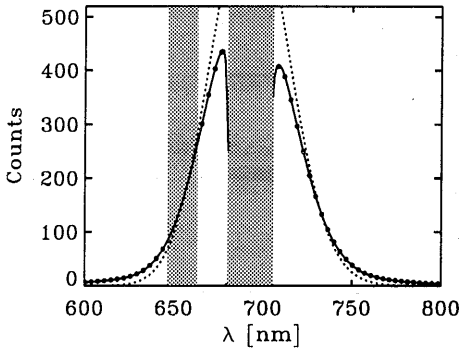d as well, resulting in a good fit of the simulated spectrum. The fitting function with same parameters but without convolution is over-plotted with a dotted line.*
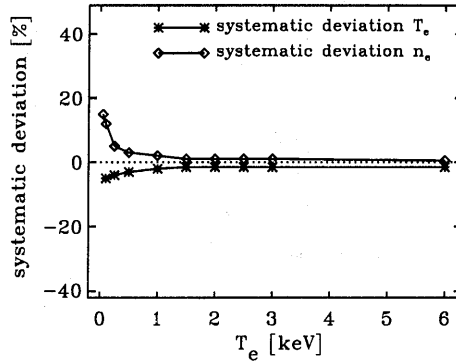
Figure 5.20: *Bias in the T_e and n_e determination when the convolved fitting function is used, e.g. Fig. 5.19. The deviation from the input values T_e=250 eV and n_e=5·$10^{19}m^{-3}$ become very small.*

5.6.3 Coarse correction for the long tail of the instrument profile.

Since the long tail of the instrument profile in first approximation puts a pedestal to the spectra, a coarse correction is subtracting a constant background from the spectra. In the experiments this is performed by subtracting a fraction 4·10^{-6} of the total signal on the CCD of the spectra. This number has been determined empirically. It appeared that in this way on average the tail in the spectra is brought back to zero. The total CCD image contains 350 spectra. In the single spectrum fit of the simulations the pedestal in the spectrum is corrected for by subtracting 350×4·10^{-6} = 14·10^{-4} of the total spectrum. Fig. 5.21 shows the convolved spectrum of Fig. 5.17 corrected for the pedestal. The fit yields T_e=308 eV, i.e. still an over-estimation of 23 %. The under-estimation of n_e becomes a little larger due to the subtraction of the constant background. the bias on n_e becomes -17.5 %, giving n_e=4.12·$10^{19}m^{-3}$. For higher T_e-values the deviation becomes less: For T_e = 3 keV, the over-estimation of T_e is 4 %, and the under-estimation of n_e is 7 %. Figure 5.22 shows the systematic deviations on T_e and n_e.
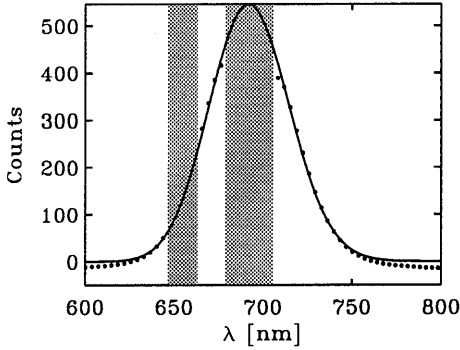
Figure 5.21:   *The same spectrum as in Fig. 5.17 with $T_e=250\,eV$ and $n_e = 5\cdot10^{19}m^{-3}$ as input values. In this case a pedestal is subtracted from the spectrum. The T_e determination is somewhat better now: $T_e=308\,eV$, and the n_e under-estimation is a little larger: $n_e=4.12\cdot10^{19}m^{-3}$.*
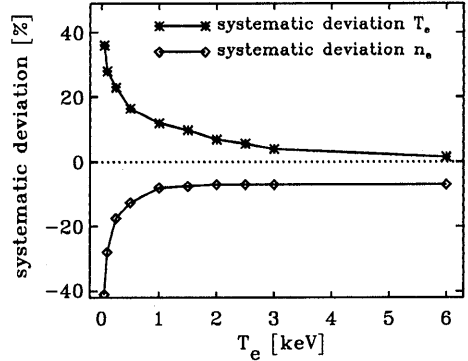
Figure 5.22:   *Bias in the T_e and n_e determination as a function of T_e when a pedestal is subtracted from the spectra. The bias in T_e becomes lower, but the bias in the n_e determination however becomes larger.*

The coarse correction method still yields rather large systematic deviations. Nevertheless, this correction method has been applied for bulk data analysis. The reason for this is that the method in fact only affects the absolute value of T_e and n_e, and is faster. Both correction methods are compared for two plasma conditions. For the convolution of the fitting function for the experimental data the same 1-D instrument profile as in the simulations above is used. Again the medium n_e Ohmic discharge, Fig. 5.11, and the low n_e ECH discharge, Fig. 5.14, are used. Figures 5.23 and 5.24 show the results for both correction methods. The relative profiles are very similar, i.e. the small scale structures in the profiles are the same for both methods. As expected from Figs. 5.20 and 5.22 the absolute values differ. The coarse correction method over-estimates T_e and under-estimates n_e compared to the method with the convolved fitting function. In conclusion, for the study of small scale structures on T_e and n_e the coarse correction method suffices.
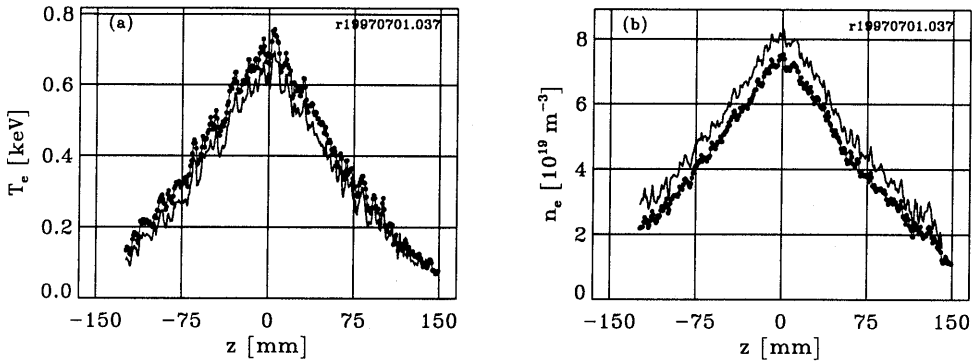
Figure 5.23: *(a) T_e and (b) n_e profile of an Ohmic discharge. The figures shows a comparison of two correction methods. The dots show the method in which a pedestal was subtracted from the spectra, and the full line the method in which a convolved fitting function was applied.*
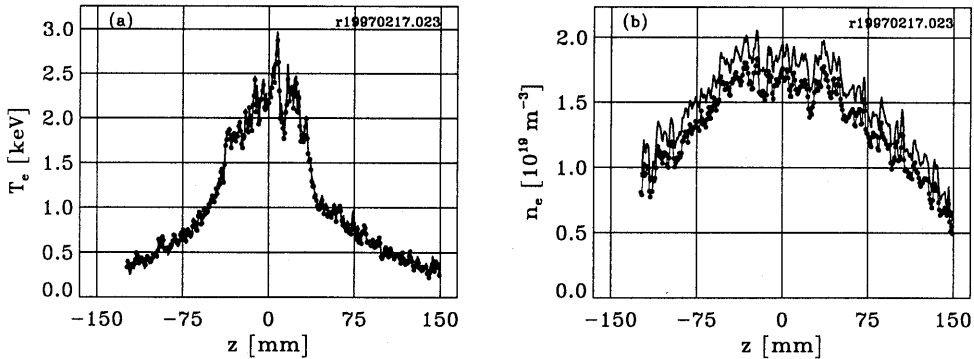
Figure 5.24: (a) T_e and (b) n_e profile of an additionally heated discharge. The figure shows a comparison of two correction methods. The dots show the method in which a pedestal was subtracted from the spectra, and the full line the method in which a convolved fitting function was applied.

5.7 Acknowledgments

References

[1] A.J.H. Donné, Plasma Phys. Reports **20** (1994) 192

[2] P.C. Liewer, Nucl. Fusion **25** (1985) 543.

[3] B.B. Kadomtsev, 'Tokamak plasma: a complex physical system' (Adam Hilger, Bristol and New York, 1992)

[4] C.J. Barth *et al.*, Rev. sci. Instrum. **68** (9), (1997) 3380-3392.

[5] M.N.A. Beurskens *et al.*, *"Double pulse multiposition Thomson scattering and dynamics of small scale T_e and n_e profiles in RTP"*, to be submitted to Rev. Sci. Instrum.

[6] N.J. Lopes Cardozo, *et al.*, Phys Rev. Letters **73** (1994) 256-259.

[7] M.N.A. Beurskens *et al.*, *"Structures in T_e profiles: high resolution TS in RTP"*, accepted by Rev. sci. Instrum.

[8] M.N.A. Beurskens *et al.*, Proc. of the 24th EPS conf. on controlled fusion and plasma physics, Berchtesgaden (1997), (**597**)

[9] D.F. Da Cruz, *et al.*, Phys Rev. Letters **75** (1995) 3685-3688.

[10] J. de Kloe, *et al.*, Proc. of the 24th EPS conf. on controlled fusion and plasma physics, Berchtesgaden (1997), (**593**)

[11] F. Salzedas, *et al.*, Proc. of the 24th EPS conf. on controlled fusion and plasma physics, Berchtesgaden (1997), (**589**)

[12] R.F.M. Meulenbroeks, *et al.*, Steady state off-axis sawtoothing near q=3/2, 2, 3 in a Tokamak, to be submitted to Phys Rev. Letters.

[13] N.J. Lopes Cardozo, *et al.*, Plasma Phys. Control. Fusion **39**, suppl. 12B, (1997) B303-B316.

[14] M. Mattioli, *"Incoherent light scattering from high temperature plasmas"*, EUR-CEA-FC-752 (1974).

[15] C.C. Chu *et al.*, *"Calibration of the RTP TS system"*, to be submitted to Rev. sci. Instrum.

[16] P.R. Bevington, *"Data reduction and error analysis for the physical sciences"*, ISBN 69-16942.

[17] A simple example to illustrate the working of the smoothing by the instrument profile. Consider a triangular instrument profile in the spatial direction with values $I=[0.25, 0.5, 0.25]$. Such profile would decrease the noise by a factor $\sqrt{\Gamma}$ with $\Gamma = 1/I^2 = 1/(2 \cdot 0.25^2 + 0.5^2)$=2.7. Apparently the profile in Fig. 5.8 is wider than the triangle in this example.

Chapter 6

Filamentation of the RTP tokamak plasma

Authors: M.N.A. Beurskens, N.J. Lopes Cardozo, E.R. Arends, C.J. Barth,
and H.J. van der Meiden.

6.1   Introduction

The tokamak is the most common type of machine used in thermonuclear research to confine a hot plasma by magnetic fields. It is presently the main candidate for a thermonuclear fusion reactor. Its beneficial properties of plasma confinement derive from the magnetic topology: in an idealised description the magnetic field lines form nested toroidal surfaces. In this picture, transport of heat or particles in the direction perpendicular to those surfaces is only possible through collisions (neo-classical transport), or through the action of fluctuating electric fields.

However, it is well known that the topology of nested surfaces is an idealisation. The field line equations form a Hamilton system, with as a generic mathematical property that surfaces on which the field line winding ratio (q) is rational are topologically unstable [1]. Under small perturbation, they degenerate to form magnetic islands. When adjacent chains of islands overlap, regions of chaotic field form. Thus, the generic topology of the magnetic field in a tokamak should be a mix of good surfaces, chains of islands, and regions with chaotic field lines. While this degeneration occurs for arbitrarily small perturbation of the magnetic field, it has been estimated that perturbations of the order $\tilde{B}_\phi/B_\phi > 10^{-5}$ are required to significantly enhance transport. In particular heat transport via electrons is sensitive to perturbations of the magnetic field topology.

The mathematical theory, which describes the topology of the phase space of a perturbed two dimensional Hamilton system, does not say anything about the level of perturbation to be expected in a tokamak. From the theory of tokamak plasmas, it is expected that e.g. tearing modes with high mode numbers should normally be stable. Recently, there has been an increased interest in the neo-classical tearing mode, which should occur at high pressure gradients. However, this mode is only unstable when it exceeds a critical size, and therefore needs a seed island to grow. Thus, the tearing mode stability analysis predicts that the formation of small magnetic islands should not occur unless the conditions for neo-classical tearing modes are met.

Experimentally, the evidence appears to point in the same direction. The observations of magnetic islands are virtually limited to the very large modes with poloidal mode numbers m=1 (the sawtooth pre- and post-cursors) and m=2 precursors to the major disruption. Such islands can reach a size of 20 % of the minor radius or more, and are easily detected with several diagnostics, e.g. [2, 3, 4].

The evidence of the occurrence of small magnetic islands is much scarcer. Observations of an m=3, n=2 have been reported from several experiments [5, 6], and recently the neo-classical tearing modes have been observed in e.g. [7]. These observations are consistent with the assumption that the magnetic topology in a tokamak is well described by the ideal set of nested flux surfaces, unless there are islands that are so large that they can be detected. However, to affect electron transport, it is sufficient that islands have a size comparable to the banana width, i.e. typically 1–10 mm. Such islands are very difficult to diagnose. For instance, to distinguish such islands a local flattening of the electron temperature (T_e) profile requires a measurement of the second derivative of T_e with a resolution of <3 % of the minor radius. This is out of the range of most tokamak diagnostic systems.
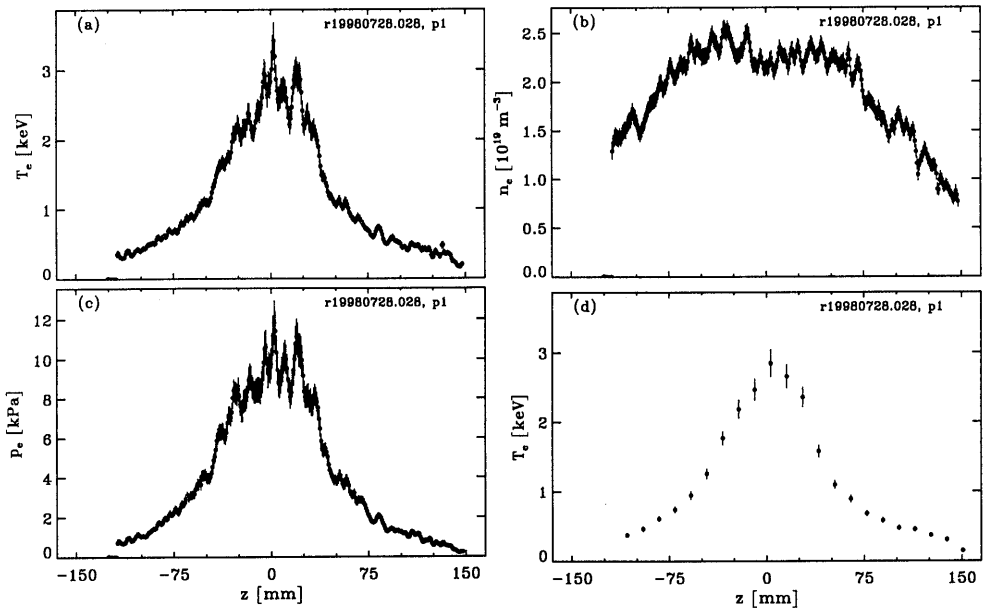
Figure 6.1: *Example of a high resolution TS measurement: (a) T_e, (b) n_e and (c) p_e profile of a central ECH plasma with q_a=6.2. The filaments are much more pronounced in T_e and p_e than in n_e. (d) The resolution of the RTP ECE-imaging diagnostic (1.3 cm FWHM) can be simulated by binning data points from the TS T_e profile shown in (a). Clearly, after binning no filaments are resolved anymore.*

Thus, in fact there is no compelling experimental evidence that the concept of ideal flux surfaces is correct in the sense that magnetic perturbations are below the level that is relevant for macroscopic plasma behaviour such as electron heat transport. Evidence in favour of such perturbations is also scarce. Measurements of fluctuations of the magnetic field in Tore Supra, using the cross-polarisation scattering of microwaves, showed

fluctuations at the level $\tilde{B}_\phi/B_\phi > 10^{-5}$ with a broad band frequency spectrum [8, 9]. It was estimated that these fluctuations could be responsible for the observed electron heat transport.

Other evidence for a broken magnetic topology was obtained at the Rijnhuizen Toka-mak Project (RTP). Measurements with a ultra high resolution Thomson scattering (TS) system [10], revealed that the T_e profile shows multiple peaks under intense local electron heating with Electron Cyclotron Heating (ECH). These were interpreted as hot 'filaments', i.e. closed flux tubes with an m/n=1 structure [11, 12]. Figure 6.1 gives a typical exam-ple. The typical width of the filaments is 5–10 mm, and they are much more pronounced on T_e than on n_e. The occurrence of filaments appeared to be limited to the low shear region inside the $q=1$ surface, and a coarse estimation yielded a life time of hundreds of microseconds. The steep gradients in the filaments as well as their life time could be un-derstood by assuming that the confinement inside a filament is very good, corresponding to a thermal diffusivity near the neo-classical value.

After the observation of plasma filamentation in RTP, a similar observation was re-ported from TEXT [13]. Using a high resolution ECE-Imaging diagnostic, strong spatial variations of T_e were observed in the central region of the plasma, under ECH. Using the high time resolution of the ECE, it was shown that the structures have an m/n=1 periodicity. In [13] it is suggested that the filaments are in fact an oddly shaped single magnetic island.

The observations of the hot filaments in RTP and TEXT raised many questions. The most important are:

- Are the filaments as measured with TS in RTP statistically significant?
- If they are, are the observed peaks in the T_e profile the cross-section of toroidally extended structures, or are they local temperature fluctuations? If they are spatial structures, are they closed flux loops? Or could the very local heating of a bundle of field lines in a chaotic region give rise to similar observations?
- Is there any relation between the occurrence of filaments and plasma parameters such as density and plasma current?
- Are the filaments ECH induced or is the ECH only high-lighting pre-existing fil-aments? And related: have filaments been observed in other conditions, without ECH?
- Are filaments restricted to the central, $q=1$ region, or are there observations of fila-mentation outside this area? Is low magnetic shear a requirement for the occurrence of filaments?
- Are the high resolution RTP measurements consistent with the TEXT interpretation of filaments as part of a single magnetic island?

In this paper we address those questions. Since the first observations of hot filaments in RTP the following steps have been made: The RTP TS diagnostic has been upgraded from single pulse to double pulse [6]. This allows a coarse study of the dynamics of filaments, and can e.g. bring out what happens to filaments during a sawtooth crash. An extensive study has been made of the spatial resolution and experimental errors of the new TS diagnostic, thus allowing a meaningful statistical analysis of the measurements [14]. An extended set of measurements of filamented T_e profiles has been made, in a variety of plasma conditions. The structure of this paper is as follows: In section 2 we briefly

describe the experimental set up, the high resolution T_e measurements, and we show how
the resolution obtained with TS is essential to resolve the filamentation in RTP. In section
3, the statistical significance of the observed structures in T_e is investigated. In section 4,
theoretical considerations are made in order to make an inventory of the possible topology
of filaments. Furthermore, two experiments are described which address the questions
1) whether or not the observed filaments are elongated in poloidal directions, and 2)
whether filaments are periodic, spatial structures or temporal fluctuations. In section 5
the dependence of filaments on plasma current and electron density is studied. For this
purpose a quantifier for filamentation is introduced. Section 6 presents an experiment in
which the time scale of filaments creation upon ECH switch-on is determined. Sections
7 and 8 answer the questions whether 1) filaments occur outside the $q \leq 1$ region and
2) whether filaments are ECH specific, respectively. In section 9 the effect of sawtooth
crashes on filaments is presented and section 10 shows the relation between filaments and
the m=n=1 sawtooth precursor.

   Thus, we come to a comprehensive description of the phenomenology of filamentation.
The discussion is interwoven in the separate sections and in section 11, all is summarised
and further worked out. The discussion then concentrates on a number of plasma physical
aspects of filamentation, such as the magnetic topology of a filament, the current density
perturbation in a filament and the energy balance in a filament. Finally, the importance
of filamentation for the understanding of transport in tokamak plasmas is addressed.

6.2   High resolution measurements

The Rijnhuizen Tokamak Project (RTP; $R/a = 0.72/0.165$ m, $B_T \leq 2.5$ T, $I_p \leq 150$ kA,
$q_a \geq 2$) is equipped with high power additional electron heating and an extensive set of
high resolution diagnostics [15]. A 350 kW, 110 GHz Electron Cyclotron Heating (ECH)
system can deposit heat in a very localised area ($\sim 10\%$ of the minor radius) in the plasma.
The ECH can be the dominant heat source, exceeding the total Ohmic power by an order
of magnitude. In an additionally heated plasma in RTP, electron temperatures (T_e) are
up to 4 keV at an electron density (n_e) of 2×10^{19} m^{-3}, while in a typical Ohmic plasma
the central T_e reaches 0.7 keV. An extensive set of high resolution diagnostics include a 20
channel Electron Cyclotron Emission (ECE) radiometer measuring T_e along a horizontal
line, a 16 channel ECE imaging (ECE-I) diagnostic measuring T_e along a vertical line,
a 19 channel FIR interferometer, and an 80 channel 5 camera soft X-ray tomographic
system. Of these, the ECE systems offer the best spatial resolution of ≥ 1.3 cm, i.e. 8%
of the minor radius.

   Crucial for the present paper is the double pulse multiposition TS diagnostic [6]. It
measures T_e and n_e, in a snapshot of 40 ns, at 350 points along a vertical chord of 300 mm.
Its spatial resolution is 3 mm Full Width Half Maximum (FWHM), i.e. 2% of the minor
radius. It measures two profiles per discharge with a tunable time separation of 20–800 μs,
enabling a study of the dynamics of small scale structures in the plasma. Its statistical
relative error is 3–5% of T_e and 2–4% of n_e for T_e in the range of 50 eV–6 keV, and
$n_e = 5 \times 10^{19}$ m^{-3} [14]. The systematic relative error on the values of T_e and n_e may be
larger, but this does not influence the study of small scale structures [14].

   At RTP, the diagnostic with the second best resolution is the ECE-I diagnostic. This

diagnostic measures T_e at 16 points with a spatial resolution of 1.3 cm FWHM. The 16 points are measured along a vertical chord in the same poloidal cross-section as the TS chord. Depending on the value of the toroidal magnetic field, the TS and ECE chords can overlap each other. Unfortunately, this diagnostic can not resolve the filaments in RTP. Firstly, the spatial resolution is of the order of the size of larger filaments, as is illustrated in Fig. 6.1. Secondly, because ECE-I and ECH at RTP both operate at the second harmonic of the electron cyclotron frequency, central ECE-I measurements are not possible during central ECH.

6.3 Statistical significance of filaments

The first question to be addressed concerning the observations of filaments, such as shown in Fig. 6.1, is whether they are a plasma physical phenomenon or a diagnostic artefact. The evidence that they are a plasma physical phenomenon consists of the following. In this paper results are presented:

1. showing that filaments are periodic structures that reappear in the TS profile after a full rotation of the plasma (section 6.4);
2. showing that the amplitude of the filaments depends on plasma parameters such as density and plasma current (section 6.5);
3. showing that in the initial period after switching on the ECH, it takes several milliseconds for the filaments to form, while T_e and n_e reach their equilibrium values much faster (section 6.6);
4. showing that filaments that were still there just before a sawtooth instability, have disappeared directly after the sawtooth collapse (section 6.9).

Each of these observations is very difficult to interpret when the filaments are a diagnostic artefact.

In addition to the experimental evidence, in this section a statistical test is performed of the presence of filaments in an ensemble of 22 similar discharges, taken at one day. All three T_e, n_e and p_e profiles are analysed, to show that the amplitude of structures on n_e is smaller than those on T_e and p_e. The test uses an estimation of the statistical errors on the three parameters, which is the result of a detailed error-breakdown of the TS measurements [14]. The 22 discharges had central ECH, $q_a \approx 4.6$ and $n_e(0)$ $\approx 2.4 \times 10^{19} \mathrm{m}^{-3}$.

For this data set, a power spectrum of the fluctuations in the T_e, n_e and p_e profiles is calculated and compared to the -known- noise spectrum. Figure 6.2 shows the profiles of a typical example taken from the test series of 22 discharges. To suppress spurious contributions of the global profile shape and parts of the profile that do not show filamentation, i) the analysis is restricted to the z-range [-40,40] mm, and ii) a smooth profile is subtracted from the measured profile to obtain a high pass filter. The smooth profiles, $T_{e,2cm}$, $n_{e,2cm}$ and $p_{e,2cm}$, are obtained by convolving the measured profile with a Gaussian, with 20 mm FWHM. This high pass filter leaves the filaments, which typically have a size of 5–10 mm, intact (see Fig. 6.2). The 22 thus obtained profiles of the central part of $\tilde{T}_e$ $= T_e$ - $T_{e,2cm}$, are normalised to $T_{e,2cm}$, and merged to form one long array (the same is done for n_e and p_e). The power spectrum of this array is shown in Fig. 6.3, along with the power spectrum of the noise of the measurement. Note that the decay of both the noise
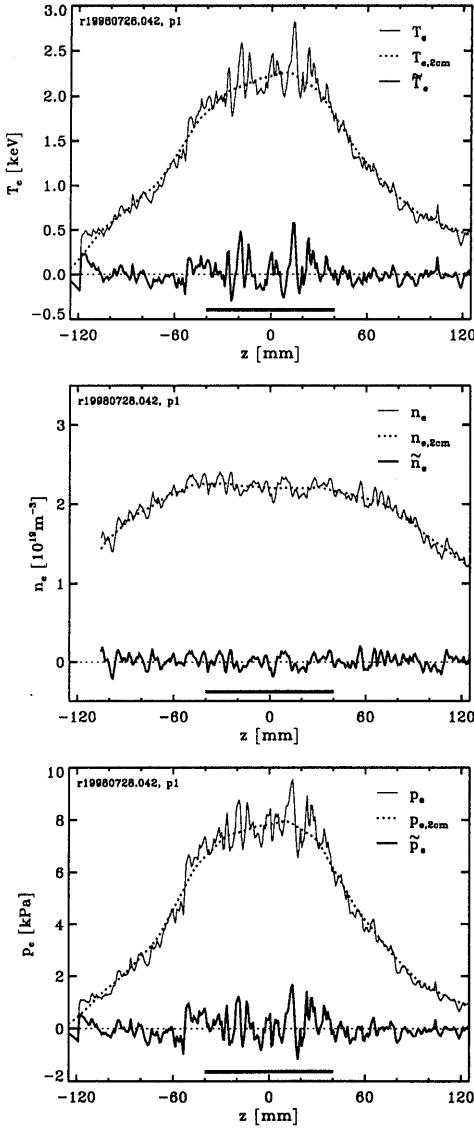
Figure 6.2: *Typical profiles of T_e (thin line), $\tilde{T}_e$ (thick line), n_e, $\tilde{n}_e$, p_e and $\tilde{p}_e$ of a plasma with central ECH. The fluctuation profiles are obtained by subtracting a smooth profile ($T_{e,2cm}$, $n_{e,2cm}$ and $p_{e,2cm}$) from the measured profile (see text). The horizontal bar drawn from $z = [-40,40]$ mm, shows the area to which the power spectrum analysis is restricted.*
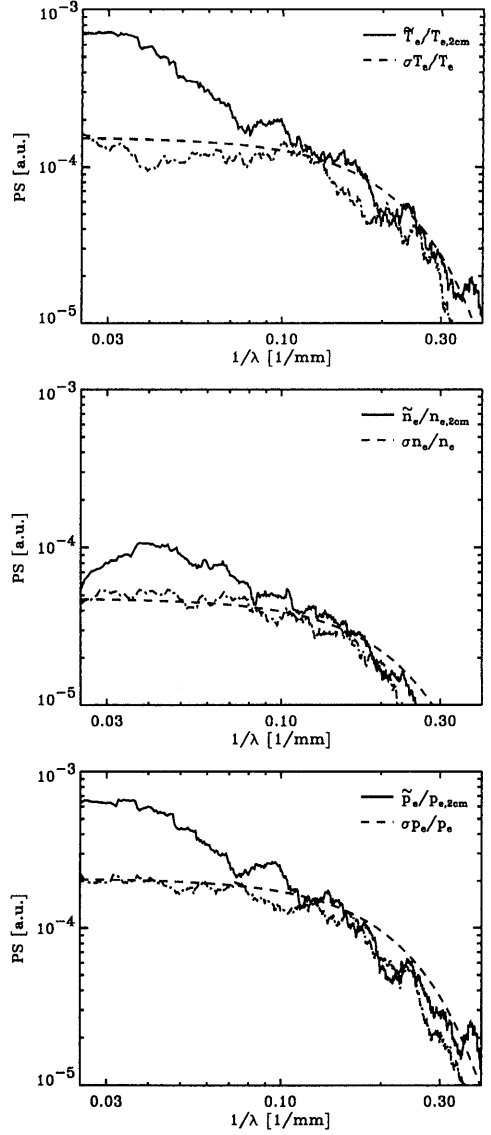
Figure 6.3: *Power spectrum (for 22 discharges) of $\tilde{T}_e/T_{e,2cm}$, $\tilde{n}_e/n_{e,2cm}$ and $\tilde{p}_e/p_{e,2cm}$ (drawn) compared to the power spectra of simulated noise σ_{T_e}/T_e, σ_{n_e}/n_e and σ_{p_e}/p_e (dash-dot). Overplotted (dashed) is the noise characteristic of a Gaussian filter with 2.4 pixels FWHM. The simulated noise comes out somewhat lower.*

and the measurement at $1/\lambda > 0.2$ mm^{-1} is due to the convolution with the instrument function, i.e. a Gaussian with 2.4 pixel FWHM. The fact that measured spectrum and noise characteristic in this range fall on top of each other, shows that the noise level is correctly estimated.

Figure 6.3 shows that the measured spectra are well above the noise in the wavelength range between the applied high pass filter (the suppression of wavelength longer than 4 cm by the subtraction of the smoothed profile) and the cut-off above $1/\lambda = 0.16$ mm^{-1} due to the instrument function. Thus, all three T_e, n_e and p_e have significant structures. However n_e structures have almost one order of magnitude smaller amplitude than T_e and p_e structures.

While in the measured T_e (and p_e) profiles the typical width of the filaments is 5–10 mm, the spectrum does not peak at the corresponding wavelength of $\lambda=10$–20 mm, nor should this have been expected. The peak in the spectrum should represent the average spacing of the filaments, which for $1/\lambda=0.02$–0.05 corresponds to 2–5 cm, or one to four filaments in the central region. The higher frequencies in the spectrum are generated by the irregular occurrence of the filaments, and the fact that their half-width is smaller than their interspacing. The fact that the spectrum does approach the noise level around $1/\lambda=0.1$ indicates that filaments with a width smaller than 5 mm are rare, but the proximity to the resolving power of the diagnostic prohibits any strong conclusion here.

In conclusion, the spectral analysis supports the hypothesis that in the measured T_e profiles of centrally heated discharges in RTP, statistically significant filaments are observed with the following properties:

1. typical occurrence: several filaments in the region [-40,40] mm;
2. typical width larger than 5 mm, and smaller than the average half interspacing of about 20 mm.

This agrees with the conclusions of a visual inspection of a series of profiles, in which typically 1 to 4 filaments with a width of 5-10 mm are observed.

6.4 Topology of filaments

6.4.1 What are the options?

In section 6.3 it was argued that the observed filamentation of the T_e profile cannot be ascribed to a diagnostic artefact. Interpreting the filaments as a plasma physical phenomenon, the first question to be addressed is: what is the topology of the filaments, i.e. what is their shape in 3-dimensional space. We consider a few possibilities, between which we shall try to distinguish on the basis of experimental material as well as theoretical considerations:

1. What appears as filaments in the T_e profile are fast, local T_e fluctuations which are recorded in the 40 ns snapshot of the TS measurement;
2. A filament is a bunch of neighbouring field lines which cross the ECH heating zone but do not form a topological entity such as a magnetic island. Around the bunch of field lines no confinement improvement is achieved. In particular, the field lines could be living in a sea of chaotic field.

3. What appears as filaments are different cross-sections of an oddly shaped magnetic island, with an m=n=1 mode structure (this is the interpretation proposed in [13].

4. The filaments are independent flux tubes, each closing back on itself (possibly with an m=n=1 periodicity). The tubes have a 'shielding' surface with low diffusivity.

Note that in the cases 2–4 it is still well possible and also likely that the filaments do change with time. However, if spatial structures live for many collision times and local current diffusion times, the spatial structure can be regarded as the essential feature.

The measurement of filamentation at TEXT with fast sampling ECE showed that the filaments have an m=n=1 structure [13]. This argues against option 1. In the remainder of this section we will show that with double pulse TS, filaments appear only slightly changed in the TS profile after a full period of plasma rotation. This, too, argues against option 1. Further, as was already shown in [11, 12], filaments live on for several tenths of milliseconds after ECH is switched off, and this again is difficult to square with option 1. Upon switching on ECH, it even takes milliseconds for the filaments to develop, as is shown in section 6.6. Finally, a Thomson scattering T_e measurement is based on the velocity distribution of the bulk of the electron population, with energies below the energy at which the ECH is absorbed. It is difficult to imagine fast T_e fluctuations in the thermal bulk of the population. Certainly on a time scale faster than the collision time (i.e. about 100 kHz) the meaning of such fluctuations would be unclear. Thus, there is ample evidence that the filaments are spatial structures.

Option 2, the bunch of field lines highlighted by ECH, too can be rejected on the basis of several arguments and measurements. First, as is shown in section 6.6, filaments take milliseconds to develop after ECH is switched on, and tenths of a millisecond to disappear after ECH is switched off. These observations are at variance with the picture of highlighted field lines in a chaotic sea. Second, to highlight a small region in a chaotic sea, a very strong T_e gradient must be sustained along the field lines. Assuming that the typically 2–3 observed filaments are all the same bunch of 'hot' field lines, a temperature difference of up to 1 keV must be sustained over a distance of 2 toroidal transits, or 10 m in RTP. This requires a thermal diffusivity of 4 orders lower than the classical one. This argument becomes even stronger if the finite time any collection of field line is in the heating zone is taken into consideration.

Thus, the filaments can only be understood if they are closed, toroidal structures. To distinguish between options 3 and 4 requires a more subtle analysis. In [13] a pseudo-tomography of the filamented central region of the poloidal cross-section is using the time resolved ECE measurements and the rotation of the plasma. The result shows that what appears as filaments in a 1-dimensional T_e profile, forms a single m=n=1 island with a very complex shape. This island, and thus the filaments are then equated to the sawtooth precursor. In section 6.10 we show extensive experimental data from RTP which contradicts this interpretation. With the double pulse TS measurement no pseudo-tomography can be constructed. However, two sets of experiments were conducted to distinguish between the interpretations 3 (oddly shaped island) and 4 (individual filaments). These are i) (section 6.4.2) taking TS profiles at different positions relative to the magnetic axis, so as to check if the appearance of the filaments depends on their proximity to the q=1 surface and ii) (section 6.4.3) using the plasma rotation to investigate the reproduction of the filaments after a full plasma rotation. The results of both are consistent with filaments as individual structures, rather then part of a single magnetic island.
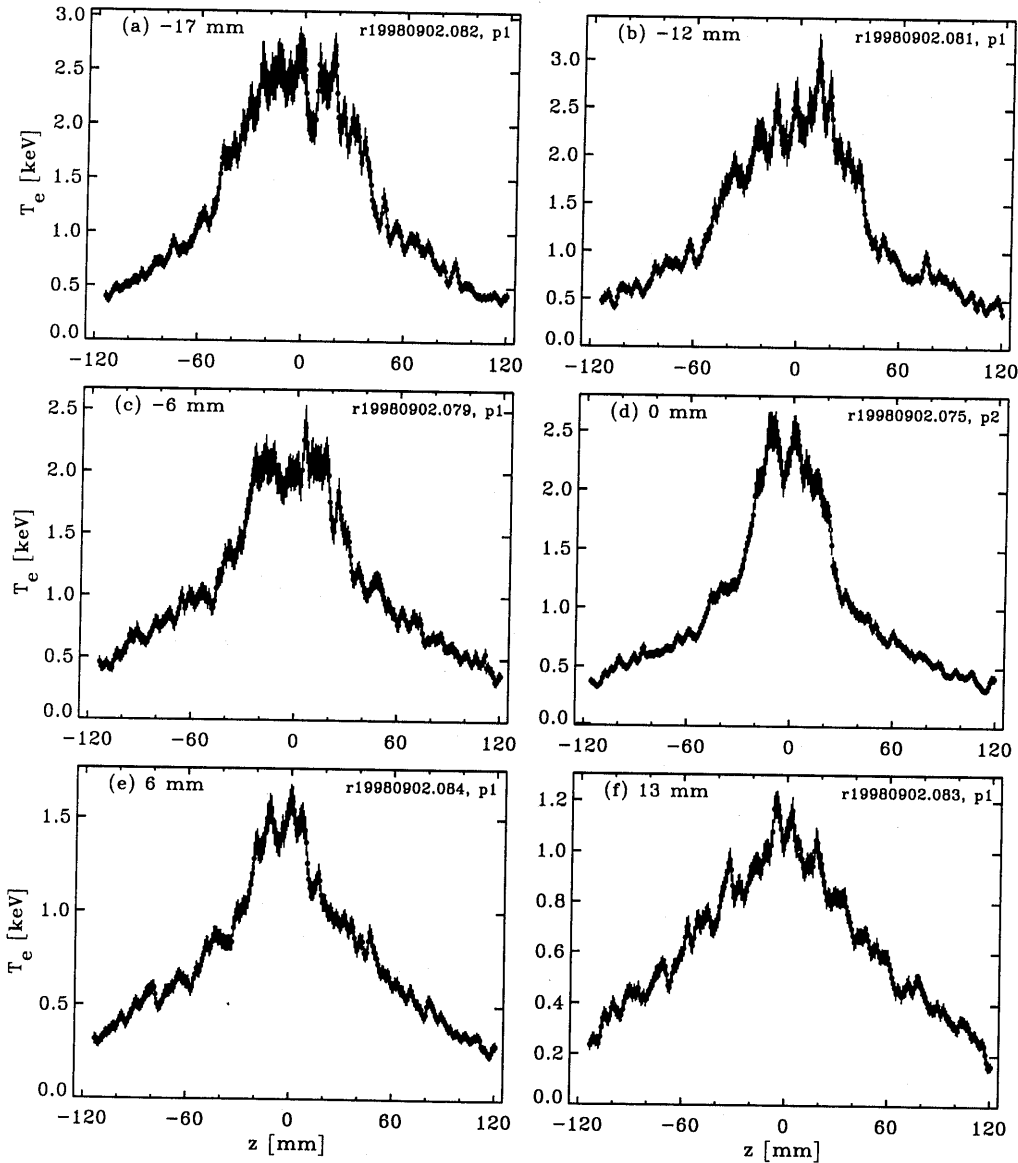
Figure 6.4: *Measured T_e profiles of plasmas that were horizontally shifted with $\Delta R=$ (a) -17 mm, (b) -12 mm, (c) -6 mm, (d) 0 mm, (e) 6 mm, and (f) 13 mm. All profiles show single peaks. The profiles (a)–(d) have a line integrated density of $4–4.5 \times 10^{18} m^{-2}$, while for (e) and (f) the line integrated density is $\sim 6 \times 10^{18} m^{-2}$.*

6.4.2 Thomson scattering profiles: scan of the major radius

The TS laser shoots vertically through the plasma. It is aligned to the geometrical center of the poloidal cross section of the torus, which normally is the center of the last closed flux surface. With a Shafranov shift of 20 mm, the TS profile misses the magnetic axis of the plasma. RTP has two plate limiters at the top and bottom of the torus. The

plasma can be shifted radially by up to $\Delta R=\pm 20$ mm in the equatorial plane. In a series of discharges, ΔR was varied on a shot to shot basis between -17 and +13 mm. All discharges were centrally heated with ECH, and had $q_a=4.6$. Unfortunately, the shift of the plasma did affect the density. The line integrated density varied between 4 and 6×10^{18}m^{-2} in this series. There is a strong dependence of the filamentation amplitude on the density (see section 6.5.3) for which we did not correct.

In Fig. 6.4 six T_e profiles from this series are shown. First we note that the steep gradient, which marks the position of the q=1 radius [16], is largest for ΔR=-17 mm, while for ΔR=+13 mm the hot core is only barely touched or perhaps missed altogether. This is in agreement with the estimated Shafranov shift of 20 mm. The appearance of the filaments does not depend on the cross section. There are always multiple peaks, which are distributed rather randomly over the hot core.

This is consistent with the picture that filaments are individual, closed tubes. If filaments were different cross-sections of a single island, profiles intersecting the hot core close to the q=1 radius should not show filamentation.

6.4.3   Appearance of filaments under plasma rotation

In RTP, MHD modes as measured with ECE or SXR diagnostics usually appear at a frequency of 10–15 kHz (they can slow down if the modes become very large). Thus, the same cut of the TS laser through a poloidal cross-section is obtained after an interval of 60 to 100 microseconds, which is in the range of the double pulse TS diagnostic. With only two high resolution T_e profiles per discharge, it is not possible to make a pseudo-tomogram, but it is still possible to distill some interesting information from the double pulse measurement.

We first report the results of experiments in which it was tried to match the interval between the two TS laser pulses to the rotation period of the plasma. To this end, plasmas were selected with a combination of filament conditions (central ECH, low density), and the presence of some MHD activity. Filaments and MHD-activity can well coexist, as is discussed in section 6.10.

Figure 6.5 shows an example of a central ECE trace, which shows the presence of a large rotating m=n=1 mode in a centrally heated plasma. The separation time of the TS , Δt_{TS}, set equal to one rotation period of the mode, τ_{MHD}, is indicated in the figure. The resulting T_e profiles are shown in Fig. 6.6 (a). Both profiles clearly show the presence of the mode, and the shifted hot core appears very similar in both. Figure 6.6 (b) gives measured profiles in a similar shot, which did not show MHD activity. The TS time interval was the same, and it is reasonable to assume that τ_{MHD} was unchanged too, although in the absence of a clear oscillating signal this could not be measured. In this case, the two TS measurements show very good agreement. In particular, both profiles show clear filaments, and they are very similar in the two profiles.

In series of discharges in which it was tried to find reproduction of filaments between two laser pulses, such correlation was only achieved when the TS pulse separation matched the MHD frequency to within a few percent, which only happens accidentally since we could not control the MHD frequency so precisely, or trigger on the MHD signal with sufficiently short response time.
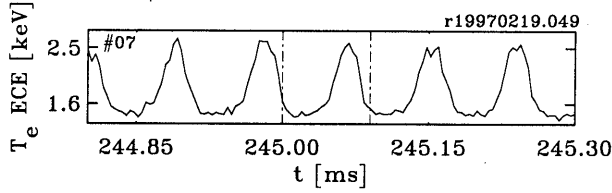
Figure 6.5: *Time trace of a central ECE channel showing the rotation of a large m/n=1/1 mode. The timing of the TS is set to 90 μs, which is approximately one period of rotation.*
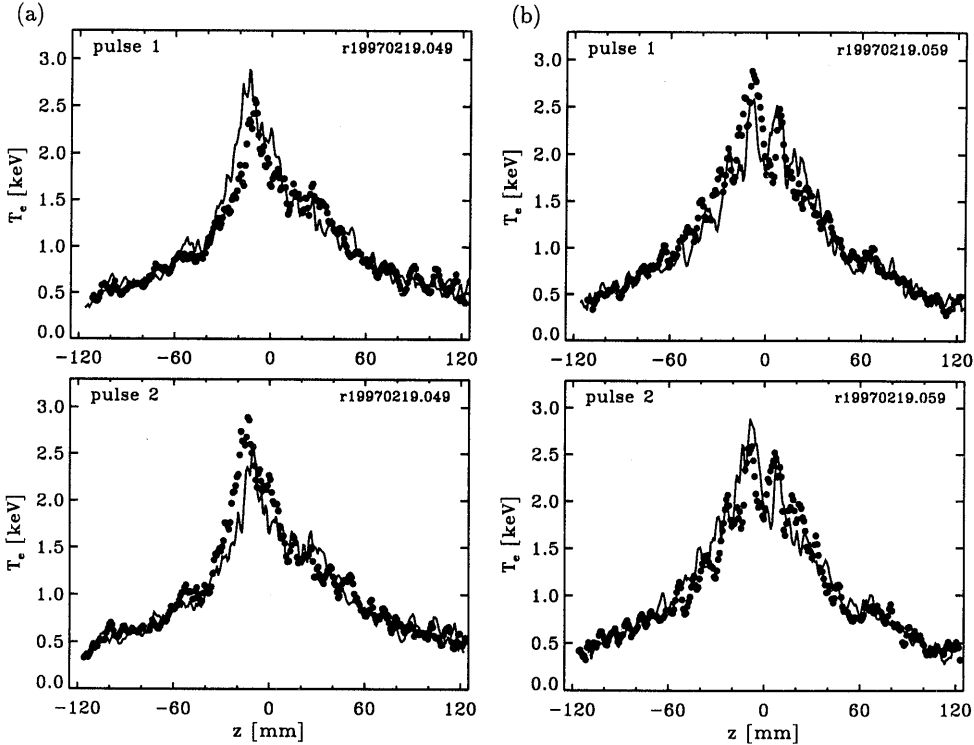
Figure 6.6: *Two examples of double pulse TS measurements with $\Delta t_{TS} \approx 1 \times \tau_{MHD} = 90\,\mu s$. The first pulse is overplotted in the figure for the second pulse and vise versa. (a) Both profiles show the reproduction of the very peaked hot core in the left wing of the profile and the low T_e area in the right wing. (b) The two filaments near z=-10 and +10 mm are reproduced. In this case no large mode was present. For both (a) and (b) $n(0) = 2.0 \times 10^{19}\,m^{-3}$, and $q_a \approx 6$, $B_\phi \approx 2\,T$, and $I_p = 60kA$. The error bars are left out for clarity.*

A very important result is, that when the period is not matched within a few percent, we found no correlation between the observed filaments in the two TS measurements. The experimental findings can be understood if filaments are individual, tube like structures. Figure 6.7 illustrates how sensitive the measured TS profiles are for the exact phase of the plasma rotation. Here, it should be realised that the T_e gradient inside the filaments is very large, so that a shift of only 2 millimeter (which at a radius $r=2$ cm corresponds to a

rotation angle of 0.1 radian) can make a filament appear very differently in the measured profile. Thus, this picture is consistent with the experimental result that reproduction of filaments is extremely hard to achieve, and only happens when the MHD rotation period and the TS separation time are matched within a few percent. Conversely, if the measured filamented profile were a cut through a single, though oddly shaped, magnetic island, reproduction of at least the main features of the profile should be simple to achieve, being much less sensitive to the exact rotation phase.

In the above discussion it has been assumed that the life time of filaments is longer than the MHD rotation period. This is a reasonable assumption in the light of the observations on both TEXT and RTP: based on their persistence after ECH is switched off, the life time of filaments in RTP was estimated at several hundreds of microseconds [11].
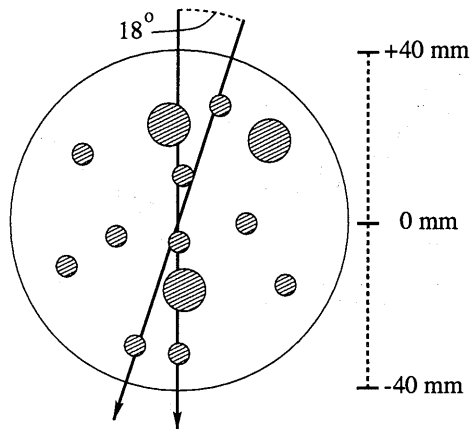
Figure 6.7: *Schematic drawing of a poloidal cross section of a filamented plasma center. The small circles indicate tube-like filaments of 5 and 10 mm diameter. The arrows indicate the laserbeam paths. If the rotation time of the plasma is mismatched in the double pulse measurement by 5 %, then filaments seen by the first TS pulse are missed by the second pulse.*

6.4.4   Conclusion

In conclusion, based on a variety of experimental results and theoretical considerations, we have concluded that filaments have to be spatial structures that close back on themselves after a toroidal transit. By studying their appearance in different cross-sections of the central plasma, either by shifting or rotating the plasma, evidence was obtained supporting the hypothesis that filaments are individual flux tubes, rather than aspects of a single island. In the present experiment the habitat of filaments is the region inside the $q=1$ surface. Most probably their mode structure is m=n=1, but also higher mode numbers are possible, e.g. m/n=7/8 or 8/9. As will be shown in section 6.7, filaments can also be found when the q-profile has an off-axis minimum at a value different from 1.

6.5 Parametric study of filaments in ECH plasmas

6.5.1 A quantifier for filamentation

It has been shown that filaments are significant and are periodic structures in the plasma. In this section the dependence of filaments on plasma current and electron density is studied. Before doing this, a quantifier for filamentation must be defined. On a shot to shot basis the measured amplitude of the filaments can vary rather much, even if the filaments themselves are the same, as was explained in Fig. 6.7. Furthermore the position and the width of the filaments are subject to variation. In this section a simple quantifier for filaments is introduced that only takes the amplitude of the filaments into account. Figure 6.8 shows how this quantifier is defined. The figure shows both an ECH plasma and an Ohmic plasma. For each profile a 'lower' and 'upper' profile are defined. The lower profile goes through the minima of the T_e profile and the upper profile through the maxima. The 'lower' and 'upper' profiles are drawn by hand. Clearly, for the ECH plasma the difference between the lower and upper profile is larger than the deviation for the Ohmic profile. A simple quantifier for filamentation, Θ_{T_e}, is now introduced, which is the maximum difference between the lower and upper profile. For the examples in Fig. 6.8 Θ_{T_e}=650 eV for the ECH plasma, and Θ_{T_e}=110 eV for the Ohmic plasma.

The advantage of this method is that the width and the number of filaments does not matter for the value of the quantifier. Equally filamented plasmas can still yield T_e profiles with different filament amplitude, as was illustrated in Fig. 6.7.

To check the usefulness of the quantifier Θ_{T_e}, two similar sets of discharges with central ECH were compared. Both sets have average $q_a = 5.9\pm0.15$, $I_p = 60$ kA, and central density $n_e(0) \approx 2.1 \times 10^{19}$m^{-3}. They where taken more than one year apart. One, taken in February 1997 with 25 discharges, has an average quantifier of Θ_{T_e}=590 ± 30 eV, and the other, taken in July 1998 with 13 discharges, has an average quantifier of Θ_{T_e}=625 ± 30 eV. Thus, the quantifier gives similar values for the two data sets, with the same plasma conditions.
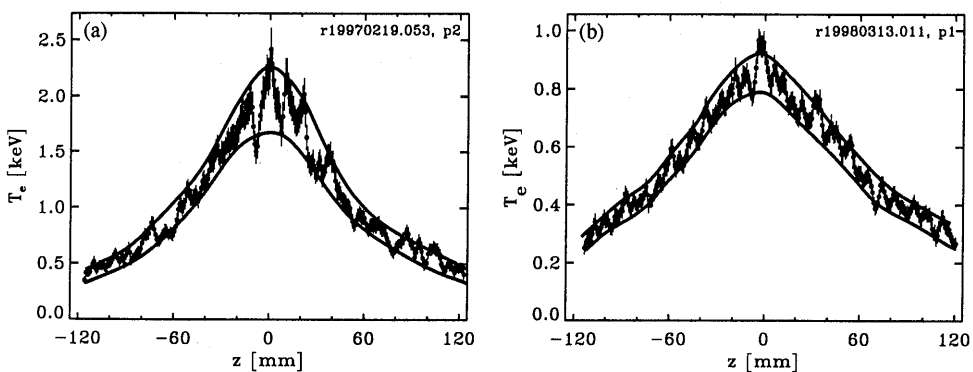

Figure 6.8: *Example of a 'lower' and 'upper' profile of T_e in (a) an ECH discharge, q_a=6.0 $n_e(0)$=2.0×10^{19} m^{-3}, and (b) an Ohmic discharge, q_a=5.1 and $n_e(0)$=2.9×10^{19} m^{-3}. The maximum deviation between the lower and upper profile is the quantifier for filamentation Θ_{T_e}.*

6.5.2 q_a dependence

Four series, each containing discharges with similar q_a, are used in the comparison. The series have $q_a \approx 3.7$, 4.6, and twice 5.9 respectively. To vary q_a, the plasma current was varied: I_p=100, 80 and 60 kA. The toroidal field $B_\phi \approx 2$ T, and the plasma density was $n_e(0) \approx 2.1 \times 10^{19}\text{m}^{-3}$ for all series. Figure 6.9 shows three examples of T_e profiles for each of the three values of q_a. The filament amplitude expressed in average Θ_{T_e} is plotted in Fig. 6.9 (d). The figure shows a weak dependence of Θ_{T_e} on q_a. The data is presented in a double logarithmic plot. The fit in the figure shows $\Theta_{T_e} \sim q_a^{0.4}$.

Filaments are found in the hot central region bounded by steep gradients near q=1. The size of this region depends on q_a, and can be approximated by the empirical relation $r_{q=1} = a/q_a$. A simple model is that the number of filaments scales with $r_{q=1}^2$, and that the filament amplitude scales with the power per filament. This model would yield a strong q_a dependence of the filament amplitude: $\Theta_{T_e} \sim q_a^2$. Clearly, this is not the case.

Another possibility is that the filament creation is limited to the ECH deposition region, which is much smaller than the cross section inside q=1. (The diameter of the ECH deposition is about 20 mm , while, according to the simple relation above, the diameter of the region inside q=1 varies with q_a from 60–90 mm.) In this case the filament amplitude should be independent of q_a: $\Theta_{T_e} \sim q_a^0$.

The experimentally found $q_a^{0.4}$ relation lies between the two simple models.

6.5.3 n_e dependence

Figure 6.10 shows a T_e profile of a plasma with central ECH and $n_e(0)$=4.3×10^{19}m^{-3}, q_a=6.1, I_p=60 kA. It is clear that it shows much less filamentation then the profile in Fig. 6.9(a), which has similar condition but lower n_e.

For three series of discharges at different densities the filamentation quantifier has been applied. Plasma parameters were: $q_a \approx 6.0$, I_p=60 kA, $B_\phi = 2$ T, and The three densities: $n_e(0)$=2.1, 2.9 and 4.3×10^{19}m^{-3}. Figure 6.10 (b) shows the decrease of filament amplitude with increasing density, in a double logarithmic plot. The dependence is described by $n_e^{-1.5}$.

Thus, the filament amplitude is a strongly decreasing function of the density. As will be shown in section 6.11, a power balance analysis yields a value for the thermal diffusivity which is close to the neo-classical value. Assuming that the transport in the filament scales as neo-classical transport, yields the following relation or the filament amplitude:

$$\theta_{T_e} \sim \frac{\sqrt{T_e}}{n_e^2} \tag{6.1}$$

Experimentally, a weak dependence of T_e on n_e is found, so that on the basis of neo-classical transport a density scaling of the filament amplitude is predicted which is close to the observed one.

In conclusion, a strong dependence of the filament amplitude as found in the experiment is not surprising in the light of the power balance of a filament. The density scaling is close to that expected when the transport inside a filament is neo-classical. The power balance of filaments is discussed in more detail in section 6.11.
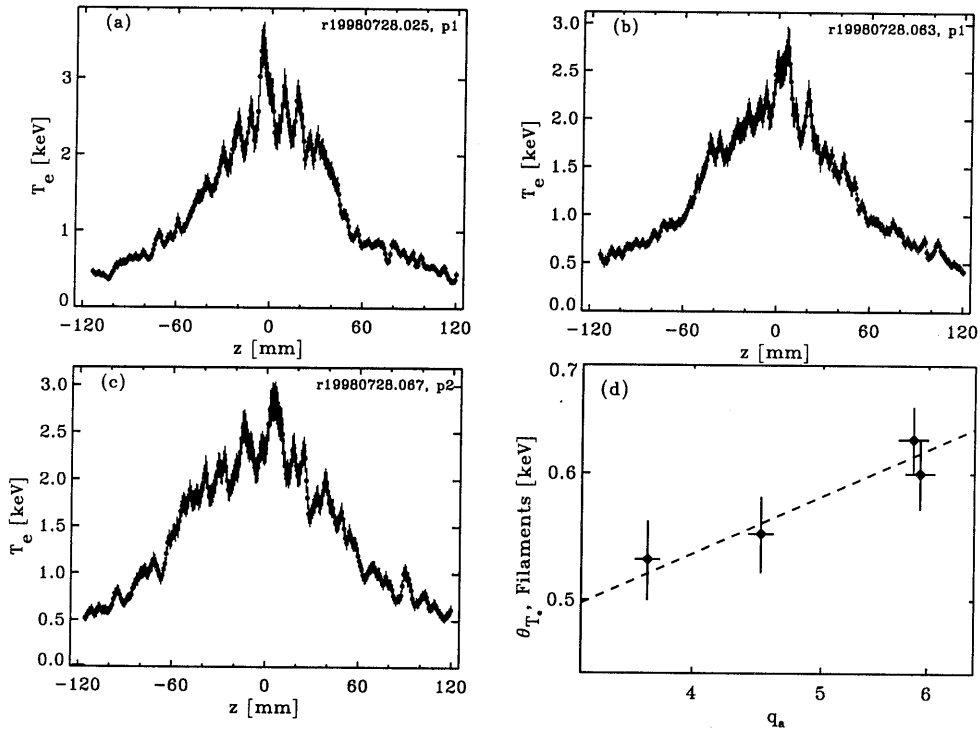
Figure 6.9: T_e profiles of plasmas with central ECH and different values of q_a. (a) $q_a = 6.1$ (b) $q_a = 4.6$ and (c) $q_a = 3.7$. $n_e(0) \approx 2.5 \times 10^{19} m^{-3}$. (d) Double logarithmic plot of Θ_{T_e} as a function of q_a. The dependence is weak, $\Theta_{T_e} \sim q_a^{0.4}$, and is overplotted with a dashed line. The values of Θ_{T_e} are an average for four series of discharges: $q_a \approx 5.9$: 2 series with 13 and 25 double pulse measurements, $q_a \approx 4.5$: 25 double pulse measurements, and $q_a \approx 3.7$: 9 double pulse measurements.
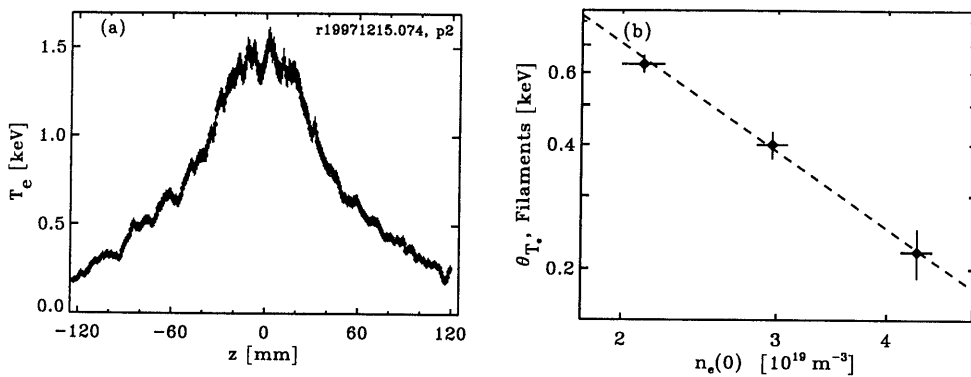
Figure 6.10: (a) T_e profile of a plasma with central ECH, $q_a = 6.1$, $B_\phi = 2$ T, $I_p = 60\,kA$ and $n_e(0) = 4.3 \times 10^{19} m^{-3}$ (b) Double logarithmic plot of Θ_{T_e} as a function of $n_e(0)$. The dependence is very strong, $\Theta_{T_e} \sim n_e^{-1.5}$ indicated by the dashed lines. The average q_a is 5.9 for all three series.

6.6   Time scale of filament creation

In section 6.4.1 four options for the physics of filaments were discussed. The first two options were: i) filaments as fast local T_e fluctuations, and ii) filaments as a bunch of ECH heated neighbouring field lines. These were rejected on the basis of arguments amongst which the creation upon switch-on and life time after switch-off of ECH were mentioned. Filaments live for several tenths of milliseconds after the switch off of ECH [11]. In this section the switch-on experiment is discussed.

Figure 6.11 shows a sequence of single pulse T_e profiles measured after ECH switch-on in well reproducing discharges. The profiles are taken 0.85, 1.85, 3.85, and 5.35 ms after switch-on. The central T_e rises and the figure shows that the filament amplitude increases. It is important to note that even though the line integrated density of these discharges remains constant, the central density decreases because the n_e profile becomes less peaked during the ECH phase. The line integrated density is $5\times10^{18}\mathrm{m}^{-2}$ for all discharges, but the central density decreases from $2.8\times10^{19}\mathrm{m}^{-3}$ (0.85 ms after switch-on) to $2.4\times10^{19}\mathrm{m}^{-3}$ (5.35 ms after switch on)

The filament quantifier has been applied on these single profiles. The $1/n_e^{1.5}$ effect found in section 6.5.3 has been used to correct the value for Θ_{T_e} for the central density decrease. Figure 6.12 shows the development of the filament quantifier in the ECH switch-on phase. Each point in the figure represents a single TS observation and is not an average over many shots. Therefore the indicated error bars are large. At $t=0$ ms the amplitude of Θ_{T_e} for a typical Ohmic plasma is taken, which is $\Theta_{T_e}=100\pm50$ eV. The saturation level at 550 eV is obtained from the series at $q_a=4.5$ in Fig. 6.9.

Although the error bar on Θ_{T_e} is large for an individual shot, the measurements clearly show that the filaments develop gradually, taking 5 milliseconds to reach the saturated amplitude. The associated time constant is estimated at 3 ms.

The time constant of the central T_e rise is 1.5 ms. If the filaments were pre-existing structures that only needed to be heated by the ECH, they should reach their full amplitude within several hundreds of microseconds. Indeed, as is shown in section 6.9, when filaments have disappeared in a sawtooth crash, it takes only a few hundred microseconds for them to reappear. Thus, the time constant for filament creation after ECH switch-on should be interpreted as the time needed to create the required conditions for filamentation. The fact that it is longer than the core energy confinement time suggests that current diffusion, i.e. the modification of the q-profile might play a role in this process. This gives further support to the hypothesis that filaments are magnetic structures.

The observed long creation time rejects the possibility that filaments are pre-existing structures, that were already there in the Ohmic phase. However, the question if filaments are ECH induced phenomena is not answered by this experiment: the ECH may only be needed to create the required conditions for filamentation. This subject is discussed in more detail in section 6.8.
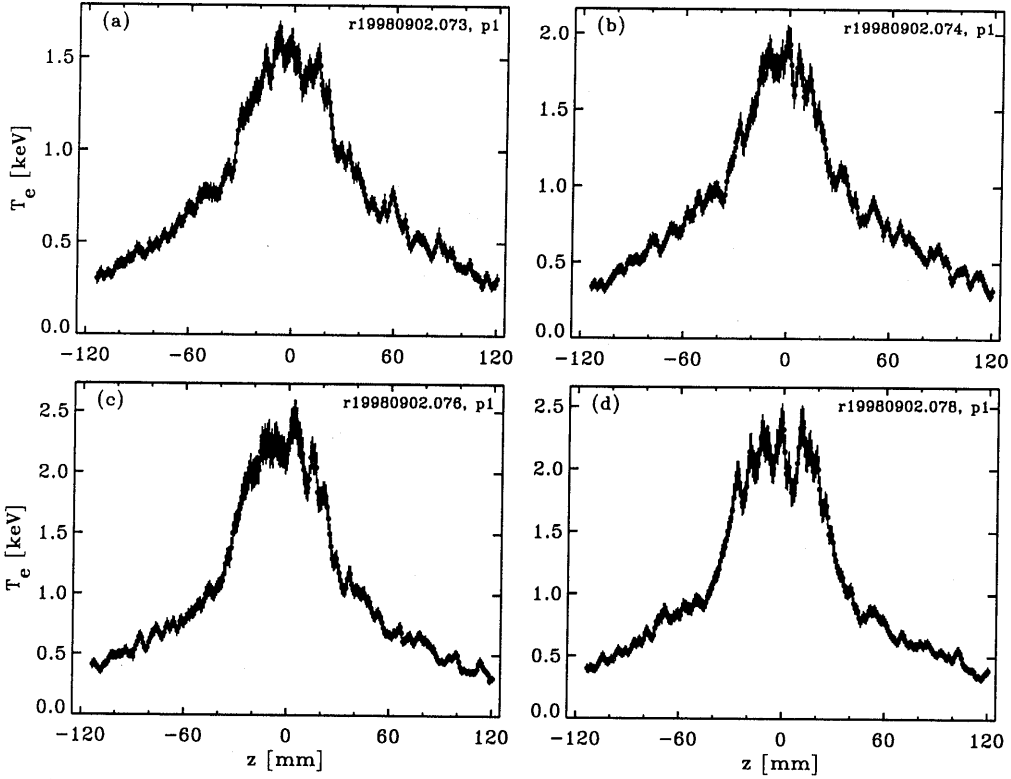
Figure 6.11: T_e profiles at different timing after ECH switch-on: (a) 0.85 ms (b) 1.85 ms, (c) 3.85 ms, and (d) 5.35 ms. The central filament amplitude increases. The discharges presented have $q_a \approx 4.5$.
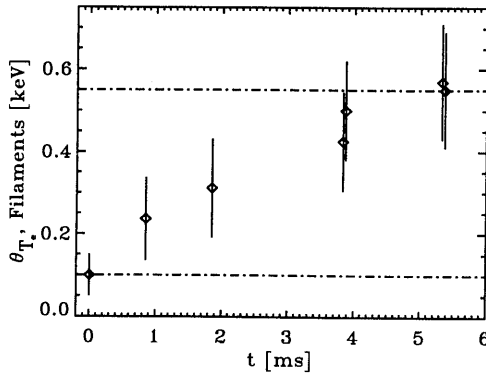
Figure 6.12: Filament amplitude expressed in Θ_{T_e} as a function of time after ECH switch-on. In the figure Θ_{T_e} for the Ohmic plasma is included. The threshold at 550 eV is obtained from the averaged Θ_{T_e} at $q_a=4.5$ in Fig. 6.9. Note that the the data point are obtained from single TS measurements. The spread is determined by multiplying the spread in Fig. 6.9 by the the squareroot of the number of discharges used in that figure. The trend is clear: it takes milliseconds before the maximum filament amplitude is reached.

6.7   Do filaments occur at $q > 1$?

So far all examples of filamented T_e profiles concern centrally heated ECH plasmas. The filaments were found in the central part of the plasma, inside the sawtooth inversion radius, where q is close to 1. The filaments are interpreted as closed flux tubes.

There is a much smaller set of observations of filaments in plasmas with inverted q-profiles, which in RTP are obtained -steady state- by application of off-axis ECH [17]. Figure 6.13 gives an example of an extreme case, where the ECH resonance was at ρ=0.6 (corresponding to z=100 mm). In this case the T_e profile as well as the p_e profile become hollow, while the n_e profile remains peaked. The plasma in this case is like a toroidal shell, with only little pressure in the interior. Note that the hollowness is mainly due to a steep T_e gradient in the region 60< |z| <80 mm. Inside the hot region, spatial variations of T_e are observed that are very similar to the filaments observed in centrally heated plasmas. Although the amplitude of the off-axis filaments is much smaller than that of the central filaments, their statistical significance is similar, thanks to the small error bars at the lower T_e.

Figure 6.13(d) shows the q profile, calculated on the basis of the measured T_e profile assuming neo-classical resistivity. Clearly, there is low magnetic shear in the region of the off-axis T_e maximum. The value of q in the low shear region is approximately q=5.5–6 but the calculation of the q-profile is not sufficiently accurate to determine whether the filaments are a resonant phenomenon or not. Off-axis filaments have been observed in a number of discharges with off-axis maxima in the T_e profile. The occurrence appears to be restricted to those cases in which these off-axis maxima show a sawtooth-instability [16, 18]. This ties q in the sawtoothing regions to simple rational values, which supports the hypothesis that filamentation is a geometrically resonant phenomenon.

In conclusion, there is a limited set of observations of filaments in T_e profiles with a pronounced off-axis maximum, obtained by application of off-axis ECH. In those cases, the value of q is certainly well above unity. These observations suggest that ECH in a region with low shear at a simple rational value of q is the condition that is favourable for filament creation.
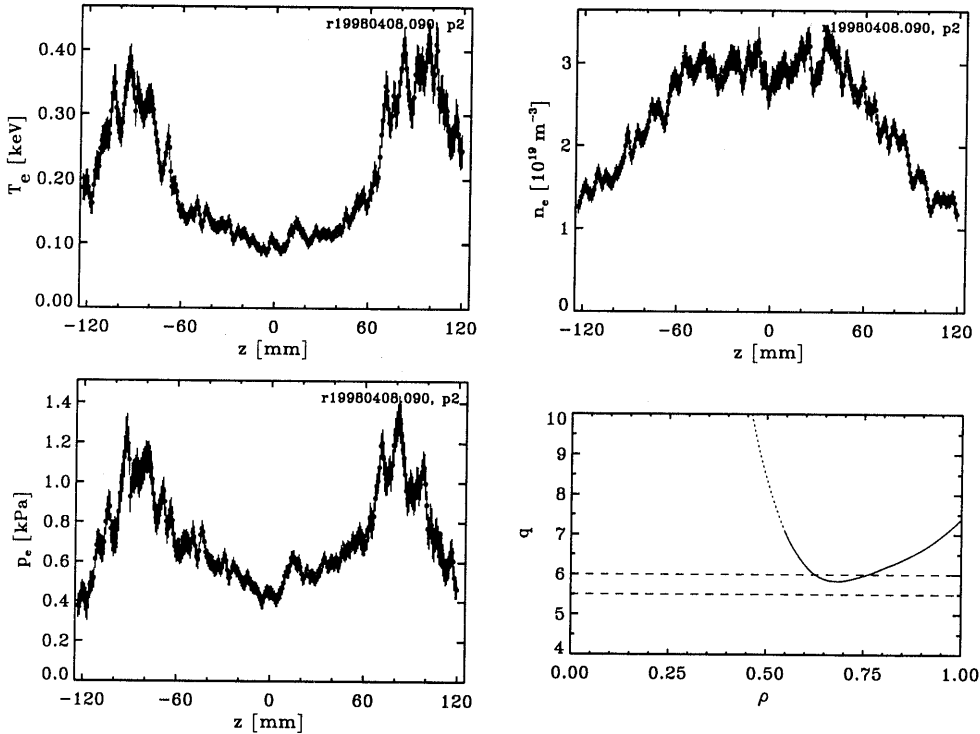
Figure 6.13: *Example of filaments in an off-axis heated plasma. The ECH deposition region is at the T_e maximum. $q_{min} > 5.5$ in this plasma, $I_p = 60\,kA$, and $B_\phi \approx 2.25\,T$.*

6.8 Are filaments ECH specific?

All filaments presented so far were observed in plasmas heated by ECH, and only in the region where the ECH was deposited. The question must be addressed whether ECH is necessary to create filaments, or whether in the examples shown thusfar the ECH only served to create favourable conditions for filaments. We first examine the T_e profiles of normal Ohmic discharges, and secondly report observations of filaments in Ohmic discharges which show a transient rise of the central temperature in response to edge cooling (the 'non-local' effect).

6.8.1 Do filaments occur in normal Ohmic discharges?

Figure 6.14 shows T_e profiles of Ohmic discharges with $q_a=5$, at three different densities. All profiles show a rich fine structure. Since the error bars are small for this T_e-range, especially for the higher densities, these structures are statistically significant. The typical size is at 5–10 mm similar to that of filaments. The typical amplitude of the structures is 100 eV, approximately constant over the profile. There is no clear density dependence. If anything, they are larger for higher density, since at low density the apparent amplitude is enhanced by the statistical error. Thus, these structures do not seem to be bound to low shear regions and do not become smaller for larger density. Their phenomenology

therefore is distinguished from that of the filaments. Moreover, as was pointed out in section 6.6, the fact that it takes 3 ms for filaments to develop after ECH is switched on, precludes the possibility that filaments were already present in the Ohmic plasma: to heat pre-existing filaments takes only hundreds of microseconds. The interpretation of the small scale structures in Ohmic profiles, and of similar structures in the T_e profiles in ECH plasmas outside the filamented region, is outside the scope of the present paper. However, it may be clear that if these structures are the fingerprint of a broken magnetic topology, this is significant for the understanding of electron heat transport in tokamaks.
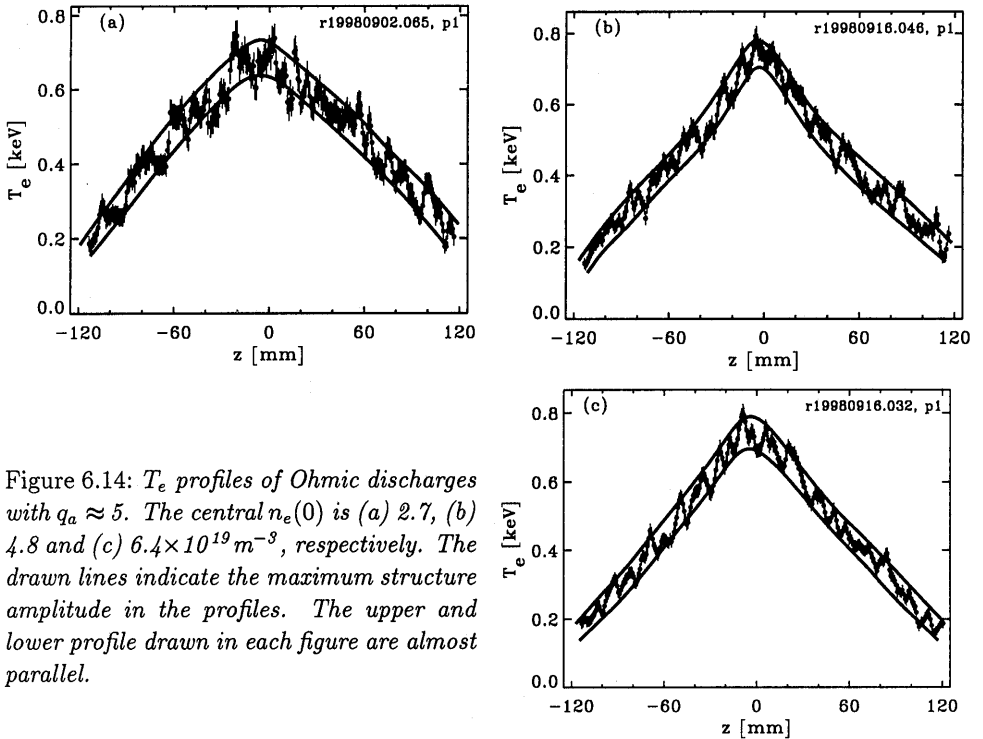
Figure 6.14: T_e *profiles of Ohmic discharges with* $q_a \approx 5$. *The central* $n_e(0)$ *is (a) 2.7, (b) 4.8 and (c) 6.4×10^{19} m^{-3}, respectively. The drawn lines indicate the maximum structure amplitude in the profiles. The upper and lower profile drawn in each figure are almost parallel.*

6.8.2   Filaments during 'non-local' heating

In many tokamaks it has been observed that an induced fast T_e drop in the outer layer of the plasma leads to a temporary rise of the central T_e [19, 20, 24]. Because of the sign difference between cause and response, and the fact that in many cases the response time is faster than can be explained on the basis of thermal diffusion, this phenomenon is often referred to as the 'non-local' effect. In RTP many experiments have been dedicated to this phenomenon, using oblique pellet injection (the pellet passes the plasma center at > 65 % of the minor radius) to induce the fast edge cooling, and techniques such as modulated ECH to probe the transport.

At 2.5< n_e <3×10^{19} m^{-3}, T_e filaments have been observed during the transient T_e rise. Figure 6.15 shows two examples. In those plasmas, no ECH was applied at all. The filament amplitude is, at 200–300 eV, somewhat smaller than in ECH plasmas, but significantly larger than that of the structures in normal Ohmic plasmas.

A detailed analysis of heat pulse propagation during the non-local effect in RTP shows that the central T_e rise is due to the formation, or strengthening, of transport barriers just outside the $q=1$ radius [21, 22]. From other studies in RTP it was concluded that electron transport barriers are tightly linked to the q-profile [23]. In this picture, the non-local effect could be the result of a subtle change of the q-profile, lowering the shear around the $q=1$ surface. According to the analysis in the previous sections, filamentation might require a region of low shear at a simple rational value of q. This condition appears to be met during the non-local T_e rise. Thus, the observation of filaments and the hypothesis that the non-local effect is due to a reduction of the shear near the $q=1$ radius are consistent.
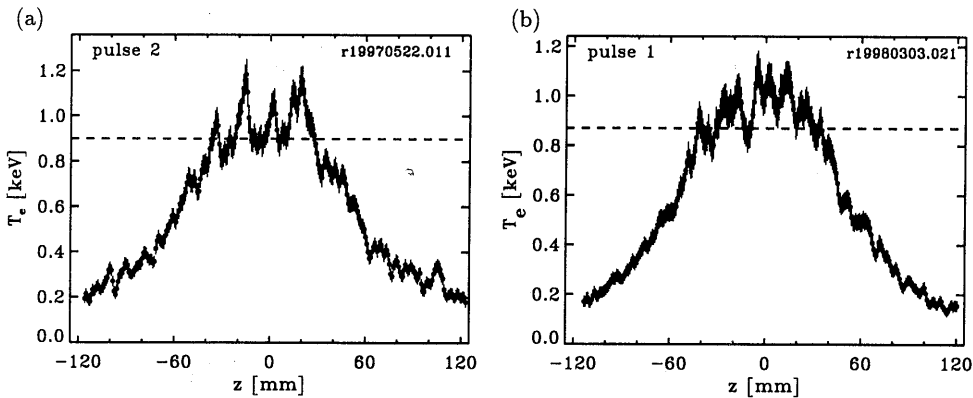
Figure 6.15: *Two examples of filaments in 'non-locally' heated plasmas.*

6.9 Filaments and sawtooth activity

In this section the effect of sawtooth collapses on filaments is presented. The double pulse feature of the TS diagnostic has been applied to measure T_e profiles just before and just after a sawtooth collapse in the same discharge. Both in the case of non-locally heated plasmas and ECH plasmas the filaments are destroyed by the sawtooth collapse. First double pulse measurements in non-locally heated plasmas will be presented.

Figure 6.16 shows two examples of non-locally heated discharges. These are the same discharges as in Fig. 6.15. The T_e rise in the plasma center can be seen in the central ECE measurements. The maximum T_e is reached a few milliseconds after the pellet is injected. Next to the rise in the central T_e, the sawtooth activity is enhanced, which is possibly caused by the peaking of the current density due to the edge cooling by the pellet. For both discharges the timing of the double pulse TS measurements is indicated in the ECE trace. Example (a) has the first pulse just after a sawtooth collapse. It shows a flat profile without filaments. The second pulse, $400\mu s$ later, and just before the next collapse, shows 3–4 filaments. Example (b) shows the reverse case. The first TS measurement is just before a sawtooth crash and the second just after. The T_e profile of the first pulse is filamented while the second is flat, and shows no filamentation.
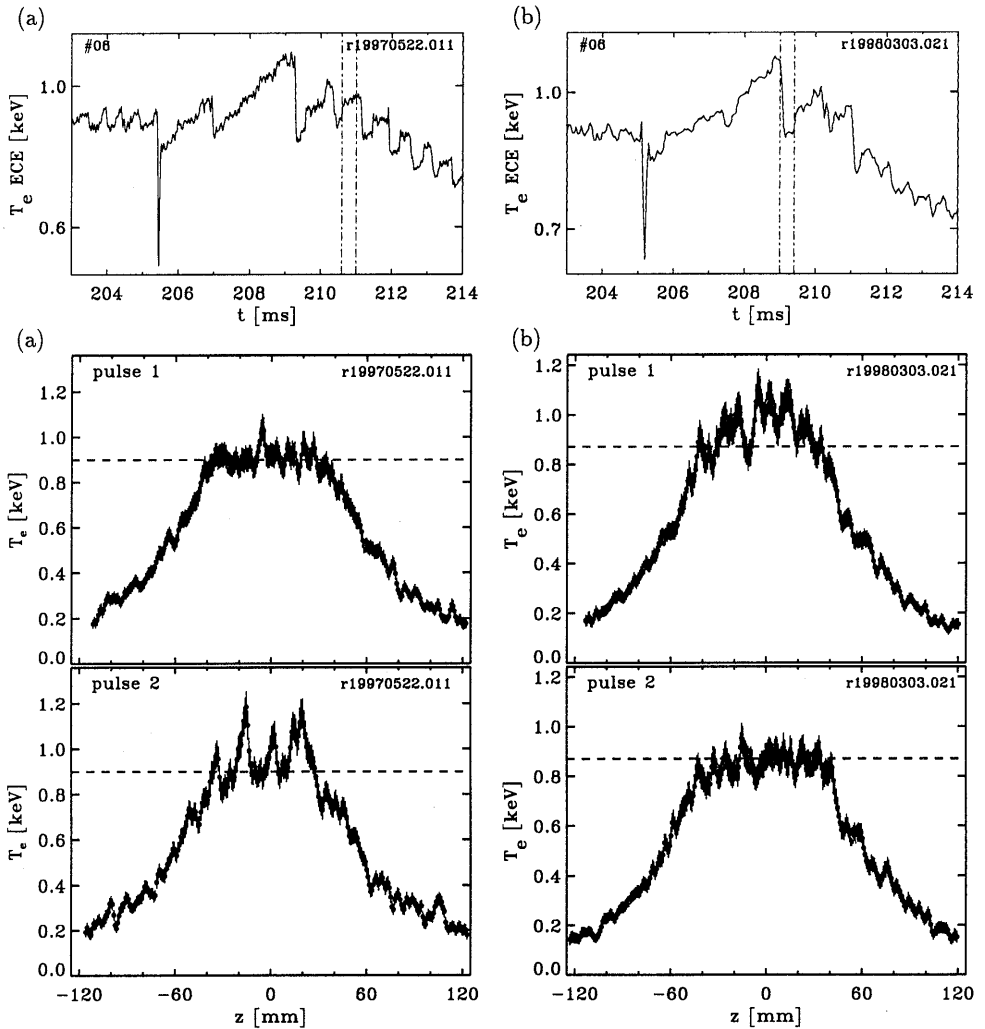
Figure 6.16: *Two examples of the effect of sawteeth on filaments in plasmas with non-local heating. The central ECE channels show that $T_e(0)$ rises after the pellet is injected. The moment of pellet injection is at (a) 205.4 ms and (b) 205.2 ms at the sudden dip in the ECE signal. In (a) the first pulse is just after a sawtooth collapse and shows a flat profile. The second profile, 400 μs later, shows filamentation of the core. In (b) the first pulse is just before a crash and is filamented, while the second profile just after the crash is flat.*

Thus, filaments observed during the non-locally induced T_e rise, are destroyed by a sawtooth crash. In ECH plasmas sawteeth also have a destructive effect on filaments. First, single pulse measurements are presented that show the evolution of the T_e profile during a sawtooth crash, and next double pulse TS measurements are presented.

Figure 6.17 shows the time trace of a central ECE channel of a discharge with q_a=5.8 and $n_e(0)$=1.5 × 10^{19}m^{-3}. Central ECH is applied, and is launched under an angle of about +20° with respect to the toroidal field B_ϕ. This drives a non-inductive current of

~10 kA as a part of a total plasma current of 60 kA. The central ECCD (electron cyclotron current drive) peaks up the current density profile and enhances the sawtooth activity. In three well reproducing discharges single pulse TS is fired in different stages of the sawtooth cycle, as indicated in Fig. 6.17. The figure also shows the three T_e profiles. The profile just before the sawtooth crash shows central filaments with an amplitude of 500–700 eV. During the crash a T_e profile is measured which shows the spectacular displacement of the hot core. The profile after the crash is flatter, and the amplitude of the structures in the center is lower than those in the profile before the crash. Outside the inversion radius the profiles before and after the crash are very similar.
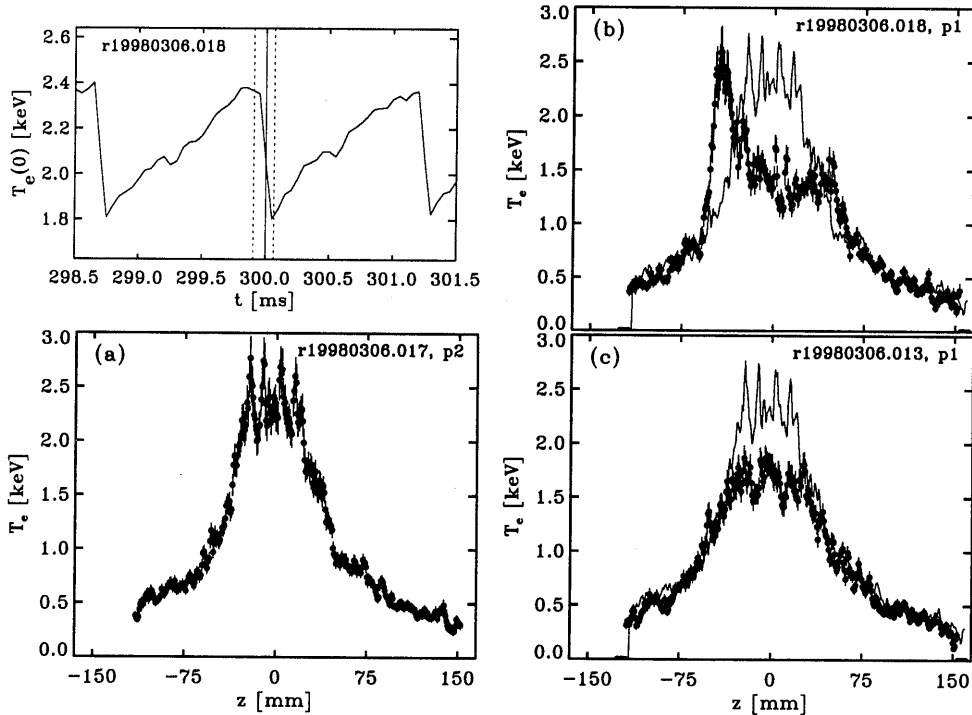
Figure 6.17: *TS profiles in different stages of a sawtooth cycle in well reproducing plasmas with ECCD. The timing of the pulses in relation to the sawtooth phase is indicated in the central ECE time trace (top left). (a) Just before the sawtooth crash, with high central T_e and a filamented core. (b) Profile inside the sawtooth crash, showing the displacement of the hot core. (c) After the sawtooth crash, showing the flattened top of the profile. The profile of (a) is overplotted in (b) and (c).*

Figure 6.18 shows two examples of double pulse measurements in a sawtoothing plasma. The time resolution of the ECE in this experiment is higher than in the examples of Figs. 6.16 and 6.17 (6 μs instead of 50 μs). The central ECE trace shows a large m/n=1/1 precursor. The first example shows the footprint of the large odd mode in the first profile. The high T_e region is filamented. The second profile is after a sawtooth collapse and shows no filamentation. The second example shows the reverse case. The first profile is just after a collapse and is flat. The second profile is filamented again.
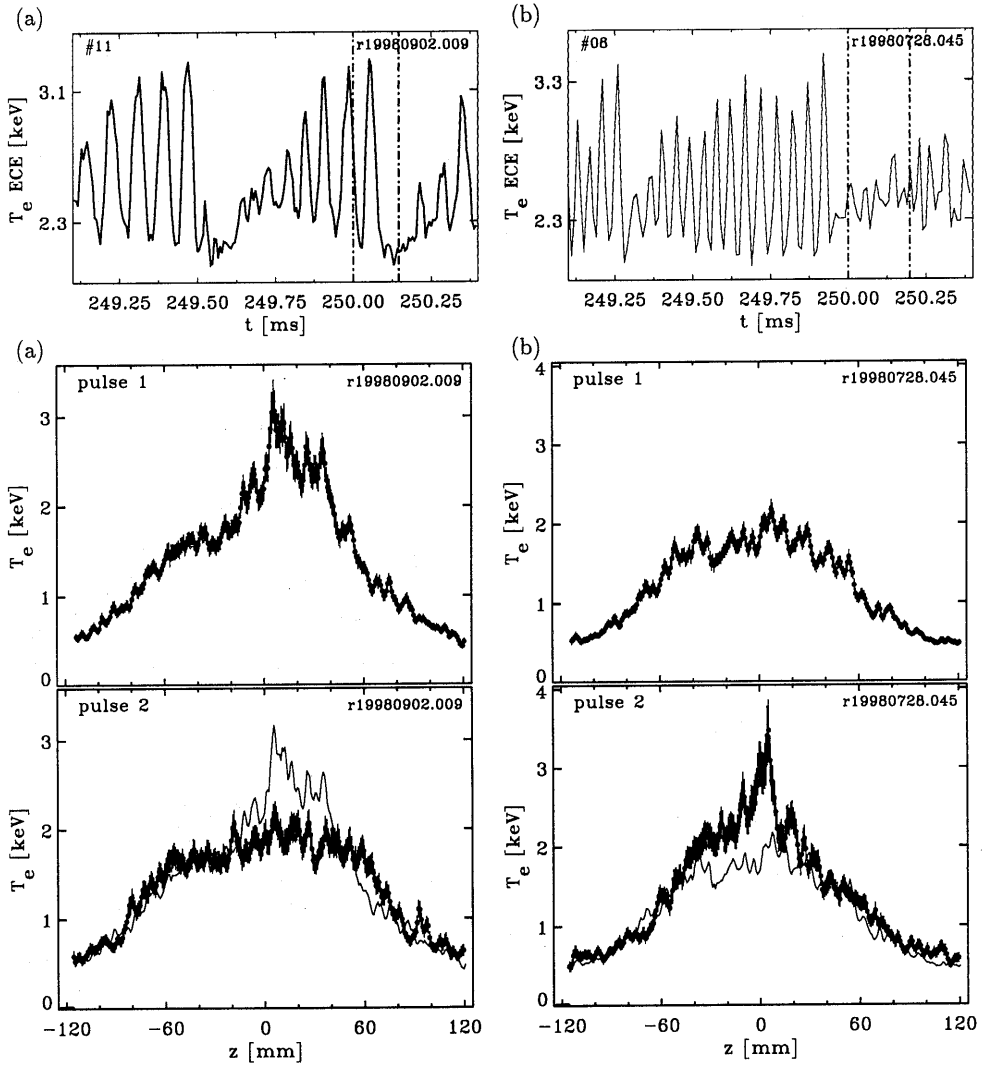
Figure 6.18: *Two examples of the effect of sawteeth on filaments. Both show a large m/n=1/1 sawtooth precursor on the central ECE channel. In (a) the double pulse TS measurements are just before and just after the crash, as is indicated with the vertical lines in the ECE time trace. The profile before the crash shows the footprint of the m/n=1/1 mode and filaments. The second profile is flattened. In (b) both pulses are after the crash. The first profile is flat, and the second 200μs later is filamented again. (a): $q_a=3.1$, $n_e(0)=2.7\times10^{19}\,m^{-3}$, (b): $q_a=4.6$, $n_e(0)=2.3\times10^{19}\,m^{-3}$.*

In section 6.6 is was shown that it takes ~3 ms for the filaments to develop after ECH is switched on. This long time scale was interpreted as the time needed to achieve the conditions in which the filaments can grow. In the case of the sawtooth crash, the conditions were already favourable for filamentation before the crash, and this is still the case after the crash. Therefore, the few hundred microseconds within which the filaments

reappear after a sawtooth crash may be interpreted as the energy confinement time of a filament. This is consistent with the observation that filaments persist for a few hundred microseconds after ECH is switched off.

6.10   Filaments and sawtooth precursors

In this section will be shown that the occurrence of filaments is independent on the occurrence of sawtooth precursor. Figure 6.19 shows an example of a sawtoothing discharge. The central ECE channels show the m=1 character of the mode. The central channel is more or less quiet, and does not show the mode, while the neigbouring channels show the mode in counter phase. A double pulse TS measurement has been performed, and the two pulses both fall in the rising phase of a sawtooth. Both T_e profiles of the TS measurement show the footprint of the odd mode. The first pulse shows flat T_e regions symmetric to the left and to the right of the center, and the second pulse shows a flat region in the left wing of the profile. A large filament is visible in the profile of the second pulse.

Another example shows a TS measurement in a sawtooth quiet phase, see Fig. 6.20. The central ECE channels show that in this example sawteeth are less frequent, and moreover, the amplitude of the m=n=1 precursor is lower. The TS T_e profile is taken at a time that no mode activity is visible in the ECE measurement. Still, this T_e profile is filamented. This contradicts the assumption in [13] that filaments are part of a larger, single m=n=1 sawtooth precursor.

The amplitude of the m=n=1 mode activity depends on the exact deposition radius of the ECH. Figure 6.21(a) shows the maximum amplitude of the sawtooth precursor per discharge as a function of deposition radius. It shows that the mode activity is the largest when the ECH deposition is located at the magnetic axis of the plasma, i.e. at $\rho=0$. (ρ is the normalised minor radius). The $q=1$ surface is located at $\rho=0.3$, as determined from the position of the sawtooth inversion radius measured by ECE. The discharges presented in Figs. 6.19 and 6.20 are marked in the figure with their RTP shot number 56 and 42 respectively. Note that the m=1 amplitude indicated in the figure for shot 42 is not the amplitude at the time of the TS measurement.

The individual filament quantifier for each of the discharges in plotted in Fig. 6.21(b). The filled circles indicate TS measurements that are taken during the m=n=1 activity, like shot 56, and the open circles indicate TS measurements taken in an MHD quiet phase, like shot 42. The figure shows no dependence of the filaments on the MHD activity.
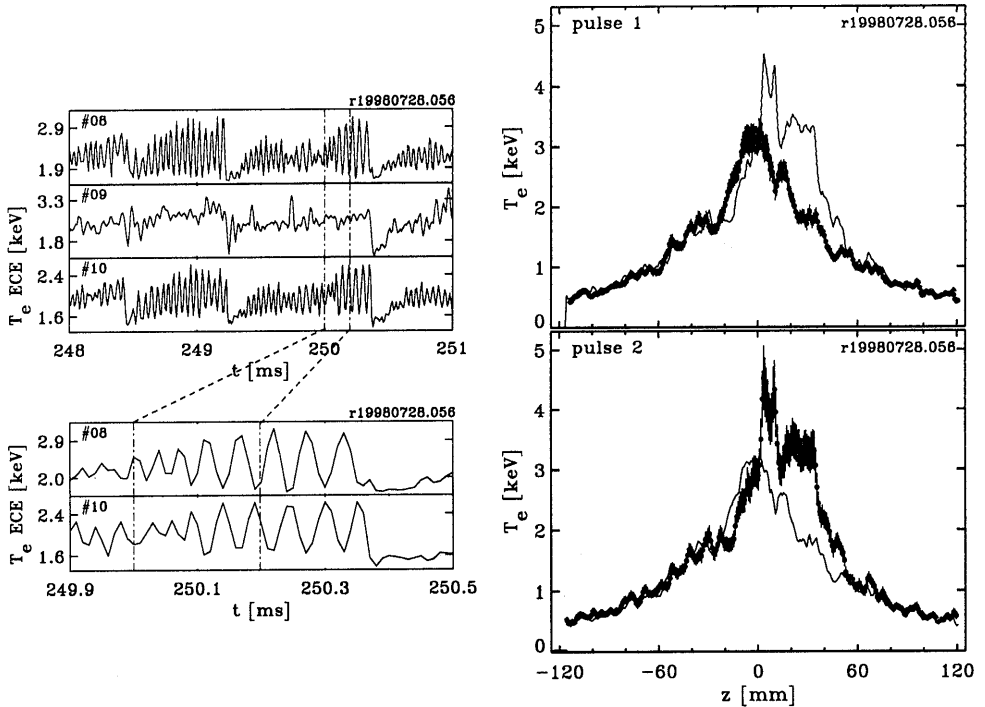
Figure 6.19: *ECE channels showing sawteeth with large m/n=1/1 precursors. ECE channel #9 lies on the magnetic axis, channels #8 and #10 are in counter phase. The first profile shows the footprint of the m/n=1/1 island on both sides of the profile. The second pulse shows the footprint on the left side of the profile and a hot filament in the high T_e part of the profile.*
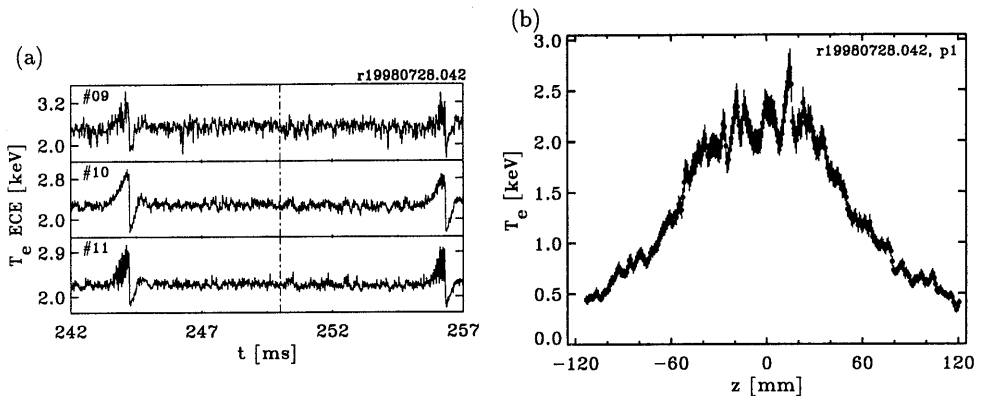
Figure 6.20: *The central ECE channels show that at the time of the TS pulse, no m/n=1/1 activity is present. Still the TS T_e profile shows filaments. The ECH deposition is just inside the sawtooth inversion radius.*

Figure 6.21: *a) Amplitude of the m/n=1/1 sawtooth precursor as a function of deposition radius ρ_{dep}. Each dot represents one discharge. Towards the q=1 surface at $\rho=0.3$ the amplitude of the m/n=1/1 mode decreases. (b) Θ_{T_e} as a function of deposition radius. Θ_{T_e} is obtained from the two pulses of each discharge. The filled circles indicate TS measurements that are taken during the m=n=1 activity, like shot 56, and the open circles indicate TS measurements taken in an MHD quiet phase, like shot 42.*
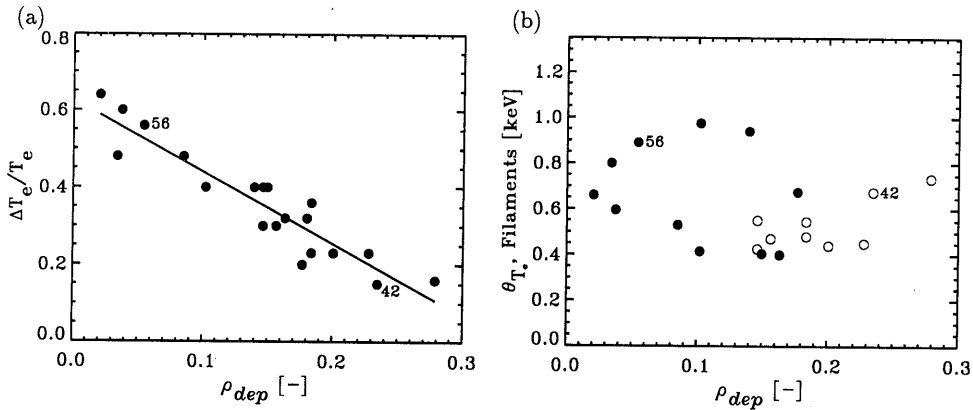
6.11 Summary and discussion

In summary, we have presented experimental data showing plasma filamentation in RTP. The filaments are only resolved by the high resolution Thomson scattering diagnostic, and appear as multiple peaks in the T_e and p_e profiles, while the spatial structures in the n_e profile have a much smaller amplitude. It was shown that the filaments are not diagnostic artefacts, because a) their amplitude and spectrum are well above the noise level, and b) they show a dynamic behaviour that identifies them as plasma physical phenomena: they are wiped out in a sawtooth crash, and they take several milliseconds to develop after switching on ECH. The filaments are interpreted as closed flux tubes, with an energy confinement time of several hundreds of microseconds, and a life time of at least that. They are resonant structures, found mostly in centrally heated plasmas inside the q=1 surface, in which case they probably have an m=n=1 mode structure. Also higher mode numbers are possible. e.g. m/n=7/8. However, filamentation of the off-axis maximum of the T_e profile has been observed in plasmas with a hollow T_e profile, induced by off-axis ECH. It is inferred that very low or vanishing magnetic shear is a required condition for the occurrence of filamentation. The majority of observations of filamentation have been done in regions that were heated by ECH, but in a few instances filamentation was also observed during the so-called non-local heating effect, when no additional heating was applied.

The topology of the filaments is a subject that needs further study. In [13] T_e fluctuations measured with high resolution ECE, were interpreted as the result of a oddly shaped magnetic island, which was then equated to the sawtooth precursor. It was suggested that these observations might concern the same phenomenon as the filamentation in RTP. The evidence at RTP contradicts this interpretation. The double pulse Thomson scattering measurements do not allow the construction of a tomogram of the central T_e, but by mak-

ing different cuts through the center, either by shifting the plasma or by using the natural plasma rotation, it was shown that the filaments are separate entities rather than a single magnetic island. Moreover, it was shown that the filaments are a phenomenon that is distinguished from the sawtooth precursor, as the filament amplitude is independent of the precursor amplitude. No in-depth analysis of such an ensemble of flux tubes has been ·carried out. There is no MHD equilibrium or stability analysis available.

There is, however, theoretical work showing the possibility of so-called 'positive is-lands'. Whereas in regions with positive shear the O-point of a magnetic island is as-sociated with a reduction in the current density, with low or negative shear flux tubes can form around current concentrations [25, 26]. In the hot filaments, it is expected that the current density is enhanced with respect to the average. The perturbation could be quite large. For a filament amplitude of 25 % of T_e, a local enhancement of the current density of up to 40 % may be expected. At $q=1$ this corresponds to an additional current density of 2 MA/m^2 in RTP. The total extra current in a filament of 5 mm radius is then up to 150 A. Thus, in a region with low magnetic shear it is possible to have regions with enhanced current density (current filaments) which are the O-points of magnetic islands. Inside the magnetic islands, the contribution of magnetic perturbations to the electron heat transport is absent, so that low electron diffusivity may be expected (see also below). Thus, in the low shear region, the occurrence of a flux tube, the high T_e inside it and the enhanced current density form a consistent set. The interaction of multiple filaments and the ensuing dynamics is an interesting issue, which has not been addressed.

To investigate the power balance in a filament, first the input power must be estimated. For a typical filament in the center of an ECH heated plasma, the Ohmic power density is estimated at $p_\Omega \approx 1$ MW/m^3 (taking $T_e=$ 2keV, $j = 7$ MA/m^2, and Spitzer resistivity with $Z_{eff}=2$). This results in a total Ohmic power $P_\Omega < 350$ W in a filament with 5 mm radius. It is noted that for the Ohmic filaments in the case of oblique pellet injection, the lower value of T_e brings the Ohmic power in the filament up to 1 kW.

The ECH power is more difficult to estimate, since the filaments move in and out of the heating zone. A conservative estimate is obtained by assuming that the ECH power is evenly distributed over the region inside the $q=1$ radius, and that a filament gets a fraction of the power in proportion to its relative cross section. Thus, a filament with 5 mm radius inside a $q=1$ region with a radius of 40 mm, sees an average ECH power density of $p_{fil, ECH} = 20$ MW/m^3, resulting in a total absorbed power in the filament of $P_{fil, ECH} = 5$ kW.

In the absence of any more sophisticated model, we only compute the energy con-finement time and the average electron thermal conductivity of a filament in cylindrical geometry. Convection or time dependent terms are neglected in this analysis. For a typical filament in a centrally heated plasma (5 mm radius, amplitude 600 eV, $n_e=2.5\times10^{19}$m^{-3} $P_{fil, ECH} = 5$ kW), assuming a uniform power density in the filament and a parabolic T_e profile we find $\chi_{fil, PB} = 0.04$ m^2/s. This value is an order of magnitude lower than the values normally found for the central region in RTP, which ties in with the fact that inside a magnetic island the magnetic topology is 'good'.

The relevant energy confinement time is associated with the amplitude of the filament, $\tau_{E,fil}=\int \frac{3}{2} n_e k(T_e - T_{e,0}) \, dV$, where $T_{e,0}$ is the electron temperature at the foot of the filament, and the integral is taken over the volume of the filament. For the typical ECH filament, we find $\tau_{E,fil}= 120 \,\mu$s. This value compares well with the observation

that filaments reappear within 250 microseconds after a sawtooth crash. The resistive skin time of a filament, estimated at $\tau_{R,fil} = 200\,\mu s$, is not much longer than the energy confinement time, thanks to the low thermal diffusivity. In particular, $\tau_{R,fil}$ is sufficiently close to $\tau_{E,fil}$ to allow the current density to follow the temperature rise in a filament. Thus, it is conceivable that filaments are the result of a thermal instability.

We compare the experimental value of the diffusivity $\chi_{fil,PB}$ to the neo-classical diffusivity χ_{neo}. For the typical ECH filament conditions, the plasma is well within the banana regime ($\nu^* \ll 1$) for $\rho > 0.01$. In the filament region, i.e. $\rho = 0-0.3$, we find $\chi_{neo} = 0.02-0.03\,\mathrm{m}^2/\mathrm{s}$. The width of the banana orbits is typically several millimeters, due to the low value of the poloidal field in the proximity of the plasma centre. Hence, the experimental value $\chi_{fil,PB}$ is quite close to the neo-classical estimate, exceeding it by only a factor up to 2. A point of consideration is the fact that the filament diameter is only a few banana widths. This may have an effect on the applicability of the neo-classical transport coefficient, but a treatment of this issue is outside the scope of this thesis.

It is interesting to compare the typical width of the filaments with fundamental length scales in the plasma. First, we note the filaments are 1-2 orders of magnitude larger than the Debije length and the electron Larmor radius. The filaments are only several times larger than the width of electron banana orbits (1-5 mm, depending on the distance to the axis), the ion Larmor radius (1 mm) and the electron inertial skin depth (1 mm). Thus, there appear to be no fundamental problems with the size of the filaments, but the observed filaments are close to the smallest size that can be expected on theoretical grounds.

Finally, the question is addressed whether the occurrence of filamentation has an impact on the global energy confinement of the plasma. First, it is observed that the filamented volume is so small that it contributes little to the total stored energy. Second, the global energy confinement of RTP discharges with central ECH that show filamentation is in good agreement with the ITER89 scaling. Hence, there is no indication that filamentation is associated with poor confinement. Third, in no way are there indications that after the switch-on of ECH the confinement degrades as a result of the filament formation. The usual power degradation sets in much faster than that. Thus, there is no sign that filament formation has a detrimental effect on global energy confinement. The filamented region itself is bounded by steep gradients, thanks to which the net confinement in this region is good. This is particularly clear in the case of the filaments which appear in an Ohmic discharge during the non-local heating effect. In this case the insulation of the central region can be significantly better than is the case in a normal Ohmic discharge. The filamented region itself obviously cannot be described by a 1-dimensional transport model.

References

[1] B.V. Chirikov, Phys. Rep. **52** (1979) 265.

[2] P.C. de Vries, *et al.*, Plasma Phys. and Contr. Fusion, **39**, 1997 439-451.

[3] P.C. de Vries, *et al.*, Nucl. Fusion, **37** (1997) 1641-1646.

[4] T. Yamauchi, *et al.*, Phys. letters A, **223** (1996) 179-185.

[5] M.F.F. Nave, *et al.*, Nucl. Fusion **32** (1992) 825.

[6] M.N.A. Beurskens *et al.*, *"Double pulse multiposition Thomson scattering and dynamics of small scale T_e and n_e profiles in RTP"*, submitted to Rev. sci. Instrum.

[7] S. Günter, *et al.*, Nucl. Fusion **38** (1998) 1431–1434

[8] X.L. Zou, *et al.*, Phys Rev. Letters **75** (1995) 1090.

[9] L. Colas, *et al.*, Nucl. Fusion, **38** (1998) 903–918.

[10] C.J. Barth *et al.*, Rev. sci. Instrum. **68** (9), (1997) 3380-3392.

[11] N.J. Lopes Cardozo, *et al.*, Phys Rev. Letters **73** (1994) 256-259.

[12] N.J. Lopes Cardozo, *et al.*, Plasma Phys. Control. Fusion **36**, (1994) B133-B142.

[13] G. Cima, *et al.*, Plasma Phys. Control. Fusion **40**, (1998) 1149-1158.

[14] M.N.A. Beurskens, *et al.*, 'Error analysis of RTP Thomson scattering data', accepted for publication in Rev. Sci. Instrum.

[15] A.J.H. Donné, Plasma Phys. Reports **20** (1994) 192

[16] N.J. Lopes Cardozo, *et al.*, Plasma Phys. Control. Fusion **39**, suppl. 12B, (1997) B303-B316.

[17] G.M.D. Hogeweij, *et al.*, Phys Rev. Letters **76** (1996) 632–635.

[18] M.R. de Baar, *et al.*, Phys Rev. Letters **78** (1997) 4573.

[19] K.W. Gentle,*et al.*, Phys Rev. Letters **74** (1995) 3620.

[20] P. Mantica, *et al.*, Proc. 24th EPS Conf. on Controlled Fusion and Plasma Physics, (Berchtesgaden 1997) Part IV, p 1853-1856.

[21] P. Mantica, *et al.*, submitted to Phys Rev. Letters.

[22] P. Mantica, *et al.*, Proc. 25th EPS Conf. on Controlled Fusion and Plasma Physics, (Prague 1998).

[23] G.M.D. Hogeweij, *et al.*, accepted for publication in Nucl. Fusion.

[24] J.D. Callen and M.W. Kissick. Plasma Phys. Control. Fusion **39** (1997) B173–B188.

[25] S.V. Mirnov, Plasma Phys. Reports **24** 1998, 813–817.

[26] M. de Rover, 'Chaos in magnetized plasmas', thesis, university of technology, Eindhoven (1996), ISBN 90-386-0018-6.

Chapter 7

Evaluation & Discussion

This thesis contains a study of plasma filamentation in the RTP tokamak, and the diagnostic development required for this study. The main work is described in chapters 4, 5, and 6. Chapter 4 and 5 describe the design, test and error analysis of the new double pulse high resolution Thomson scattering (TS) diagnostic. Chapter 6 describes a study of the nature and the dynamics of plasma filamentation.

In this evaluation chapter, first the instrumental properties of the double pulse TS diagnostic will be summarised. Then the findings of the filament study will be listed. Furthermore, the question is addressed whether the research goals have been achieved. Finally, suggestions for new experiments and new diagnostic development are discussed.

7.1 Double pulse Thomson scattering

A double pulse multiposition Thomson scattering diagnostic has been designed, constructed, described and tested. Below the main specifications of the diagnostic are listed.

- It measures two profiles of T_e and n_e in a vertical chord with a range of z=[-125, 165] mm. A ruby laser is fired twice and the scattered light is recorded by a double detection system containing 2 Intensified-CCD (ICCD) cameras (Chapter 4).
- The spatial resolution of the measurements is 3 mm Full Width Half Maximum (FWHM) over the full z-range. This is 2 % of the RTP minor radius (Chapter 4).
- The time separation Δt_{TS} between the two measurements can be tuned in the range Δt_{TS}=[20, 800] μs (Chapter 4).
- The relative statistical error of a single measurement is 3–5 % of T_e and 2–4 % of n_e. This is for the full T_e-range of T_e= [50 eV, 6 keV], at $n_e = 5 \times 10^{19} \text{m}^{-3}$ (Chapter 5).
- The relative systematic error in a single measurement due to the instrument profile may be larger than the relative statistical error. However, this results in an offset on the T_e and n_e profiles, and thus does not influence the study of small scale structures (Chapter 5).
- The deviations between measurements of the same laser pulse with both ICCD cameras are below the amplitude of their statistical error. As a consequence, differences in the profiles of T_e and n_e of double pulse measurements are significant when they are larger then the statistical error (Chapter 4).

The diagnostic has been operational most of the time since June, 1996 until the end of operation of RTP in September 1998. Although the aim was to study the dynamics of

filaments, the diagnostic has been used for many other research topics. A list of publications is given in chapter 1. The most important are: the study of electron heat transport barriers; off-axis sawtooth activity; profiles during pellet ablation; profiles during major and minor disruptions; and the measurement of current density profiles with tangential TS.

7.2   Filaments

The research aim of this thesis was to study the topology, the dynamics and the occurrence of filaments with extended experiments using the double pulse TS diagnostic. Observations and conclusions from these experiments are:

- Filament are a statistically significant plasma physical phenomenon and not a diagnostic artefact.
- Filament are most likely separate flux tubes rather than part of a single magnetic island. This is determined in an experiment where different cuts through the plasma center are made. Single peaks are found in all cross-sections. Furthermore, it is shown that the filament amplitude is independent of the amplitude of a large m=1 island present as a sawtooth precursor.
- The filaments show a weak dependence on q_a.
- The scaling of the filament amplitude with density as $n_e^{-1.5}$ is close to the density scaling in neo-classical confinement.
- Inside a filament the experimentally found value for the heat diffusivity is close to the neo-classical value.
- It is inferred that very low or vanishing magnetic shear is a required condition for the occurrence of filamentation. Filaments are mostly observed in the center of discharges with central ECH. However, they have also been observed in off-axis heated discharges in the off-axis maximum of the T_e profile. In both cases the filament region has low shear.
- Filaments are not ECH specific. They were also observed during the so-called non-local heating effect where a central T_e rise is observed after cooling of the edge. No ECH was applied in these plasmas.
- Filaments are not pre-existing in the Ohmic phase before the ECH is switched on. The time scale for filament creation is $\sim 3\,\mathrm{ms}$.
- Filaments are destroyed by a sawtooth crash.

7.3   Have the goals been achieved?

The questions on filaments addressed in the introduction of this thesis have been answered. The topology of the filaments has been revealed, and information of the dynamics is obtained. The occurrence of filaments in various plasma conditions has been shown.

However, two pulses yields poor time resolution. Furthermore, it is found that the requirements on spatial resolution and accuracy have only just been met. It is not clear whether the smallest scale of filaments observed is limited by the spatial resolution of the diagnostic, i.e. by its instrument profile, or that 5 mm indeed is the smallest scale structure in the plasma.

In order to really reveal the topology of the filaments, it would be ideal to be able to measure a 2-dimensional poloidal cross section with a spatial resolution of 2 mm and a relative accuracy better than 5 %.

It is possible to make a quasi-tomographic reconstruction by means of TS, assuming that the plasma is a rigid rotator. For a TS diagnostic at RTP this would require a temporal resolution of $\sim 5\,\mu s$. In section 7.4.2 the diagnostic possibilities are discussed.

7.4 New diagnostic development

7.4.1 Next step: move to Textor

It should be noted that the research program at RTP ended in September, 1998. New experiments on filamentation at RTP are therefore not possible. The research program on tokamak physics is continued at the Textor tokamak in Jülich, Germany. This tokamak is in linear dimensions ~ 3 times larger than RTP. It can be assumed that filaments scale with the size of the machine. Therefore, at Textor, filaments are expected to have a typical width of 1.5–3 cm.

A new double pulse Thomson scattering diagnostic will be installed with a relative spatial resolution better than the resolution of the RTP system: <7.5 mm (1.5 % of the Textor minor radius), which is sufficient to resolve possible filaments. The measurement accuracy will be equal to the accuracy of the RTP system.

Furthermore the Textor tokamak will be equipped with a 1 MW gyrotron for ECH heating and later with an additionally 1 MW Free Electron Maser (FEM) that produces electron cyclotron radiation with a tunable frequency. That way the deposition radius of the ECH can be changed without changing the magnetic field of the plasma.

At Textor the study of filaments will be proceeded. Although filament-like structures have been observed with ECE-I in the TEXT-tokamak in the USA [4], high resolution measurements of filaments in Textor, would be a good indication of their general occurrence.

All the experiments done on filaments in RTP should be repeated in Textor. New experiment should include a more extensive parameter scan with a broader n_e and q_a range, and an ECH-power scan. Further, the time scale of filament 'creation' after ECH switch-on requires further study.

7.4.2 Further development

As was discussed in section 7.3 a higher time resolution of the Thomson scattering would enable a quasi-tomographic reconstruction of the poloidal cross section, which resolves a 2-dimensional picture of filaments. This requires the assumption that the plasma is a rigid rotator. The plasma rotation at Textor is a factor 5–10 slower than at RTP. The temporal resolution of the measurement of small scale structures therefore can be lower than at RTP. Above was suggested that a repetition rate of $5\,\mu s$ was required for RTP to make a good quasi-tomographic reconstruction. At Textor a repetition rate of $50\,\mu s$ would be sufficient.

A 16 channels ECE-imaging diagnostic, similar to the system at TEXT, USA, will be installed at Textor. The requirement on the temporal resolution of $50\mu s$ are achieved

with this diagnostic. The spatial resolution. i.e. 1 cm FWHM, is also sufficient to resolve Textor filaments (1.5–3 cm). However, the channel spacing will be too large. To resolve filaments the system should be upgraded to more channels with less inter-spacing.

To obtain higher spatial resolution measurements of filaments, Thomson scattering is the only option. Below a discussion is given on the possibilities of a multi pulse Thomson scattering diagnostic with a temporal resolution of 50μs.

Multi pulse Thomson scattering

Multi pulse means multi laser pulses and multi detection of those laser pulses. Both require an upgrade of the current double pulse system.

Laser

The RTP Thomson scattering laser is a 25 J ruby laser. It has one oscillator and three amplifier stages. In double pulse mode, the laser can yield 2 pulses of 12.5 J and 40 ns FWHM each by double Q-switching during one period of the oscillator flash lamp.

What are currently the possibilities for a multi pulse system? Commercially available are:

- A 4 Hz ruby with $\sim$ 5 J and $\sim$15 ns FWHM per pulse.
- A 100 Hz Nd:YAG laser with $\sim$ 0.5 J and $\sim$15 ns FWHM per pulse.

Clearly, the repetition rate is not high enough to achieve a temporal resolution of 50 μs required to construct a quasi 2-dimensional T_e profile. Stockdale presented a system for DIII-D in which multiple Nd:YAG lasers are operated in 'burst'-mode, i.e. are fired in rapid succession [1]. In this system a repetition rate of $\leq$10 kHz has been achieved. This could also be performed with ruby lasers in order to achieve higher laser energies.

A different way to achieve a high repetition, high laser energy system has been presented by Kantor and Kouprienko, [2, 3]. They have constructed a multi pass intra cavity system in which the plasma volume is part of the laser cavity. Multiple laser pulses have been obtained by multiple Q-switching of the laser during one period of the oscillator flash lamp. The high laser energies stem from the multiple passing of the laser beam through the plasma. With this system repetition rates of up to 15 kHz, and laser energies as high as 100 J in a 1μs FWHM pulse have been achieved.

Thus, high repetition laser-systems are feasible. Nd:YAG lasers in burst-mode have been tested. However these provide only low laser energy. Higher laser energies can be achieved with a battery of ruby lasers in burst-mode. A further study of multi Q-switching lasers is recommended. These give high repetition rate and high laser energy.

Detector

The detection system of a fast multi pulse TS diagnostic must have a read-out time below the laser pulse separation. Only CCD-based systems yield the required spatial resolution. The dynamic range of the applied CCD's should be at least 14 bit. However, CCD-systems with high enough dynamic range feature a typical read-out time in the order of 1 s, i.e. too slow for the fast dynamics in the plasma.

CCD systems that do not require full read-out must be considered. Two options that require further study are 'sweep-cameras' and 'masked-cameras'. Both are CCD-based camera systems.

In a sweep-camera the electron beam from the photocathode is swept from one part of the CCD-chip to another part. This requires large CCD-chips. The 'sweeping' of the image to different areas on the CCD-chip can be done very fast ($\leq 1\mu s$). When the CCD is filled with multiple images, it must be read out completely, which is slow and takes several seconds. The number of pulses that can be recorded is limited to the ratio between the size of the CCD-chip and the size of the image. Furthermore, the sweeping-accuracy can be a limiting factor.

The masked-cameras are also CCD-based. Part of the chip is covered and is used as storage of already recorded images. Again the number of pulses that can be recorded is restricted to the ratio between the size of the CCD-chip and the size of the image. The temporal resolution is limited by the speed at which an image can be shifted from the detection region to the masked area of the CCD. For a 14 bit CCD-chip this is estimated to be ≥ 1 ms, i.e. not fast enough to reconstruct a quasi-tomographic picture of filaments.

In conclusion, a multi pulse high resolution TS diagnostic with a temporal resolution of $\sim 50\mu s$ is feasible. Both lasers in 'burst-mode' and multi pass intra cavity systems belong to the options. To achieve high spatial resolution high repetition detection, fast sweep-cameras seem to be an important candidate.

References

[1] R.E. Stockdale, *et al.*, Rev. Sci. Instrum. **66**, 490 (1995)

[2] M. Yu. Kantor and D.V. Kuprienko, Tech. Phys. Lett. **23** (1997) 321

[3] M. Yu. Kantor and D.V. Kuprienko, Rev. Sci. Instrum. **70** 1999, 1–3

[4] G. Cima, *et al.*, Plasma Phys. Control. Fusion **40**, (1998) 1149-1158.

Dankwoord

Ik neem bij deze graag de gelegenheid om een aantal mensen te bedanken. Allereerst mijn eerste promotor en begeleider Niek Lopes Cardozo. Ik heb ontzettend veel van je geleerd. Altijd kritisch en haarscherp commentaar, en in de eindsprint een geweldige steun in de rug. Daarnaast natuurlijk mijn copromotor Rolie Barth. Van jou heb ik enorm veel geleerd over optica en fysische instrumentatie. Ik kon altijd bij je terecht. Je zeer nauwgezette wijze waarop je mijn werk volgde en bekritiseerde heeft een grote bijdrage geleverd aan de tot standkoming van dit proefschrift. Je bent een kei! Dan Chris Schüller, mijn tweede promotor, voor de goede commentaren op mijn proefschrift. Het is jammer dat ik niet méér van je kennis gebruik heb kunnen maken, want die discussies die we gevoerd hebben waren zeer inspirerend. Vervolgens dank ik de leden van de leescommissie, Daan Schram en Marnix van de Wiel, voor de kritische kijk op mijn proefschrift.

En dan nu de vele collega's zonder wie ik het zeker niet had gered: Marco waar lief en leed mee gedeeld, niet op de laatste plaats het schrijversleed met een innovatie-coëfficiënt van 148. Hennie de ongelooflijke manus van alles, niet waar? Chen Chi en Folbert voor de start van mijn Thomson kennis. De gehele transportfysica groep voor het gebak en de discussies, en bovenal de prettige sfeer: Arnold (lompe Nol), Frank (Best ver dat Kiev), Attila (vijf gulden), Dik (bakje thee?), Ralph (hee baby), Eric A. (Goeiesmaandags. En-nuh, is de lay-out wel in orde?), Oktay (iedereen zou een auto moeten hebben), Jos (Als jij dat leuk vindt moet je dat vooral doen), Francisco (disruption man).
Het RTP-team: Noud (marathonman), Cor (lekker shekkie en dan is alles goed), Paul (lekker kort), Jeroen (de motorheld), Marlies (ECRH met een vrouwelijke touch), O.G. (ECRH met een mannelijke touch), Jaap en Ruud, Bart (voor alle goede data), Geurt, Tony, Theo en Frans. Het was altijd bijzonder plezierig om met jullie samen te werken.
En natuurlijk Hajnal (het is beter als het mooi weer is) en Gert Jan (Zonder streepje, en niet leuk, wel waar). Wim (voor de gezelligheid). Een rits studenten die een groot deel van het experimentele programma voor hun rekening hebben genomen: Martijn (laalalaa, geld), Frank (hup zo de gracht in), Marleen (Tsja) en Erik (Indo) Min. Yvonne Kramer voor de moeilijke formules.
De SEG groep: Peter Busch (niet te hard), Geert Verhaag , Wim Kooijman voor de ongelooflijk mooie software. Zowat iedereen van de Werkplaats en de tekenkamer. André en Erik voor de Unix ondersteuning. En Kees voor het betere PC-werk. Piet van Kuyk en Wim Tukker voor de prachtige figuren.
Daarnaast iedereen van het ondersteunend personeel. Het is geweldig dat je op Rijnhuizen zoveel en zo snel hulp krijgt op wat voor gebied dan ook.
En last but not least, de hardloopploeg om de overtollige energie eraf te lopen. (waarvan op het laatst niet veel meer over was). Sorry, helaas, ik heb Peter B. niet weten te kloppen.

Curriculum Vitae

Ik ben geboren op 8 april 1970 te Roermond. Het examen Atheneum B heb ik gedaan in mei 1988, aan de scholengemeenschap St. Ursula te Horn. Meteen daarna ben ik Technische Natuurkunde gaan studeren aan de Technische Universiteit in Eindhoven. Mijn afstudeerwerk bestond uit een experimenteel onderzoek aan de ionisatie graad van een Ar/H_2-cascadeboog plasma. De belangrijkste diagnostiek bij dit onderzoek was een Thomsonverstrooiingsdiagnostiek. Ik ben afgestudeerd op 31 augustus 1994. Op 1 oktober 1994 ben ik begonnen aan mijn promotie onderzoek bij het FOM-instituut voor plasmafysica "Rijnhuizen". De resultaten van dit onderzoek staan beschreven in dit proefschrift.

STELLINGEN

BEHORENDE BIJ HET PROEFSCHRIFT

FILAMENTATION OF TOKAMAK PLASMAS

Marc Beurskens

Eindhoven, 24 maart, 1999

1. Voor een goede analyse van de foutenbijdragen in een Thomsonverstrooiingsmeting met een hoog oplossend vermogen is het van groot belang om naast de juiste lokalisatie van ruisbronnen in het instrument, het effect van het instrumentprofiel op de ruimtelijke uitsmering van de meting in ogenschouw te nemen.
   Dit proefschrift.

2. In een tokamak zijn met behulp van een Thomsonverstrooiingsdiagnostiek met een hoog ruimtelijk oplossend vermogen, structuren op de elektronentemperatuur gemeten met een afmeting van 5 % van de kleine straal van het plasma. Een tweedimensionaal beeld van deze structuren kan verkregen worden door een serie metingen te verrichten met een repetitiefrequentie die een orde van grootte hoger is dan de rotatiefrequentie van het plasma.
   Dit proefschrift.

3. In een "reversed field pinch" zijn de toroidale en poloidale componenten van de elektrische stroomdichtheid van de zelfde orde van grootte. Een combinatie van radiële en tangentiële observatie van Thomsonverstrooiing is een mogelijkheid om deze componenten afzonderlijk te meten.

4. Het standaardbeeld van warmtetransport in tokamakplasma's die enkel worden verhit door dissipatie van de elektrische stroom is incompleet en dient te worden aangevuld met de invloed van inhomogeniteit van de warmtegeleiding.
   *M.R. de Baar, et al., Phys. Rev. Lett., **82**, 1999, 89-93.*

5. Een manier om fusiebrandstof aan een brandend thermonucleair plasma toe te voegen, is de injectie van ijsbolletjes van waterstofisotopen. De dichtheidstoename van het plasma als functie van de kleine straal wordt meestal bepaald aan de hand van het verloop van de volumeintegraal van de H_α lijnemissie. Deze methode is foutief.
   J. de Kloe, et al., ingestuurd naar Phys. Rev. Lett.

6. Bij de berekening van de hoeveelheid negatieve lading op een stofdeeltje in een radiofrequente ontlading bij lage druk dient rekening te worden gehouden met het feit dat de snelheidsverdeling van de elektronen sterk afwijkt van de snelheidsverdeling volgens Maxwell.
   *M. Capitelli, et al., Plasma Chem. and Plasma Proc., **8**, 1988, 399.*

7. Vrije-elektronenlasers zullen de concurrentie met door titaan saffier lasers gepompte parametrische generatoren nog aankunnen zolang deze laatsten geen verstembare pulsduur hebben.

8. Een veel gebruikte techniek bij de behandeling van aspecifieke rug-klachten is rugtractie. De grootte van tractiekracht bij de behandeling, met een maximum van 50 % van het lichaamsgewicht, heeft geen effect op het herstel van deze klachten.
   A.J.H.M. Beurskens, et al., Lancet, 1995, 346: 1596-1600.

9. De belangrijkste obstakels op de weg naar een fusiereactor zijn niet van wetenschappelijke en technologische, maar van politieke aard.

10. De schoonheid van de menselijke ziel hangt niet af van haar geluk.

Stellingen behorende bij het proefschrift
Filamentation of tokamak plasmas
Marc Beurskens, Eindhoven,
24 maart, 1999